2010

UV-LITHOGRAPHIC PATTERNING OF MICRO-FEATURES ON A CONICAL MOLD INSERT

Justin P. Huber
University of Kentucky, jphube2@gmail.com

ABSTRACT OF THESIS

UV-LITHOGRAPHIC PATTERNING OF MICRO-FEATURES ON A CONICAL MOLD INSERT

In past studies, several techniques have been employed to create microscopic features on relatively simple surfaces. Of these, lithography-based techniques have proven effective at manufacturing large fields of deterministic microasperities and microcavities on planar and cylindrical substrates. The present study focuses on adapting UV-lithography to a more complex substrate. Machined from stainless steel, a conical mold insert introduces an interesting geometry designed for the injection molding of radial lip seal elastomer. The distinct shape of this mold insert poises unique challenges to a conventional lithography procedure. Spray application is investigated as a feasible means to deposit layers of photoresist on the surface. An appropriate masking element is designed and created to facilitate transfer of a particular pattern via UV exposure. A clamping technique is implemented to align and secure the photomask. These techniques are incorporated into a three-day process, and results are obtained through optical microscopy and light interferometry. By applying Design of Experiments (DOE) and Analysis of Variance (ANOVA), significant process variables are indentified. Based on these findings, refinements to the process are enabled and future considerations are made evident.

KEY WORDS: UV-lithography, conical mold insert, spray application, radial lip seal, and micro-textures.

Justin Huber

November 17, 2010

(Date)

RULES FOR THE USE OF THESES

Unpublished theses submitted for the Master's degree and deposited in the University of Kentucky Library are as a rule open for inspection, but are to be used only with due regard to the rights of the authors. Bibliographical references may be noted, but quotations or summaries of parts may be published only with the permission of the author, and with the usual scholarly acknowledgments.

Extensive copying or publication of the thesis in whole or in part also requires the consent of the Dean of the Graduate School of the University of Kentucky.

A library that borrows this thesis for use by its patrons is expected to secure the signature of each user.

Name	Date

THESIS

Justin P. Huber

The Graduate School
University of Kentucky
2010

UV-LITHOGRAPHIC PATTERNING OF MICRO-FEATURES ON A CONICAL MOLD INSERT

THESIS

A thesis presented in partial fulfillment of the
requirements for the degree of Master of Science in Mechanical Engineering in the
College of Engineering
at the University of Kentucky

By

Justin P. Huber

Lexington, Kentucky

Director: Dr. L. Scott Stephens, Professor of Mechanical Engineering

Lexington, Kentucky

2010

ACKNOWLEDGEMENTS

The completion of the following thesis would not have been possible without the unique contributions of several people. I am grateful to my advising professor, Dr. L. Scott Stephens, for his guidance, patience, and advice. As representatives of Infiinite Graphics Incorporated, Ron Videen, Gene Brunn, and Mike Wilcox played instrumental roles in photomask development. I thank Rob Hardman and Harris Miller for their continuous technical support concerning Microchem® Microspray™ products. Various metal fabrications and modifications were possible because of the skill and expertise shared by Herb Mefferd and Larry Crockett. I also thank several fellow researchers for their support: Daniel Impellizerri developed key devices for UV-exposure, Chris Morgan provided MATLAB® support, and Katherine Warren continually offered advice on various aspects of the lithography process. Lastly, I would like to pay special thanks to my Thesis Committee members: Dr. L. Scott Stephens, Dr. Keith Rouch, and Dr. Christine Trinkle.

The support from my family and friends has been invaluable. I thank my parents and my brothers for providing advice and motivation throughout my academic pursuits. I am equally indebted to my friends for their tolerance and encouragement.

TABLE OF CONTENTS

LIST OF TABLES

LIST OF FIGURES

CHAPTER 1 — INTRODUCTION TO UV-LITHOGRAPHY

1.1 Introduction

Dealing on a scale of centimeters & inches, part fabrication becomes a trivial application of tools commonplace in a machine shop. Measuring tapes and squares help translate drawing information onto a work piece. A few revolutions in a lathe create a desired diameter, or a short pass with a milling tool produces a straight channel. As the scale shrinks to the realm of millimeters & mils, the demands of accuracy & precision overwhelm the keen eye of a well-practiced machinist. Digital sensors and readouts become necessities. The radius of a drill bit now limits part specifications. Smaller still, components demand sub-micron precision, and customary machining methods become obsolete.

Furthermore, creating such parts a thousand times over proves time-intensive and cost-ineffective. Extend this logic beyond the manufacture of individual parts to the manufacture of a repeating pattern. Features must be created on a single substrate, side-by-side, and with consistent tolerances. Room for error rapidly constricts. Moreover, suppose these patterns must be applied to non-planar surfaces. For example, consider a steel work piece exhibiting curved edges, sharp chamfers, and other unusual geometries. Now, machining techniques must cross the brink from conventional to experimental.

The present work investigates such an experimental technique to create a pattern of micron-sized features on the surface of an unusually shaped substrate. Specifically, ultraviolet lithography serves as the technique, and the micro-texture consists of an array of triangular asperities (i.e. posts) with identical dimensions on the order of 10μm to 100μm as shown in Figure 1-1. The substrate of interest is a stainless steel mold. Depicted in Figure 1-2, the mold exhibits sharp corners and chamfered edges. The specific surface to receive the aforementioned micro-texture is more complex than the planar surfaces investigated in previous studies. Resembling a frustum, the surface can be appropriately described as conical. By achieving the desired micro-texture on this conical mold, injection molding can be utilized to manufacture nitrile rubber elastomers with a corresponding micro-texture as indicated in Figure 1-3.

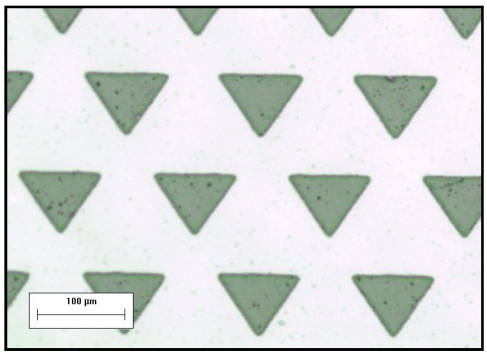

Figure 1-1. Pattern comprising an array of triangles.

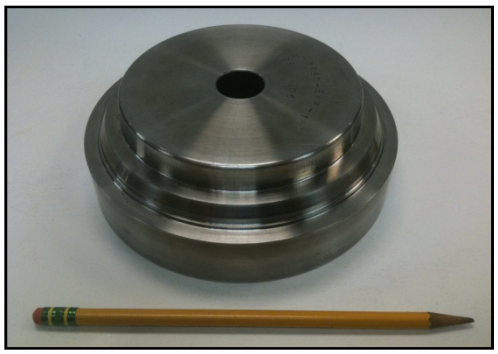

Figure 1-2. Conical mold insert to receive micro-texture.

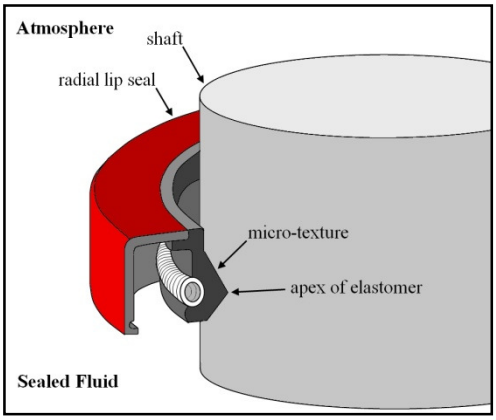

Figure 1-3. Micro-textures on the mold insert may be transferred to a radial lip seal elastomer via injection molding.

Ultraviolet lithography shares many similarities with another popular microfabrication process – LIGA. Developed at the Institute for Microstructure Technology in Karlsruhe, Germany, this micro-structure fabrication technique comprises three main steps: X-ray lithography, electroforming, and molding [1]. As the name indicates, UV-lithography incorporates a more accessible ultraviolet source in place of the relatively expensive X-ray synchrotron used in LIGA. Besides this difference, the two processes dawn essentially the same methodology. Namely, a special chemical is applied to a substrate; when exposed to a specific spectrum of light (X-ray or UV), the intermolecular structure of the chemical changes. In an ensuing development step, a solvent is used to exploit this chemical change. The product can then serve as a template for electroplating. The final result is a substrate incorporating micron-sized surface features with aspect ratios on the order of 100:1 [1,2]. A basic overview of the fabrication process is shown in Figure 1-4 [1].

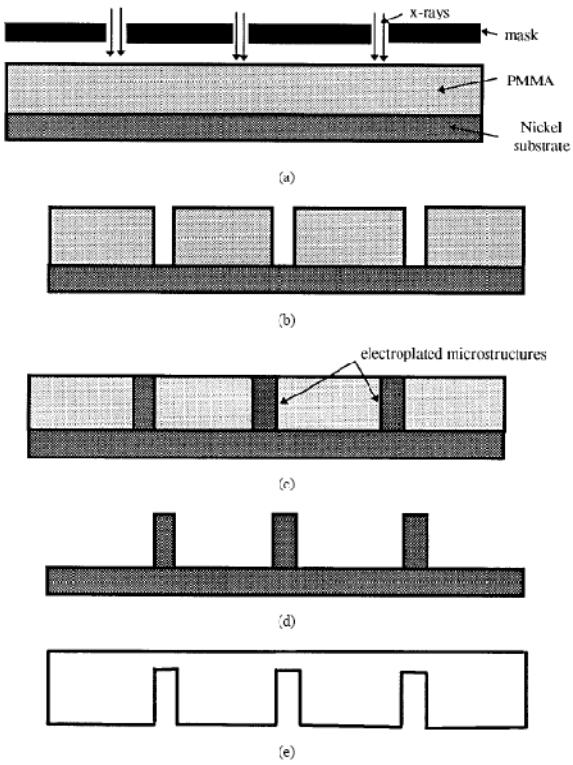

Figure 1-4[1]. Overview of LIGA process. The chemical structure of polymethyl methacrylate (PMMA) changes upon exposure to X-rays (a) facilitating its removal during a development step (b). In UV-lithography, a similar chemical may be used, which will experience chemical changes during UV-exposure. Electroforming (c) followed by additional processing creates a mold (d), which can be used to create a desired part (e).

1.2 Interesting Aspects of Current Work

Flat silicon wafers have been popular recipients of UV-lithography in past studies [3]. Even cylindrical surfaces have been successful candidates, but a conical substrate presents a new frontier for this process. With this challenge come new possibilities. Creating a micro-texture on this conical mold insert pushes the geometric boundaries of UV-lithography beyond simple surfaces toward more complex surfaces with broader applications. For instance, a neurosurgeon's micro-textured probe may penetrate more easily through a patient's skin [4], or arrays of micro-features may accelerate heat dissipation from an engine component [5]. Expanding the applicability to more diverse substrates has the potential to boost marketability and churn further research & development of this technology.

To compliment this market growth potential, UV-lithography is already recognized for its economic advantage in the field of micro-feature fabrication. Replacement of an X-ray synchrotron device with a more accessible ultraviolet source shrinks costs by improving availability [6,7]; moreover, the relatively short exposure times translate to fewer processing hours [7]. The nature of the lithographic process makes it well suited to a mass production application [8]. Although micro-machining provides a means for creating individual parts, adapting such techniques for micro-texturing involves extended processing times and costly tool maintenance [9]. Laser surface texturing is also disfavored economically [10,11]. No doubt, investors attracted to the improving applicability of UV-lithographic patterning will find the inherent economic benefits equally appealing.

Scientific motivations also accompany the financial motivations. Applying micro-patterns to a conical mold insert presents a challenge, and such challenges elicit innovation. The present work applies concepts of lithography that have existed for decades, but these concepts are implemented through slightly modified techniques. An aerosol spray distributes a photosensitive chemical on a surface instead of a conventional spin-coating method. An exposure mask dawns a peculiar shape to match a peculiar substrate. A customized screw clamp aligns and secures this mask to a conical surface. These methods may prove remarkable; they may prove to be trivial. Regardless, they represent an innovative mindset striving to advance the scientific understanding of UV-lithography.

Moreover, successful lithographic patterning of a conical mold insert may advance research opportunities in other fields. At the University of Kentucky, the Bearing and Seals Laboratory has a vested interest in micro-textured surfaces and how such textures affect tribological behavior. Paige studied micro-texturing of a rubber thrust ring as shown in Figure 1-5, which was manufactured via a similarly textured mold insert [12]. An investigation by Warren studied smooth radial lip seals operating against a micro-patterned steel shaft [13]. A foreseeable progression of this research is a study of a micro-textured radial lip seal operating against a smooth steel shaft. A conical mold insert would be crucial to advancing these scientific efforts.

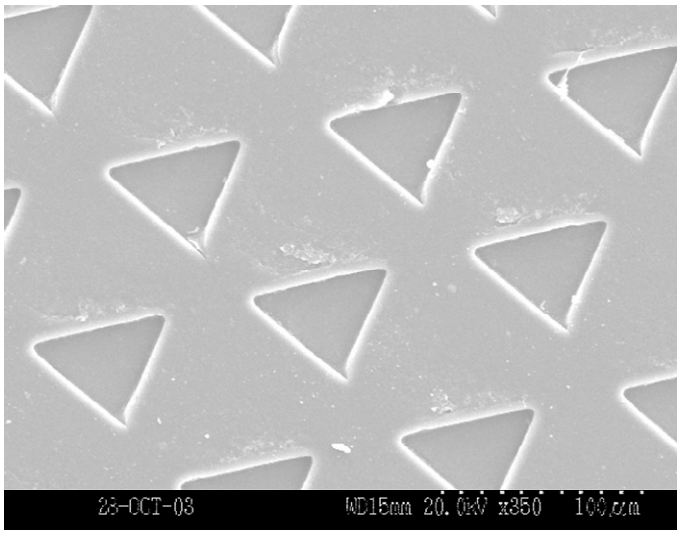

Figure 1-5[12]**.** Array of triangle microasperities molded into a nitrile rubber disk.

Along with a progression of current research, the present work may have immediate commercial applications. The complexity of the mold insert owes to its intended purpose. That is, the work piece has been designed for injection molding of radial lip seals used in a specific application for the transportation industry. Supposing that micro-patterns can be correlated to the performance improvement of radial lip seals, a demand for these seals may ensue. Refinements to the present research work could then facilitate an integration into the commercial sector.

1.3 Challenges to Present Research

A repeatable, reliable UV-lithographic process must preface such commercialization, but several obstacles arise when micro-texturing a conical mold insert. For example, photoresist application presents certain challenges. When dealing with silicon wafers and other planar substrates, spin-coating tends to be the preferred coating method [7,14,15]. However, a conical mold insert introduces declining surfaces, which inevitably lead to pronounced edge buildup. The inability to spin-coat eliminates an obvious means of achieving a uniform coat thickness; other means of photoresist application must be refined to minimize thickness variations. Otherwise, the quality of ensuing lithography steps suffers. In particular, thickness variations hinder intimate contact between the substrate and an exposure mask, which proves critically important to lithography resolution [6]. Additional obstacles to UV-lithography are encountered

due to the size and mass of the conical mold insert. Relative to a silicon wafer, the mold insert requires greater handling care to accommodate its weight. The high mass also introduces a considerable heat reservoir, which must be accounted for during any baking steps. Development and electroplating parameters must also be optimized for the atypical surface area and geometry. Additionally, the non-planarity of the mold insert prohibits polishing the textured surface on a conventional lapping machine.

1.4 Key Approaches and Methods

In light of the aforementioned issues, innovative methods are required to apply the UV-lithographic process to the conical mold insert. In place of spin-coating, the present work has adopted a relatively new XP Microspray™ offered by Microchem Corporation; this product adapts the chemistry of liquid photoresist into an aerosol form. To create an appropriate exposure mask, the 3-dimensional conical surface is translated to a 2-dimensional planar image, which can then be printed using the precision services of Infinite Graphics, Incorporated. Successful mating and alignment of this mask is achieved using a clamp plate, which exploits existing threads machined into the mold insert. The Bearing & Seals Laboratory provides a rotating jig developed by Daniel Impellizzeri to facilitate uniform UV exposure of the work piece. In addition, various other devices have been fabricated to properly handle the conical mold insert both during the lithographic process and during the eventual analysis.

To refine UV-lithographic texturing techniques, the prior methods are evaluated and optimized using successive application of experimental design (DOE) and analysis of variance (ANOVA). Post-exposure development of photoresist provides a key visual indication to the success or failure of the overall process. Poor quality at this stage will only be expounded during electroplating. In contrast, precise pattern geometries and straight sidewalls predict a favorable outcome. The present work attempts to quantify this visual indicator; specifically, the degree of photoresist coverage obtained experimentally is compared to an ideal case. Variations in coverage can then be associated with variations in process parameters. This methodical approach reveals that UV-exposure dosage is a significant factor to consider when texturing the conical mold insert. Moreover, the magnitude of this dosage may deviate considerably from the manufacturer's recommendations [16].

CHAPTER 2 – PREVIOUS WORK

2.1 Background of LIGA and UV-Photolithography

Developed from German roots, the LIGA process gained popularity as a micro-fabrication method due to the high aspect ratios it facilitated [10]. Originating at the Nuclear Research Center of Karlsruhe, a team of scientists including Erwin Becker and Wolfgang Ehrfeld spearheaded efforts to produce extremely small separation nozzles for uranium enrichment [17]. This work combined steps of synchrotron X-ray lithography, galvanoforming, and plastic molding into a single process capable of forming parts with micron-scale dimensions, excellent resolution, and immense structural heights. Prior to this research, few records existed of features successfully incorporating all of these characteristics. The findings from this investigation would eventually extend beyond the intended nuclear application and into fields of microelectronics, optics, and medicine.

Upon development of the LIGA process, manufacturing terminology soon welcomed a new acronym – HARM (High Aspect Ratio Microstructures). With heights on the range of hundreds of microns and widths in the scope of tens of microns, these structures could be readily manufactured with the resources and expertise available in Germany. However, a broadening interest in HARMS eventually culminated with research efforts by the MicroSystems Engineering Team (μSET) in Baton Rouge, Louisiana.

Vikas Galhotra and colleagues at Louisiana State University aimed to mass produce large sheets with expansive areas covered by HARM [18]. To progress toward this goal, an important step included manufacturing a mold insert. Applying the same polymethyl methacrylate (PMMA) adopted by their German counterparts, the LSU team applied X-ray exposure to this photoresist using a wire mesh mask to create a comparable pattern on a nickel plated silicon wafer. The ensuing electrodeposition utilized a modified Watt's bath. With relatively high current density and deposition rates, this modified bath produced nickel structures with desirable heights and a high hardness well-suited for the rigors of molding. However, this investigation revealed issues of photoresist delamination thought to be caused by thermal cycling induced during exposure or by swelling of PMMA during submersion in the plating bath.

The continuing efforts at LSU to create large fields of HARM eventually led to a slightly modified LIGA procedure. The introduction of a clamping mechanism to secure a PMMA template to the nickel substrate replaced the chemical bonding necessary in prior studies. This mechanical clamp effectively eliminated the issue of delamination. Applying this technique, mold inserts were successfully covered by nickel HARM with structural heights ranging from 500µm to 1000µm as shown in Figure 2-1 [19]. A series of injection molding tests supported the viability of using such inserts to produce fields of cavities in a thermoplastic polymer as shown in Figure 2-2 [19]. However, drawbacks became evident. Namely, features incorporated into the PMMA template had to be self-supporting, which incurred considerable limitations to electroplated patterns. For instance, this approach could produce fields of tall nickel posts on a mold insert, but it could not produce fields of cavities within a layer of nickel.

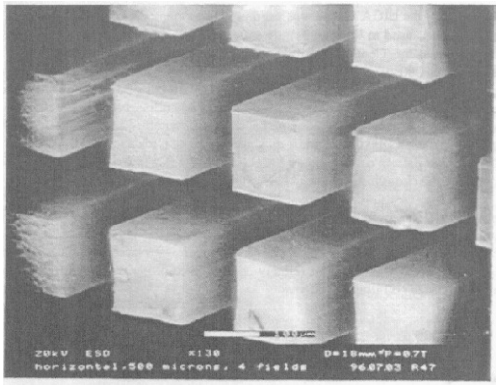

Figure 2-1[19]. A field of nickel posts 500µm in height created on a nickel sheet.

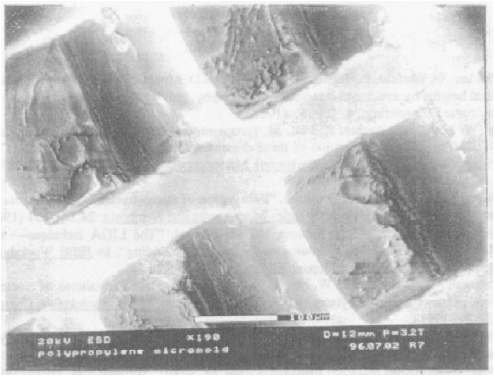

Figure 2-2[19]. Cavities created in thermoplastic polymer via injection molding.

Having demonstrated the ability of LIGA to create micro-feature arrays on a planar macroscopic area, the natural progression was to adapt such methods to nonplanar surfaces. The research group in Baton Rouge would provide further insight. The mechanical clamping technique previously mentioned yielded an interesting approach; namely, by eliminating the need for a chemical bond, the process of developing a PMMA template was decoupled from the process of electodeposition. With this notion in mind, Marques and colleagues could develop a planar free-standing polymer template via masking and X-ray exposure, and this template could then be wrapped around a nonplanar, cylindrical shaft to be electroplated [1]. Resulting from this approach, a nickel cylinder measuring 1.6cm in diameter was successfully covered with a field of microposts measuring 150µm in diameter and 500µm in height as seen in Figure 2-3 [1].

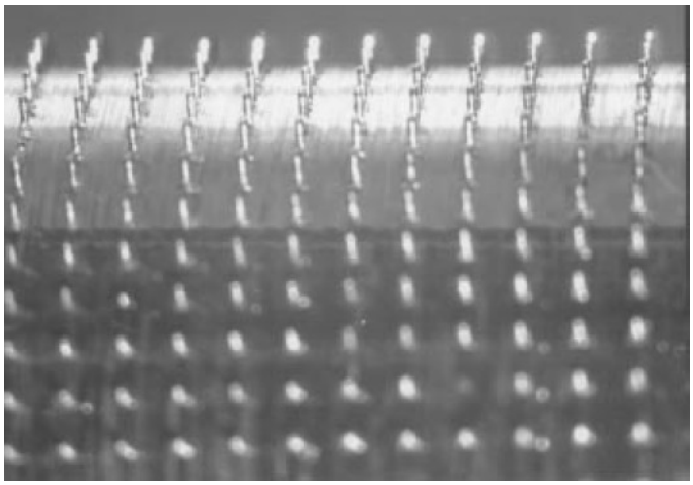

Figure 2-3[1]. A nickel cylinder covered by 500μm tall microposts.

Incorporation of LIGA technology into useful applications remains a prerequisite to its introduction to commercial markets. In his dissertation prepared at LSU, Marques demonstrated one such application that utilized microposts in a novel surface designed to enhance heat exchange at the leading edge of gas turbine blades [5]. With a curvature comparable to that of a turbine blade, a nickel cylinder was covered with electroformed nickel microposts, which further supported a sheet of nickel. The space surrounding the microposts and between the surfaces hence provided channels for cooling airflow. Thus, a technology intended for nuclear applications was adapted for alternative means, which further supported the growing applicability of LIGA as imagined during its German infancy.

However, a certain characteristic of PMMA prolonged the reception of LIGA into mainstream manufacturing. Though PMMA offered superior resolution and aspect ratios of 100:1, its relative insensitivity to radiation necessitated long exposure times. For instance, approximately 6 hours were required to adequately expose a layer of photoresist measuring 500μm in thickness. This requirement was a sizable drawback when considering mass production scales. Fortunately, Jian Zhang presented a possible alternative in his 2002 thesis defense [20]. Introduced by IBM, an epoxy resin known as SU-8 exhibited sensitivities to X-ray exposure nearly 200 times that of PMMA. Despite a diminished resolution, this SU-8 compound proved a viable option for many applications, and the shorter processing time bode well economically.

Even during the early development at Karlsruhe, researchers acknowledged that the limited availability of radiation sources would be detrimental to transitioning LIGA onto a commercial scale [17]. Becker and colleagues relied on an X-ray synchrotron stored at the Bonn University in western Germany. Other candidate sites included the BESSY facility located in Berlin and the DORIS facility located in northern Germany. Within the United States, researchers at Baton Rouge relied on resources at the nearby CAMD facility [5]. However, with only 13 synchrotron stations in North America, availability proved a staunch opponent to the commercialization of LIGA [21].

A low-cost alternative to synchrotron arrived in the form of ultraviolet photolithography wherein a more accessible UV light source replaced the X-ray synchrotron. The Bearings and Seals Laboratory (BSL) at the University of Kentucky successfully incorporated this approach. Utilizing the SU-8 resin, Kortikar applied ultraviolet exposure to pattern stainless steel thrust bearings with a variety of microfeatures ranging from square asperities (posts) to triangular cavities [10]. In later work, Venkatesan incorporated similar geometries into thrust rings by utilizing SU-8 as well as a proprietary photoresist offered by Rohm and Hauss® [22]. Yang and colleagues in Baton Rouge applied UV-exposure to create microfeatures of different heights on a mold insert [7]. More recently, researchers at the University of Kiel in Germany adapted an ultraviolet light source to transfer patterns onto a rotating cylindrical substrate [23].

2.2 Microfabrication on Complex Surfaces

As microfabrication methods have progressed, substrate geometries have gradually strayed from the traditional silicon wafer. Free-standing PMMA templates have facilitated a modified LIGA process to texture a nickel cylinder [5]. The inception of ultraviolet exposure and new photoresist has permitted lithographic patterning of Ni/Ti-coated glass rods [23]. Still other machining techniques attempt to texture ball bearings and the interiors of half-cylinders [24,28]. As new concepts for fabrication develop, the scope of substrates continues to grow.

Cylinders have become a popular candidate for variations of the lithographic process. As previously mentioned, researchers at LSU successfully implemented a modified LIGA method to manufacture microstructures on a nickel shaft [1]. A free-standing planar PMMA template was heated via convection oven to approximately 130°C; the resulting flexibility of the polymer was then exploited to wrap a nickel shaft measuring 2cm in diameter. Following electroplating, the

nickel substrate acquired the desired micro-texture. Marques and colleagues also successfully applied this technique to a nickel cylinder measuring 1.6cm in diameter and 5.5cm in length as well as to a stainless steel tube with 19.1mm diameter (3/4”), 12.1cm length (4-3/4”) , and an arbitrary wall thickness of 1.6mm (1/16”) [5]. At the University of Kentucky, members of the BSL applied UV-lithography to create fields of micro-cavities on a cylinder; the resulting stainless steel shaft then served to elucidate the behavior of radial lip seals [13,25]. Researchers at the University of Kiel adapted the UV-lithographic technique to transfer patterns to narrow glass rods [23]. In this study, the rotational movement of a glass sample was carefully synchronized with the lateral movement of a planar mask; as shown in Figure 2-4, a successful test specimen consisted of circular patterns covering a glass tube measuring 1.5mm in diameter [23].

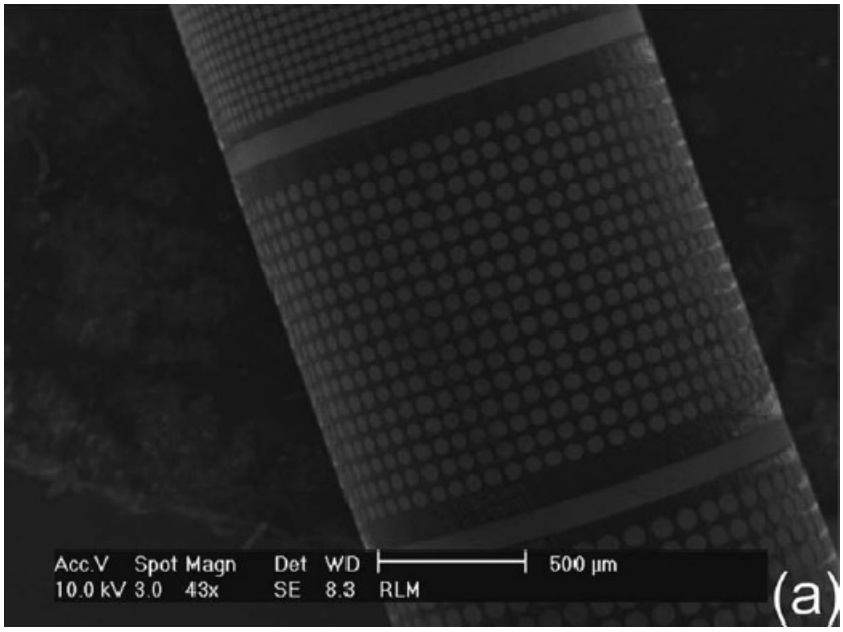

Figure 2-4[23]. Ni/Ti-plated glass tube measuring 1.5mm in diameter and covered with a pattern of circles.

The cylindrical substrate has also become a prime focus of laser ablation methods. Geiger and colleagues at the University of Erlangen-Nuremberg in Germany successfully applied imaging optics to concentrate an excimer laser onto a ceramic work surface [26]. In combination with a masking technique, arrays of microstructures were formed onto the exterior surface of ceramic disks made from aluminum oxide and silicon carbide. At the Technion-Israel Institute for Technology, Etsion has continually refined techniques to modify substrates with laser surface texture (LST). In a study published in 2008, Etsion and Sher applied LST to the exterior surface

of piston rings with outer diameters measuring 93.7mm and face-widths measuring 2.5mm; these rings were then incorporated into a functional Fort Transit diesel engine [27]. Chauvy and colleagues at the Swiss Federal Institute of Technology focused efforts on three-dimensional titanium surfaces. Combining laser treatment with electrochemical micromachining, researchers created a pattern of circular cavities onto a hollow titanium cylinder measuring 1cm in outer diameter and 2cm in height as shown in Figures 2-5 and 2-6 [24].

Figure 2-5[24]**.** Hollow titanium cylinder covered with micro-cavities.

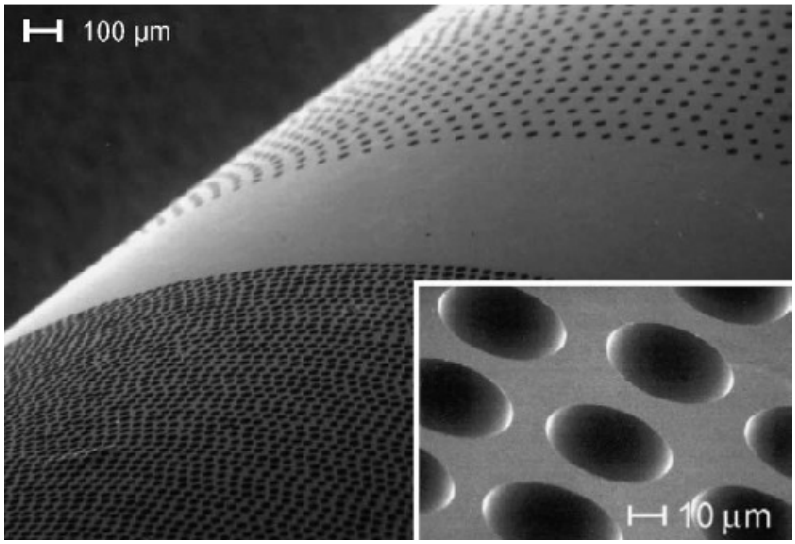

Figure 2-6[24]**.** Magnified imagery showing the pattern of micro-features applied to the titanium cylinder via laser and electrochemical micromachining.

Along with the advent of lasers and lithography, still other methods have been demonstrated to transfer patterns to complex, nonplanar surfaces. Pettersson and fellow researchers at the Uppsala University in Sweden developed a novel embossing technique. By depositing a diamond film with Hot Filament Chemical Vapor Deposition (HFCVD), a tool with diamond micro-structures could be formed. As depicted in Figure 2-7, this tool could then be pressed against the surface of a steel ball bearing to create the desired texture [28]. At the Herriot-Watt University in Edinburgh, researchers utilized concepts of electrostatics and lithography to form micro-textures. By administering a high voltage potential, a polymer coat applied to a metal surface was manipulated to reflect the texture of an opposing metal electrode. The setup illustrated in Figure 2-8 formed a polymer micro-texture on the interior of an aluminum half cylinder measuring 9.5mm in diameter [29].

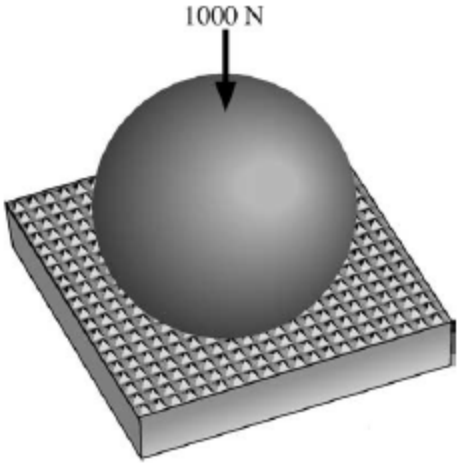

Figure 2-7[28]**.** Illustration of a novel diamond embossing tool used to texture a steel ball bearing.

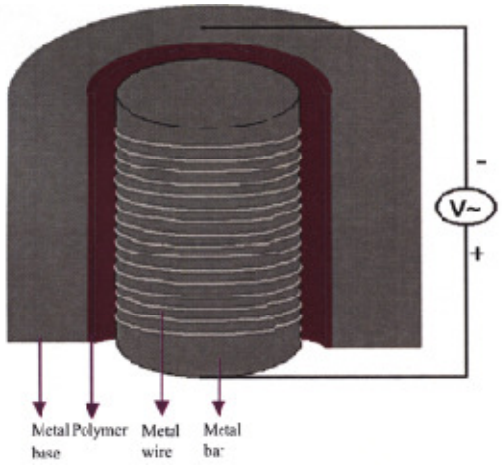

Figure 2-8[29]**.** A center electrode is used to texture the surrounding electrode via electrostatic induced lithography.

2.3 Fields of Micro-Structures Applied to Macroscopic Areas

Advancements in lithography add to the diversity of micro-fabrication methods, and researchers exploit this diversity to continually push the limits of micro-texturing. Requiring a high degree of repeatability, these expansive patterns of microscopic features allow little room for processing error. However, techniques such as laser surface texturing, UV-lithography, and novel diamond-tool embossing have enabled breakthroughs. These methods represent the brink of research, which continues to reduce measurement scales, improve quality, and expand the complexity of micro-patterns.

Progress in micro-texturing has relied profoundly on improvements in MicroElectroMechanical Systems (MEMS). Though repeatability may be arguably less critical, these systems demand high precision and quality. Efforts by Miyajima and Mehregany focused on applying photolithography to create a comb-drive actuator, which drives microscopic linear motion using electrostatic forces [6]. This device shown in Figure 2-9 exhibited fingerlike projections with dimensions ranging from 2μm to 20μm. At Louisiana State University, Dai and Wang fabricated similar actuation devices shown in Figure 2-10, which facilitated linear movements on the scale of 10μm to 40μm [30]. The capabilities of this technology were further demonstrated by Wang and colleagues to manufacture the relatively complex power relay shown in Figure 2-11 using innovative multi-step, multi-layer UV-photolithography [31].

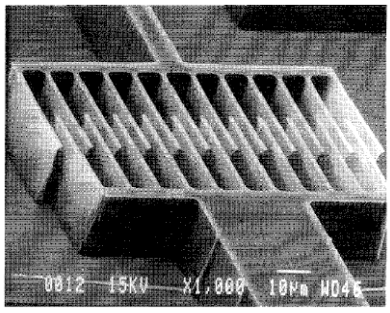

Figure 2-9[6]. Comb-drive actuator with 3μm wide fingers spaced 2μm apart.

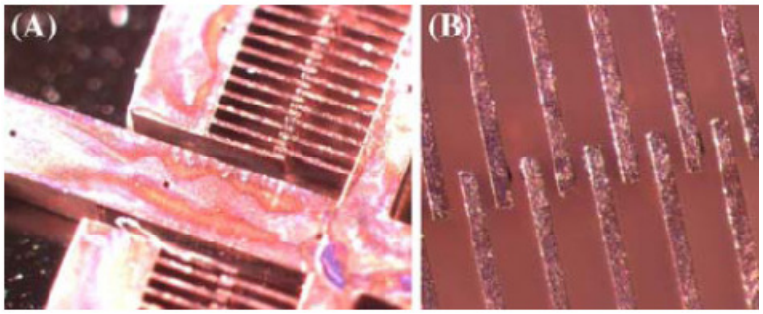

Figure 2-10[30]. The MEMS shown (A) provides actuation in the range of 10-40μm. A close up (B) illustrates the required precision of the finger-like projections.

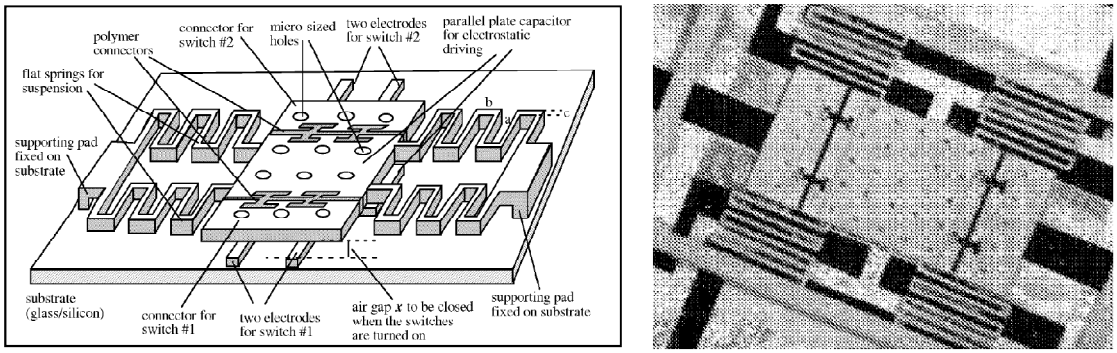

Figure 2-11[31]. The schematic (left) shows the design of a novel micro-relay that relies on electrostatic forces in the middle capacitor to close two adjacent switches. The photograph (right) depicts a birds-eye view of the prototyped relay.

As shown in Figure 2-12, various other micro-structures have been successfully created using a deep X-ray lithography method (DXRL); through collaborative efforts, this research has offered insight into improving the economics of MEMS fabrication [2].

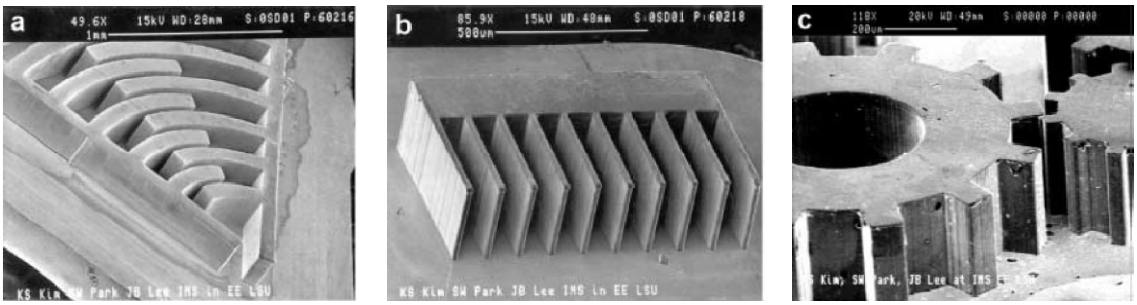

Figure 2-12[2]. With structural heights of 300μm, several patterns (a-c) for MEMS were successfully incorporated into nickel mold inserts. The patterns were then transferred to silicone rubber via casting.

To adequately gauge progress in MEMS and micro-texturing technologies, several characterization techniques have been developed. Of these, the concept of aspect ratio has proven useful in measuring process capability. This term refers to the ratio between a feature's longer dimension and its shorter dimension as the following Figure 2-13 illustrates. The popularity of LIGA relied considerably on this concept as numerous studies demonstrated the process's unique ability to attain aspect ratios of 100:1 and higher [1,2]. This basic definition has evolved into slight variations, though the general concept remains the same [6]. In addition to aspect ratio, surface characterization has welcomed a variety of other terminologies. Patterns of grooves and thin-walled features are often referred to in terms of line-width and line-spacing. Expansive textures necessitate the use of parameters such as average surface roughness, skewness, kurtosis, and area fraction ratio. Collectively, this language of surface characterization enables researchers with the analysis tools needed to further the science of micro-fabrication.

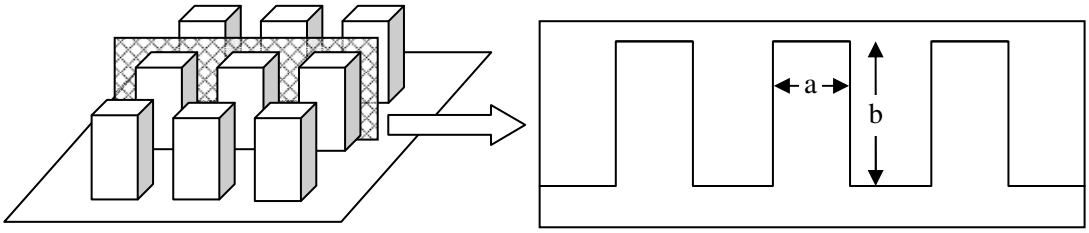

Figure 2-13. Aspect ratio refers to the ratio between a longer dimension (b) and a shorter dimension (a).

In the science of micro-texturing, a logical endeavor has focused on miniaturizing conventional machining. For instance, successful efforts to produce small, high-precision tools have advanced research in micro-turning, micro-milling, and micro-grinding. In a collaborative study, Morgan and colleagues demonstrated the capability of micro electro discharge machining (μEDM) to fabricate a cylindrical milling tool made from polycrystalline diamond (PCD) measuring 50μm in diameter. The scanning electron microscope (SEM) images in Figure 2-14 show a few surface features created within a brittle glass substrate using this PCD tool [32]. At the University of Singapore, similar research efforts utilized a custom-made PCD tool to machine microscopic features into a stainless steel plate [9]. The series of micro-holes shown in Figure 2-15 provide a glimpse of the micro-texturing capabilities of this process. However, time and cost inevitably hamper such a process. Creating each micro-hole required approximately 2 minutes; a

field with thousands of these features would prove time-intensive. Additionally, issues of tool wear, inaccurate tool re-positioning, and unreliable substrate clamping reduce machining quality. Though such micro-machining techniques provide a valuable tool for quick prototypes, the current methods would be impractical to micro-texturing applications.

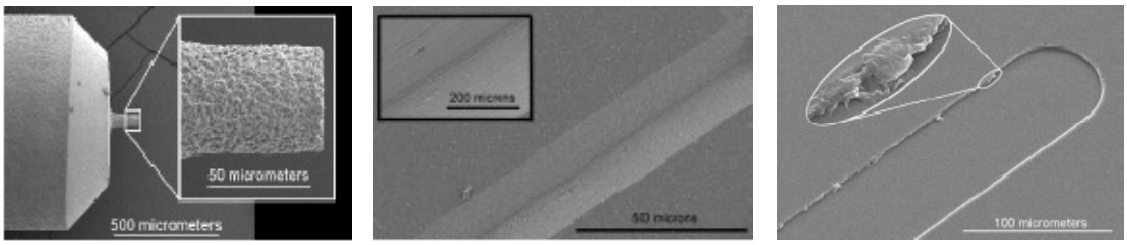

Figure 2-14[32]. SEM images of a PCD micro-milling tool (left), a 50µm deep groove created in soda-lime glass (center), and a 5µm deep pocket machined in ultra low expansion glass (right).

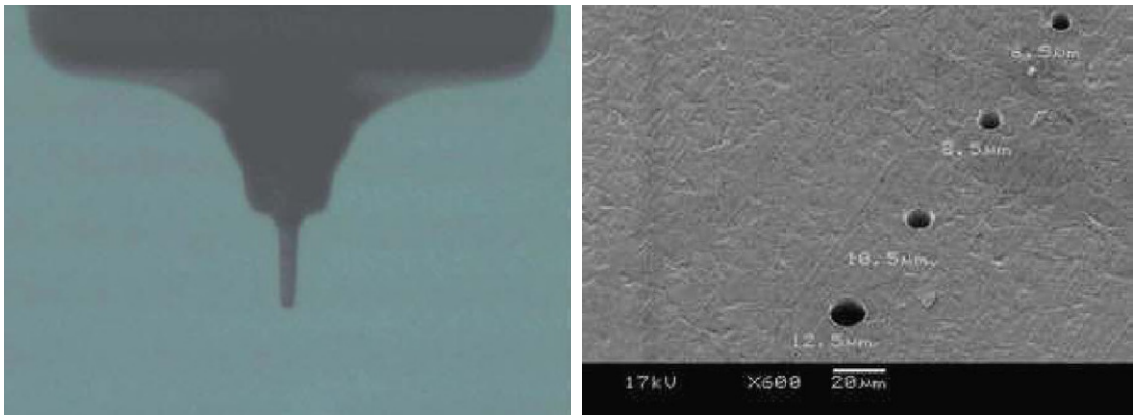

Figure 2-15[9]. A PCD micro-tool (left) is utilized to machine an array of holes (right) of varying diameter in a stainless steel plate.

A more practical approach has focused on the established LIGA method. During early development of this process, Becker and colleagues created masks with intricate patterns of gold and copper on a beryllium membrane [17]. Pattern transfer via X-ray exposure yielded templates for nickel electrodeposition on steel or copper substrates. The finished micro-texture consisted of hexagonal prisms with widths of 80µm, heights of 330µm, and 4µm wide gaps between features. This texture is depicted in Figure 2-16 along with a honeycomb pattern produced with comparable dimensions.

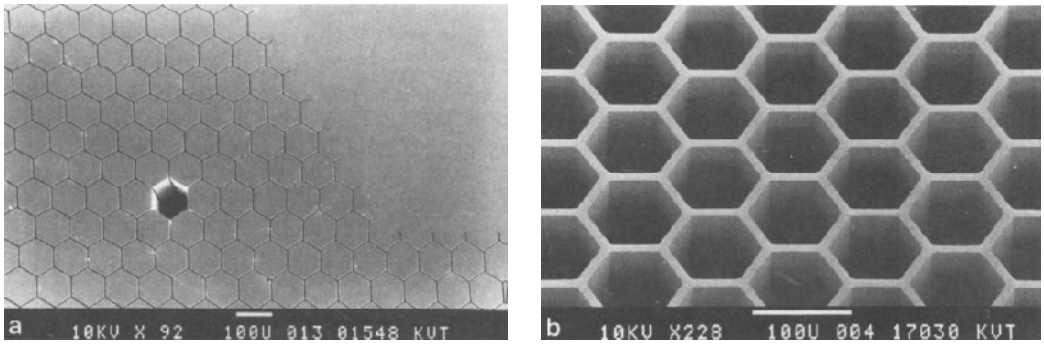

Figure 2-16[17]. A field of hexagonal nickel prisms (a) and honeycomb structures (b) created with few defects. A single prism was intentionally removed for analysis.

At Louisiana State University, researchers successfully masked a PMMA layer using a fine wire-mesh; upon X-ray exposure, the resulting layer provided an adequate template for electroplating square protrusions with side lengths of 500μm, heights of 490μm, and spacing of 14μm between each feature [18]. However, adhesion loss between the PMMA and the nickel-coated silicon substrate became a recognized issue. Further efforts relied on mechanically clamping the photoresist to a flat nickel substrate. As shown in Figure 2-17, the resulting micro-texture comprised a field of rectangular posts measuring 500μm in height [1]. This clamping methodology was further exploited to manufacture fields of cylindrical posts measuring 150μm in diameter with post-to-post spacing of 1mm.

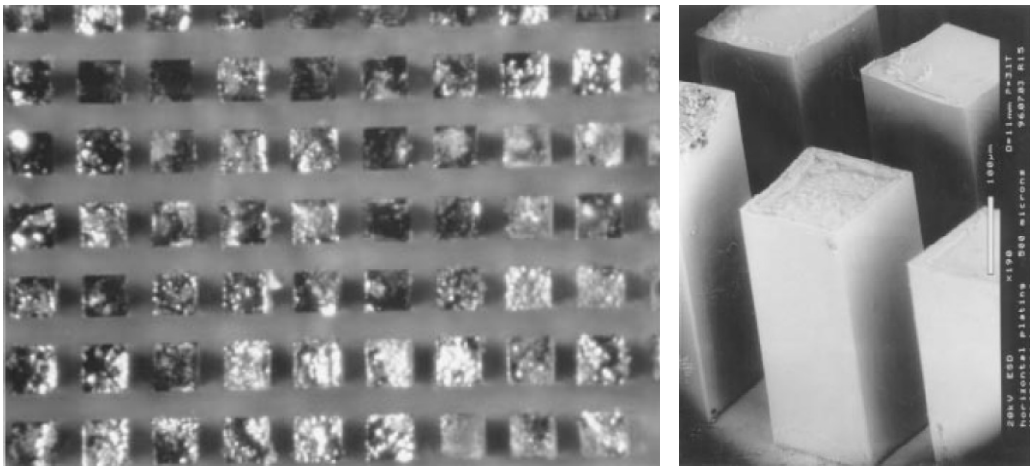

Figure 2-17[1]. Fields of rectangular nickel posts (left) manufactured on a nickel sheet. A close up (right) lends perspective to the 500μm height of these features.

As micro-texturing via LIGA has progressed, its commercial viability has also steadily improved. Marques demonstrated the potential of this technology to augment the heat exchange properties of various surfaces [5]. Depicted in Figure 2-18, he manufactured a nickel plate that incorporated a staggered array of nickel pin-fins measuring 500µm in diameter and 500µm in height. Additionally, Marques modified this micro-texturing process to create a cylindrical surface mimicking the leading edge of a turbine blade. The surface shown in Figure 2-19 comprised an in-line array of 200µm OD, 500µm tall posts sandwiched between an inner layer of stainless steel and an outer nickel shroud.

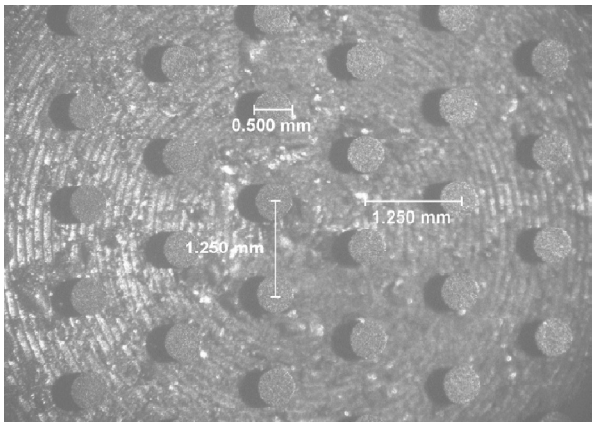

Figure 2-18[5]. Array of pin fins measuring 500µm tall created on the surface of a heat exchanger.

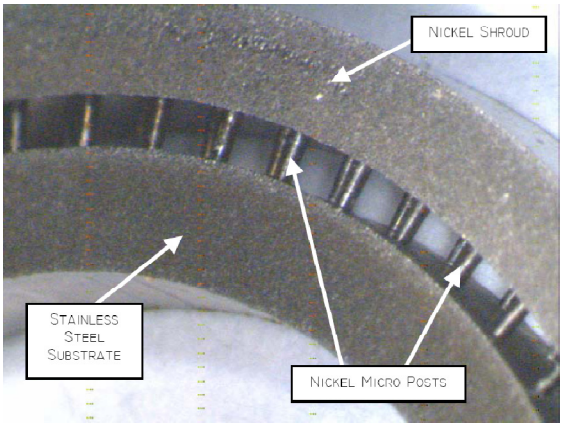

Figure 2-19[5]. A novel heat exchanger surface incorporates micro posts within a coolant flow channel.

In a later study, Turner focused on developing micro-textures to enhance the heat exchange properties of a seal [33]. An interesting aspect of this work involved the introduction of a draft angle to facilitate the injection molding process. Using a cutting edge exposure device, the resist-coated substrate could be slightly tilted with respect to the X-ray source and fully rotated about its axis. This tilt feature permitted interesting polymer micro-features with non-vertical sidewalls, which enabled the desired draft angle. Turner manufactured the tapered nickel mold insert depicted in Figure 2-20, which includes a honeycomb-shaped field of hexagonal cavities that forms a circular annulus. As shown in Figure 2-21, this mold was successfully applied to produce seal parts covered by the desired array of hexagonal posts with face-to-face widths of 320µm, heights of 960µm, and a 3° draft angle.

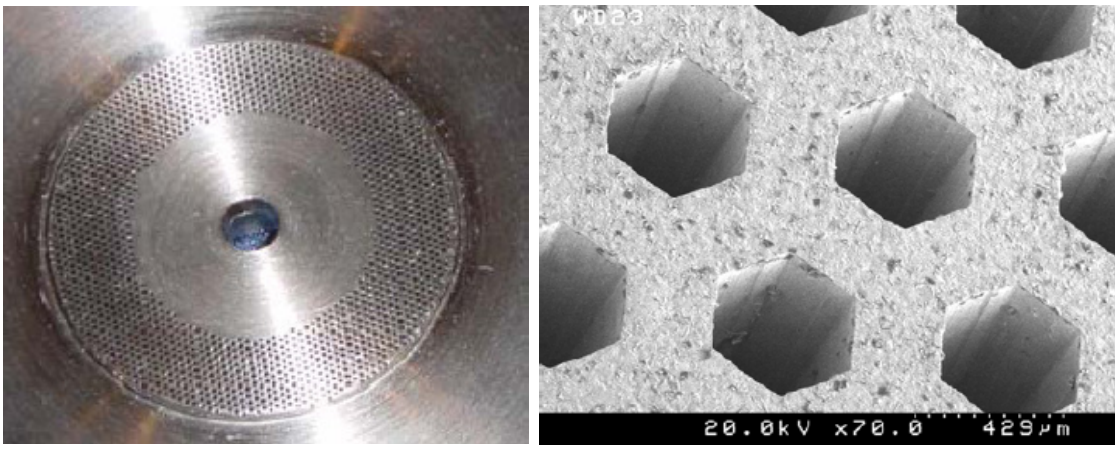

Figure 2-20[33]. Nickel mold insert (left) incorporates features with a slight taper (right) to facilitate part ejection during the molding process.

Figure 2-21[33]. A micro-texture created on a molded seal part consists of hexagonal posts measuring 960µm tall with a 3° draft angle.

At the University of Kentucky, several research efforts concentrated on micro-texturing bearing surfaces for the purpose of improving tribological behavior. The Bearings and Seals Laboratory utilized LIGA to manufacture a hexagonal array of hexagon micro-asperities on a 28.5mm OD stainless steel thrust ring [34]. Depicted in Figure 2-22, the surface features measured approximately 550µm in average diameter with heights of 14µm; the overall micro-texture exhibited an asperity density of roughly 2.5 asperities per square millimeter.

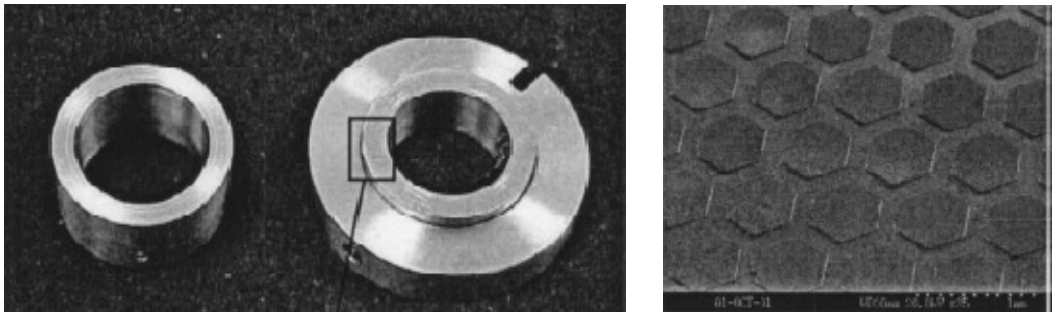

Figure 2-22[34]. A stainless steel thrust ring (left) serves as the substrate for a hexagonal array of electrodeposited nickel micro-asperities (right).

Dependence on a synchrotron source is an acknowledged pitfall of LIGA; however, by incorporating an alternative light source, this pitfall can be surpassed. Kortikar applied UV-photolithography techniques to create various patterns on a 3" diameter thrust disk [10]. This work demonstrated the process potential to create patterns with a specific area fraction ratio (δ^2); this surface characteristic compares the area of micro-features to the overall substrate area. In Figure 2-23, the bearing surface is covered by a field of 480μm wide square micro-asperities with a deliberate area fraction ratio, $\delta^2 = 0.40$, and heights measuring 15μm. Additionally, Kortikar successfully manufactured fields of triangular asperities and fields of square cavities with area fraction ratios ranging from 0.05 to 0.70.

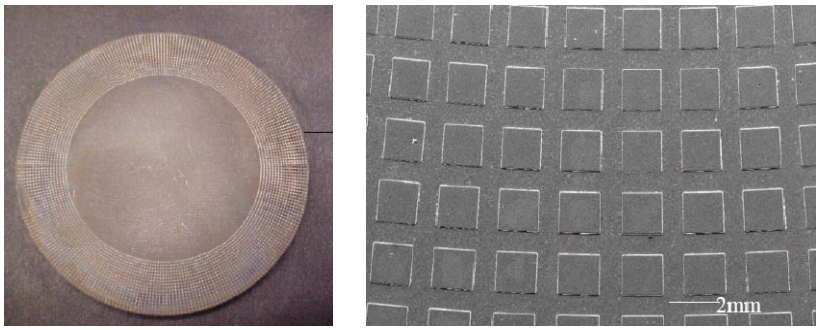

Figure 2-23[10]. Thrust disk (left) micro-textured with an array of 15μm tall square micro-asperities (right).

In addition to the diverse shapes of surface features, Warren demonstrated that these shapes could be produced in various orientations [13]. Minor alterations during the masking step enabled micro-texturing a stainless steel shaft with triangular cavities oriented in specific directions. This process control became an important aspect to studying micro-pumping—an interesting tribological phenomenon that accompanies ongoing developments in micro-texturing.

Besides lithography-based techniques, alternative methods of micro-texturing have incorporated lasers. In a joint effort, Swiss and Russian researchers utilized a pulsating copper-vapor laser to produce micro-grooves on a sapphire plate. Emitting light at 510nm wavelength, the laser beam required an average power of a few milliwatts to produce two specific patterns. A rough pattern consisted of parallel grooves measuring approximately 11µm wide and 4µm deep, and a fine pattern comprised of similar grooves 3µm wide and 2µm deep. Both patterns exhibited a periodicity of about 20µm. Captured using atomic force microscopy, the image shown in Figure 2-24 depicts the rough pattern created in the sapphire plate substrate [35]. Of note, this laser technique avoided the usual crater formations that typically accompany laser ablation processes. Moreover, grooves maintained a relatively consistent width. However, the large variations in groove depth presented a considerable drawback.

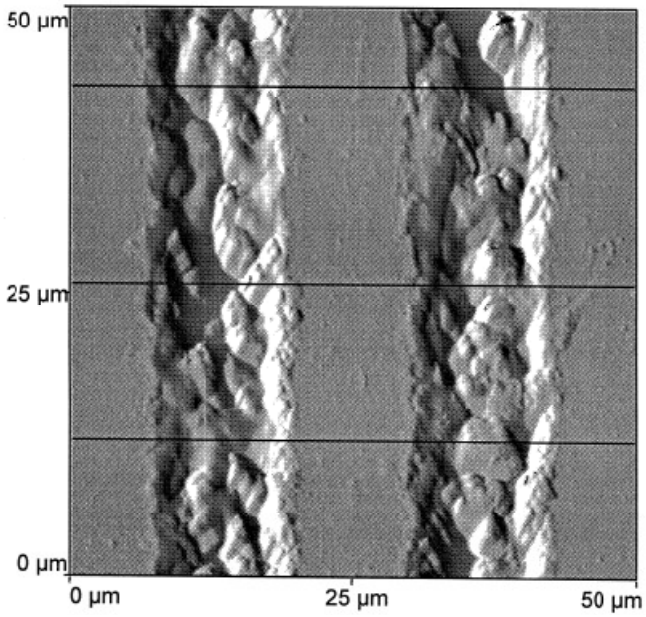

Figure 2-24[35]. Pattern of grooves etched into sapphire plate by pulsating copper-vapor laser.

In Bern, Switzerland, Dumitru and colleagues at the Institute of Applied physics successfully implemented a Nd:YAG laser to produce micro-craters within stainless steel. With a diameter of approximately 10µm, the depth of the structures could be varied between 5µm and 8µm by controlling the number of laser pulses administered. An undesirable consequence of this method was the bulge formation around the rim of each micro-crater. Depicted in Figure 2-25, this formation could be minimized to a certain degree; furthermore, a motorized translational stage could then facilitate micro-texturing of the stainless steel substrate [11].

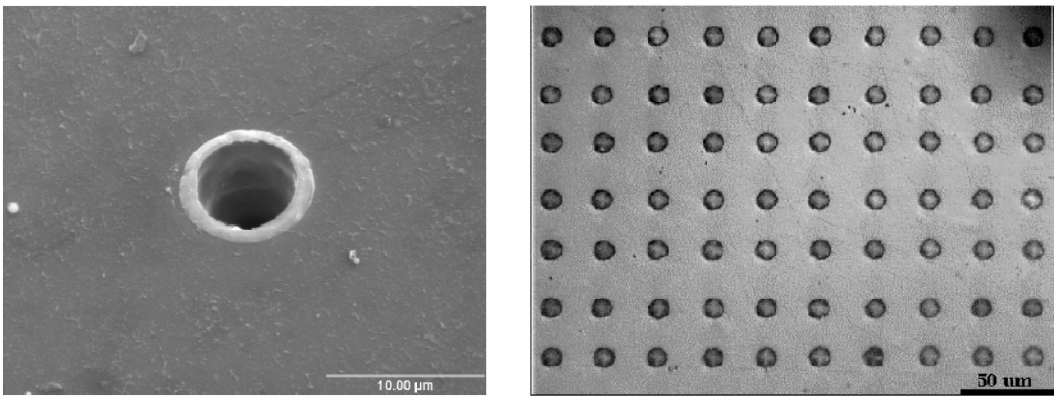

Figure 2-25[11]. A micro-feature (left) formed using an Nd:YAG laser is replicated to form a micro-texture in stainless steel (right).

German researchers at the University of Erlangen successfully incorporated a masking step into laser micro-texturing. Using a XeCl excimer laser emitting wavelengths in the UV range (308nm), a beam with a cross-sectional area of 2mm by 2mm was introduced onto a ceramic work surface. By applying a mask, relatively large areas of the substrate could be patterned with hundreds of micro-structures at the same time. This method was successfully implemented to produce fields of circles, triangles, or rectangles in substrates of alumina oxide and silicon carbide; feature depths could be varied from 25µm up to 150µm [26]. The arguably low heat transfer involved in this process made it well-suited for materials sensitive to thermal shock—an issue that generates undesirable surface micro-cracks and material embrittlement [36].

Extensive development of Laser Surface Texturing (LST) has been practiced at the Technion Israel Institute of Technology. Etsion has contributed significantly to developments in the texturing of mechanical seals. By applying LST, modified seal rings have been produced that include fields of micro-dimples with 100µm diameter, 10µm depth, and an area density of 20% [37]. In addition, Etsion has implemented this method to piston rings to study the tribological effects. Figure 2-26 illustrates this micro-texturing applied to the outer cylindrical face of a piston ring segment measuring 93.7mm in diameter. Using a 3D optical profilometer scan, the actual pattern achieved on the piston ring is also depicted [27].

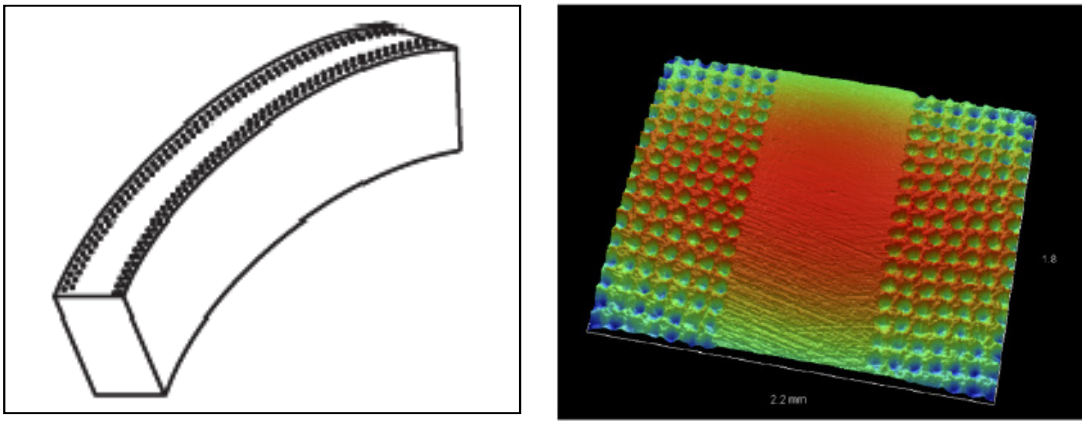

Figure 2-26[27]. Schematic of LST applied to a piston ring segment (left) and a scan of the actual texture achieved (right).

Micro-texturing continues to progress down several scientific avenues. However, these avenues are revealing unique obstacles. Efforts to miniaturize conventional machining methods are hampered by issues of tool wear, extensive processing times, and poor quality control. Studies utilizing the LIGA technique must confront the scarcity of synchrotron sources; moreover, if PMMA is used, long exposure times must be accommodated. Research involving lasers must resolve issues caused by thermal shock: micro-crack development, material embrittlement, and crater formation. Techniques such as electrostatic induced lithography and embossing show potential for micro-texturing but are underdeveloped for commercial applications. In contrast, UV-lithography offers several attractive features. Initial tooling times are relatively short and offset by the mass-production capabilities. Readily available ultraviolet lamps can be used in place of synchrotrons. Repeatability and dimensional consistency are inherent process qualities. These factors provide motivation to incorporate UV-lithography into micro-texturing research, and this paper attempts to exploit these features to pattern a complex, conical mold insert.

CHAPTER 3 – MOTIVATIONS BEHIND WORK

3.1 Improving Performance of Bearings and Seals

Successful incorporation of micro-textures into bearing & seal technologies stands to impart significant benefits. Friction continues to be a plaguing force; in automobile engines, studies suggest that 40% of the developed energy is lost due to engine friction [38]. These frictional effects may be reduced by integrating microscopic textures into components [34,35,37,38,40]. Textures may also considerably lessen lubricant usage [13,39]. Less lubrication means optimum bearing performance can be sustained at lowered costs. In addition, bearing and seal life may be substantially extended due to the presence of micro-textures [37]. This longer life may be coupled with functional improvement; a textured bearing may handle more extreme loading conditions compared to its non-textured counterpart [43]. Unlocking this potential continues to drive micro-texture research and development.

Theoretical evidence is growing. At the University of Kentucky, researchers developed a mathematical model to compliment the actual performance of a textured thrust ring [34]. Exploiting the concept of "unit cell", the model considered a single hexagonal asperity and its surrounding cavity to yield an expression for friction coefficient. A lower coefficient indicates lower frictional forces between interacting surfaces. Less friction may translate to less wear, longer part life, and minimal energy loss. As Figure 3-1 illustrates, certain characteristics of the asperity could be optimized to reduce the frictional coefficient; compared to the theoretical results for a plain thrust surface, data suggested as much as a 60% reduction.

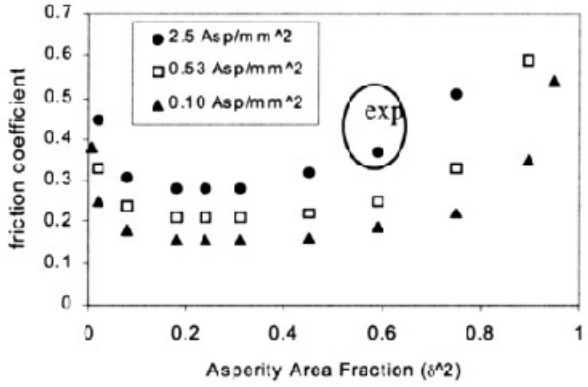

Figure 3-1[34]. Model predicts reduced friction in a thrust bearing by optimizing surface texture characteristics.

As a progression of this work, the Bearing and Seals Laboratory analyzed a numerical model of a radial lip seal. Simulating a micro-textured steel shaft rotating against a smooth elastomer, this model revealed the potential benefits of deterministic microasperities. The plots shown in Figure 3-2 provide insight; optimizing asperity height and geometry may reduce the frictional coefficient by 35% as compared to surfaces with naturally occurring microasperities [39]. Deterministic asperities may also improve load capacity. By optimizing asperity height, an engineered surface may support up to 45% higher loads. Moreover, theoretical data suggested certain asperity geometries may impart a unique "reverse pumping" phenomenon; rather than lubricant leaking from the seal interface, it can be conserved due to dynamic behavior caused by the engineered surface texture [39].

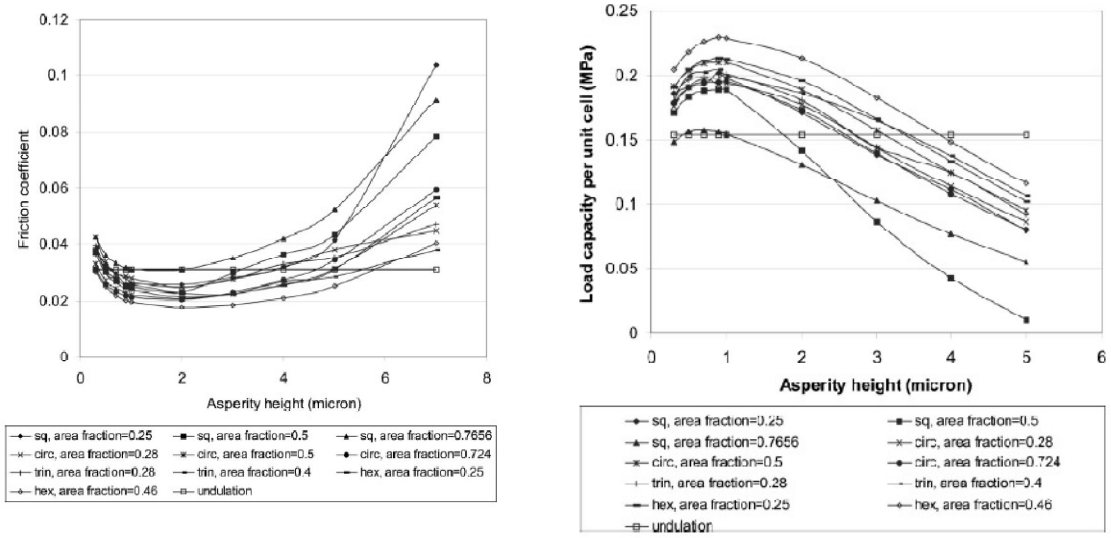

Figure 3-2[39]. Compared to the natural undulations that form on radial lip seal surfaces, deterministic microasperities may reduce friction (left) and simultaneously improve load capacity (right).

Etsion and colleagues provided additional theoretical support behind micro-textures in a bearing application. As previously mentioned, friction within internal combustion engines greatly diminishes energy efficiency. The Israeli research group addressed this issue by modeling laser surface textured (LST) piston rings reciprocating against cylinder liners. The texture consisted of hemispherical micro-pores. As shown in Figure 3-3, the model suggested that micro-pore geometry may be optimized to reduce friction forces by 30% or more [38].

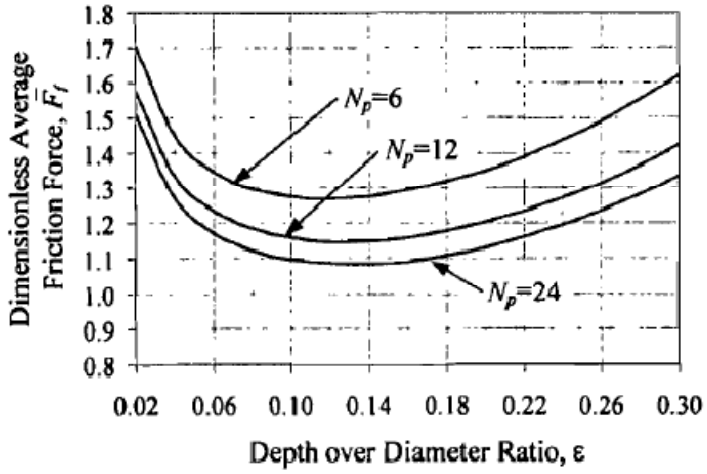

Figure 3-3[38]. By optimizing micro-pore geometry, ε, and number of pores, N_p, friction may be considerably reduced using textured piston rings as compared to their non-textured counterpart (ε = 0).

Recalling previous modeling of the radial lip seal, Etsion's research group developed a comparable simulation with one major exception: the micro-texture resided on the elastomeric surface as opposed to the metal shaft [40]. This investigation yielded favorable results. By optimizing the geometry of micro-dimples within the elastomer, frictional forces were shown to decrease while load capacity increased. These findings provide significant motivation to realize micro-textures in elastomers—an effort that may rely on an appropriate mold insert.

Theory continues to uncover potential, but a necessary element to micro-texture development has been experimentation. Using a thrust washer rotary tribometer, Stephens provided convincing evidence that engineered surfaces enhance bearing performance. The test setup illustrated in Figure 3-4 introduced a rotating bronze ring to a stationary, micro-textured specimen [34]. Specifically, this specimen consisted of a hexagonal array of deterministic nickel microasperities manufactured on a stainless steel substrate via LIGA methods. Operating within a non-pressurized oil bath, this setup revealed interesting results. Displayed in Figure 3-5, the microasperity height could be optimized to reduce friction coefficent by 14-22% as compared to a conventional plain bearing.

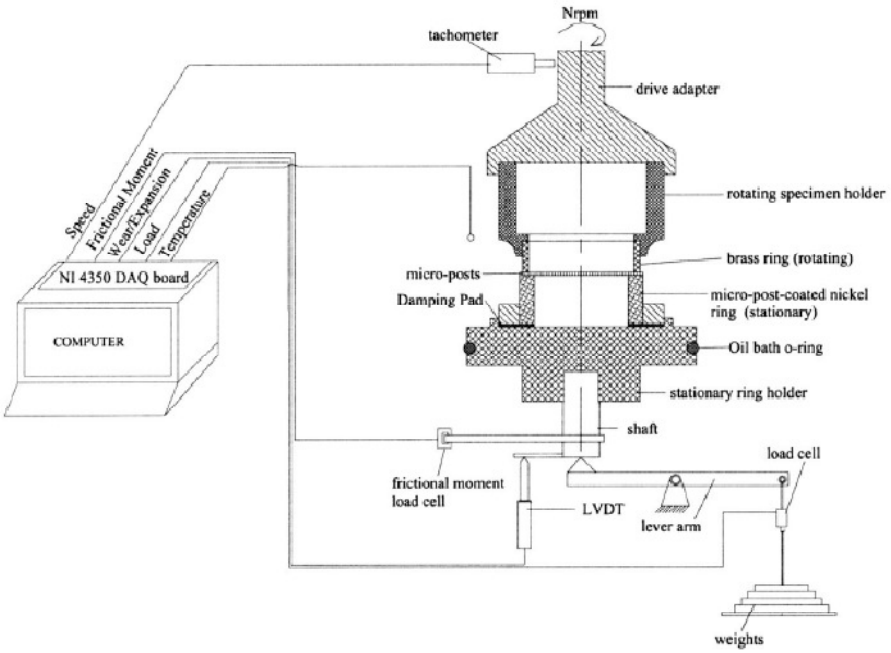

Figure 3-4[34]. Experimental setup to study interaction between a rotating brass ring and a stationary, micro-textured thrust ring.

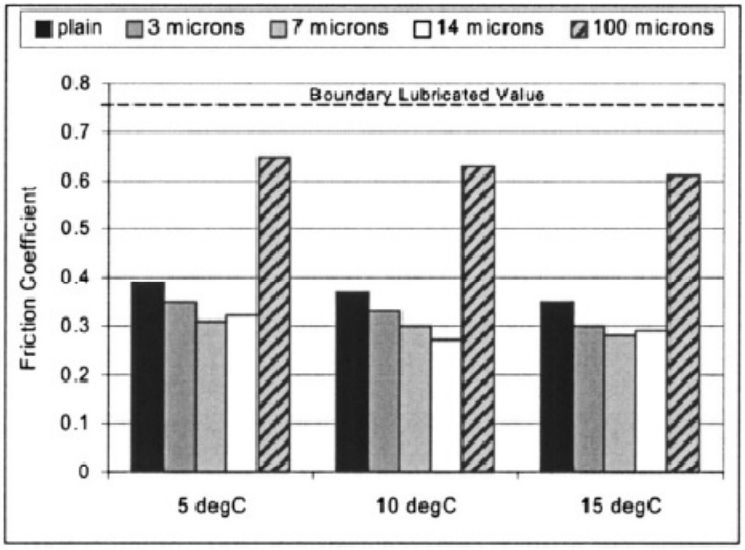

Figure 3-5[34]. For various lubricant temperatures, experimental findings support reductions in frictional effects due to optimized deterministic microasperities.

Using a modified tribometer setup, a study also assessed the performance of radial lip seals with micro-textured shafts. Warren investigated fields of triangular micro-cavities applied to a stainless steel shaft. Adopting the test setup shown in Figure 3-6, data suggested a significant relationship between cavity orientation and sealing capability [13].

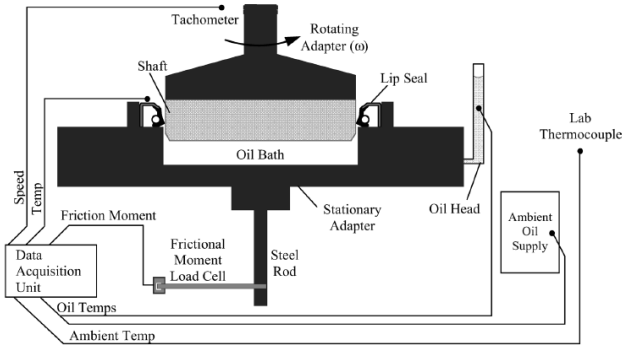

Figure 3-6[13]. Modified tribometer to test radial lip seal.

That is, the apex of the triangular cavities could be directed in such a way to induce "reverse pumping"; consequently, lubricant could be retained despite the opposing behavior caused by a pressurized oil bath. Moreover, when adequately lubricated, this micro-texture reduced frictional effects by as much as 51%. In yet another orientation, these triangular cavities also improved seal performance during starved lubrication; shown in Figure 3-7, "leading" and "lagging" cavities provided friction reductions of 8-13% as compared to a stainless steel shaft. The author suggested this behavior resulted from lubricant retention in the cavities—a popular theory shared within the research community [26,28,41,42].

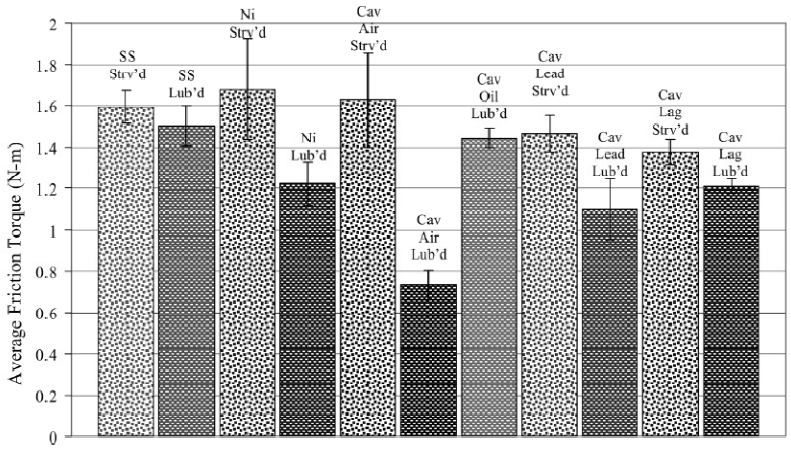

Figure 3-7[13]. When lubricated, cavities directed toward air show exceptional friction reductions. Under starved conditions, "lead/lag" cavities provide noticeable reductions in friction torque.

Laser Surface Textured (LST) substrates have proved interesting specimens for several experimental studies. At the Technion Institute, a research project aimed to incorporate LST into a hydrostatic mechanical seal; depicted in Figure 3-8, the setup consisted of a back-to-back arrangement of seals within a pressure vessel housing a rotating shaft [43]. Partial texturing was applied to the face width of the seal stator rings. Applying low shaft speeds to avoid hydrodynamic effects, the modified seals reduced friction torque over 50% as compared to untextured samples. Moreover, the plot in Figure 3-9 illustrates another marked improvement. The operating pressure as designated by the seal manufacturer was effectively doubled from 12 bars to nearly 24 bars.

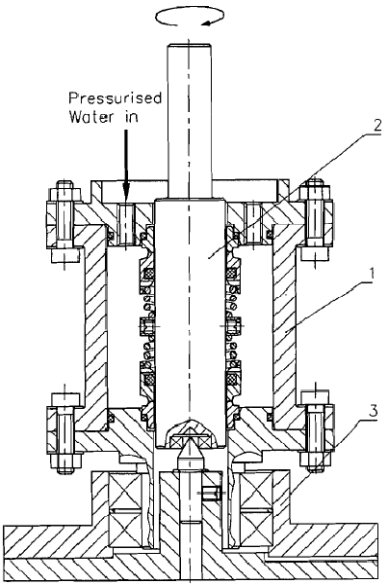

Figure 3-8[43]. A pressure vessel (1) with LST seals houses a rotating shaft (2) supported by a thrust bearing assembly (3).

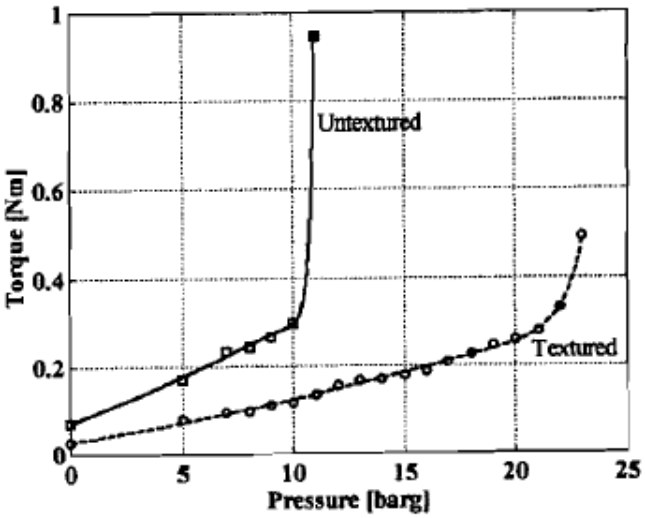

Figure 3-9[43]. Textured hydrostatic seals perform satisfactorily at nearly twice the manufacturer's recommended operating pressure.

Another study incorporated LST into a combustion engine. Using a 2500cm^3 Ford Transit diesel engine, Etsion and Sher applied texturing to specific regions of the piston rings [27]. Operating conditions were carefully controlled to attain desired engines speeds and loading while measurement systems monitored exhaust gas composition and fuel consumption. Spanning a total of 1800 working hours, the experiment yielded an interesting result. Though the exhaust gases remained relatively unchanged, the fuel consumption decreased by 4% with a repeatability of ±0.5%. Compared to the untextured piston rings, the textured specimens minimized energy usage.

Experimentation continues to gain ground. A pin-on-disk setup revealed that laser-etched sapphire plates exhibit reduced friction, decreased wear, and improved test life [35]. Researchers concluded that friction torque within ceramic seals could be reduced by as much as 65% by applying appropriate textures; a petrochemical company discovered that tungsten carbide seals could endure a threefold increase in operating life due to LST [37]. Bearings and seals continue to evolve with the addition of micro-texturing technologies, and UV-lithographic patterning remains a powerful ally to this ongoing development.

3.2 Improving Applicability of Micro-Texturing

Bearings and seals represent only a small portion of the potential market for micro-textures. A simple flat substrate has progressed toward a non-planar geometry; cylindrical and spherical topographies have proved viable candidates for micro-texturing. Such developments have enabled the technology to branch into new disciplines including biochemical research, thermal engineering, and medical instrumentation.

At Louisiana State University, UV-lithography has opened doors to advanced genomic research. Past efforts in this field relied on bulky bench-top equipment. However, lithography techniques have prompted a miniaturization of these instruments. Known as lab-on-a-chip systems, these devices offer broad benefits: reduced manufacturing costs, decreased reagent usage, automation capability, and shortened analysis times. As shown in Figure 3-10, researchers at LSU designed a lab-on-a-chip system to purify nucleic acid [44]. To realize this design, the high precision and quality of UV-lithography was exploited to produce a nickel large area mold insert (LAMI); by applying appropriate heat, this insert was used to emboss a polycarbonate sheet. With a footprint measuring 150mm in diameter, the final device employed an array of 96 capture beds to separate DNA material from other cell debris

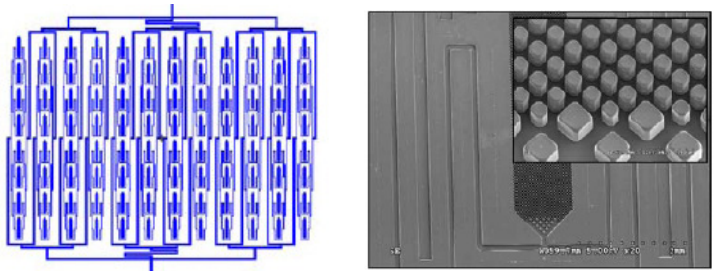

Figure 3-10[44]. Schematic for lab-on-a-chip system (left) and SEM image of a single capture bed (right).

As mentioned in previous chapters, micro-textured surfaces stand to significantly improve heat management. Applying a modified LIGA technique, Marques demonstrated the potential of electroformed fields of nickel micro-posts on a cylindrical substrate; the engineered surface exhibited a 40% increase in heat transfer coefficient [5,45]. This texture could be applied to the surfaces of boiler tubes to enhance performance [46]. Furthermore, these techniques could be applied to create novel heat exchangers; as depicted below in Figure 3-11, coolant flow channels could be incorporated into the surfaces of gas turbine engine blades to increase component life and improve durability [47].

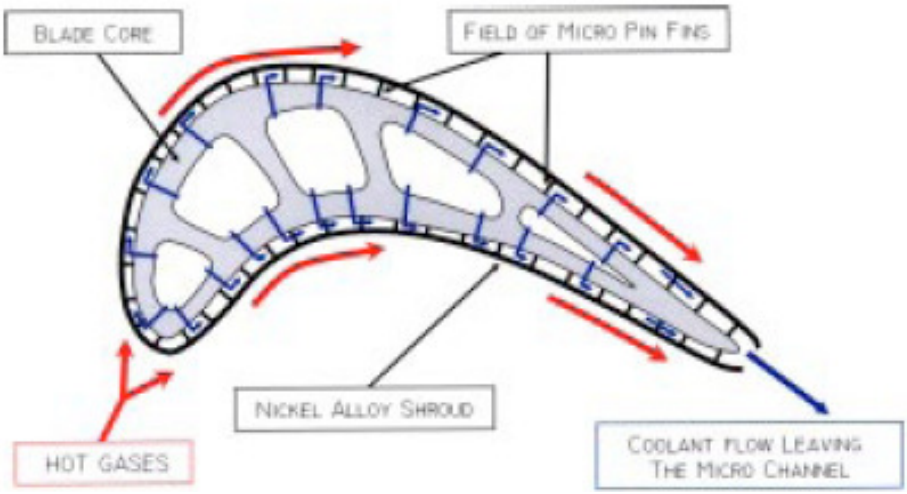

Figure 3-11[47]. Potential application of micro-texturing to enhance heat transfer in a gas turbine engine blade.

The medical field holds considerable potential for micro-textures. At Harvard University, researchers developed a technique to produce structures comparable in form to a coronary stent—a medical device necessary for balloon angioplasty [48,49]. First, patterns developed through photolithography were cast into an elastomeric stamp. This stamp then transferred "ink" to a substrate; the "ink" was hexadecanethiolate and the substrate was a glass rod coated with a silver/titanium seed-layer. The ink pattern protected areas of this seed-layer during an ensuing etch process. Following silver electrodeposition, a concentrated hydrofluoric acid solution removed the glass substrate. In Figure 3-12, the final product is shown in its unexpanded form and in the expanded form that would result after a balloon angioplasty procedure.

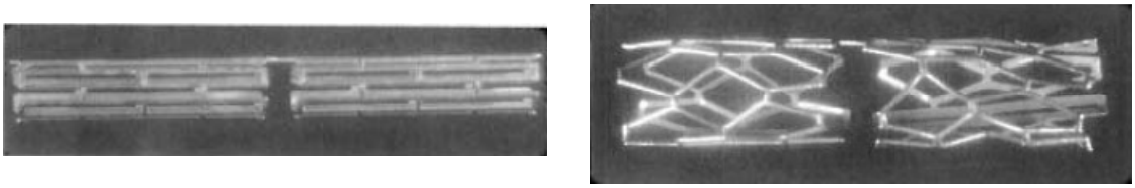

Figure 3-12[48]. The unexpanded structure (left) is created using a Microcontact Printing (μCP) technique. The expanded form (right) would help unblock a blood vessel following a balloon angioplasty.

As the medical community tends toward minimally invasive procedures, micro-texturing may improve the accuracy and safety of next generation neurosurgical probes [4]. Scientists in London have incorporated the technology into surgical needles. Utilizing SU-8 and UV-photolithography, strips of triangular and fin-like teeth were manufactured and adhered to needle frames. Experimental findings indicated reduced insertion forces and increased gripping forces. Moreover, these micro-textures may permit a novel technology. Mimicking a biological mechanism in wasp, a textured neurosurgical probe with reciprocating halves may provide unprecedented directional control to navigate brain tissue along low-risk trajectories.

The incorporation of micro-texturing into medical applications is hindered by a narrow selection of biocompatible materials. However, recent work has addressed this issue. At the Swiss Federal Institute of Technology, researchers developed an innovative process to create patterns on titanium [24]. By selectively irradiating an oxidation layer formed on the metal, a template was created for electrochemical treatment. This study introduced a novel method to engineer the surfaces of titanium implants commonly used in dental and orthopedic applications.

The scope of micro-texture applications continues to expand; however, as form and function become more specific, these textures must be applied with increasing attention to location and orientation. Engineered surfaces on a surgical probe are constrained by the width of a needle. To manufacture the medical stent, a planar pattern must be transferred seamlessly onto a thin glass rod. With each new application and process, this aspect of micro-texturing must be confronted.

An established technique such as photolithography is not immune to this challenge. At Louisiana State University, Kortikar applied a novel method to align a planar mask to a planar substrate [10]. Electrical Discharge Machining (EDM) produced a precise reference mark on the surface of a stainless steel thrust rung. A photomask exhibited a similar mark. Depicted in Figure 3-13, these references could then be aligned using a Karl Suss Mask Aligner—an exposure station comprising microscope objectives and precise linear stages. With average deviations less than 15µm, the alignment marks proved an effective means to properly locate the micro-texture.

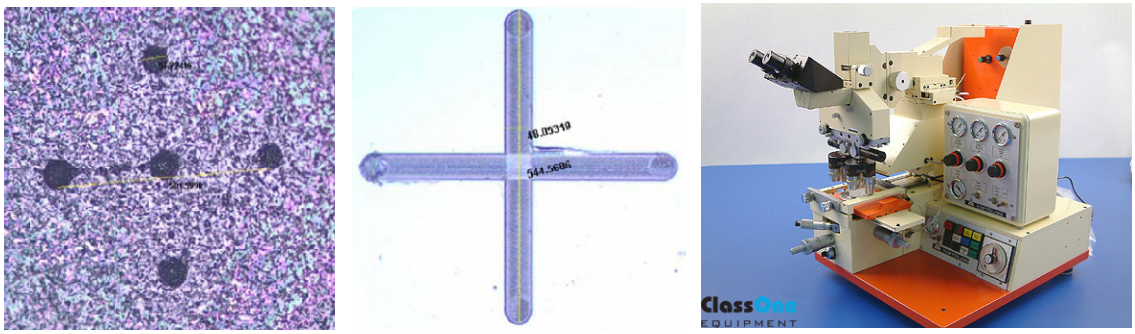

Figure 3-13[10]. Reference marks on the substrate (left) and photomask (center) could be aligned with a Karl Suss MJB3 Mask Aligner (right) to ensure proper micro-texture placement.

When faced with planar masks and non-planar substrates, alignment becomes a formidable task. However, researchers at the University of Kiel developed a custom rotational device to transfer a mask image onto a cylindrical surface via UV-photolithography [23]. By synchronizing the angular velocity of this device with the linear travel of a planar mask, a texture was successfully applied to a 3.5mm diameter glass tube. As shown in Figure 3-14, the resulting pattern exhibited minimal misalignment; further improvements may be achieved with reduced substrate tolerances and finer motor control.

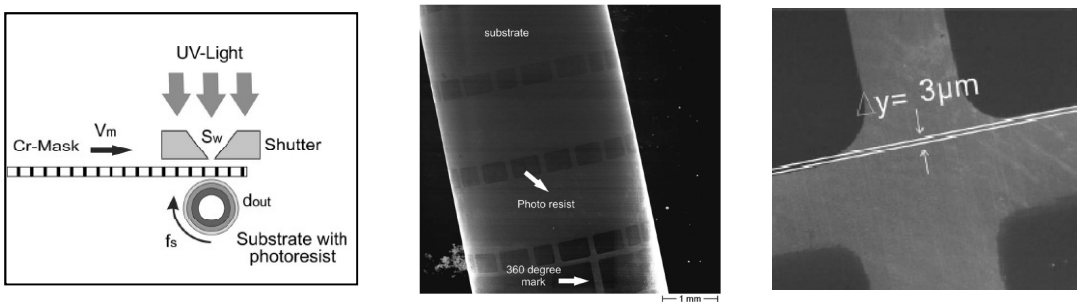

Figure 3-14[23]. As shown in the schematic (left), a rotational device enable micro-texturing of a glass tube (center) with little axial misalignment (right).

Complexity further increases when considering a non-planar mask and a non-planar substrate. The present work faces this challenge. In an effort to apply micro-textures to a conical mold insert, a comparably shaped mask must be mated to the substrate surface. This task is addressed by using an innovative clamping scheme to exploit the conforming geometries of the mask and the mold insert. Shown in Figure 3-15, a plate secured to pre-existing threads introduces a distributed clamping force to the entire perimeter of the photomask. This technique provides insight into micro-texturing as the technology continues to permeate new disciplines.

Figure 3-15. A clamp plate secures a photomask to the conical surface of a mold insert.

CHAPTER 4 – METHODS

4.1 Description of Conical Mold Insert

The core focus of this work rests on a remarkably unusual work piece. Unlike the silicon wafers typical to photolithography studies, the mold insert presents few flat surfaces. Tracing the cross-sectional profile, a brief plateau encounters an abrupt vertical rise that tapers into a precise chamfer. Revolving this profile about a central axis reveals the final form shown in Figure 4-1. A cylinder may be the closest comparison; however, the intricacy of the conical mold insert presents striking challenges to surface engineering. The geometry is undoubtedly peculiar. Micro-texturing this geometry is an equally peculiar and interesting consideration.

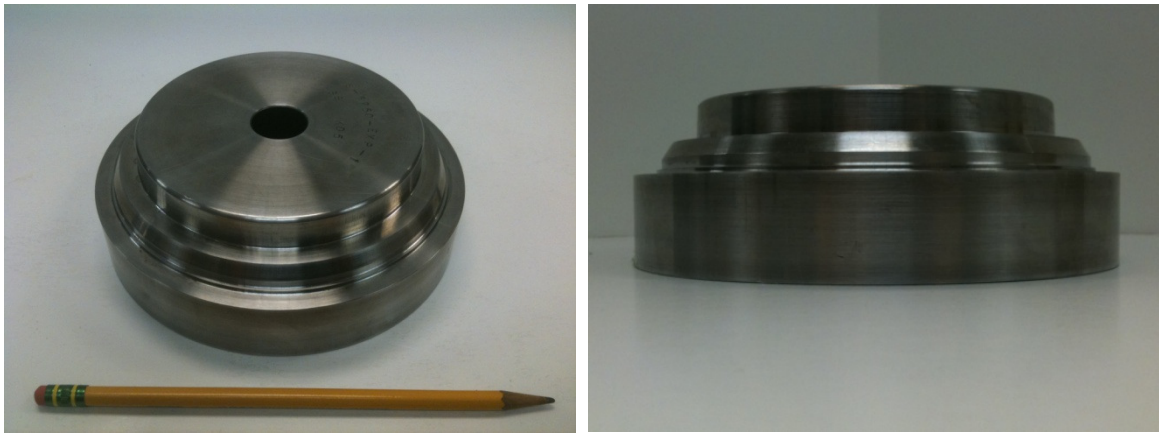

Figure 4-1. Conical mold insert considered for micro-texturing.

Shape of the conical mold insert follows function. A radial lip seal (Federal-Mogul® National® Oil Seals) includes an elastomeric component within a metal housing. As shown in Figure 4-2, the elastomer operates against a rotating shaft and provides a barrier between two environments; in commercial-vehicle applications, this seal prevents lubricant leakage and offers protection against debris contamination [50]. Designed for an interference fit, the elastomer is fitted with a garter spring to compensate for shaft imperfections, misalignment, and part wear. The elastomer plays a crucial role in overall seal performance. Injection molded from nitrile rubber, the proper specifications of this elastomer depend on the unique shape of the conical mold insert.

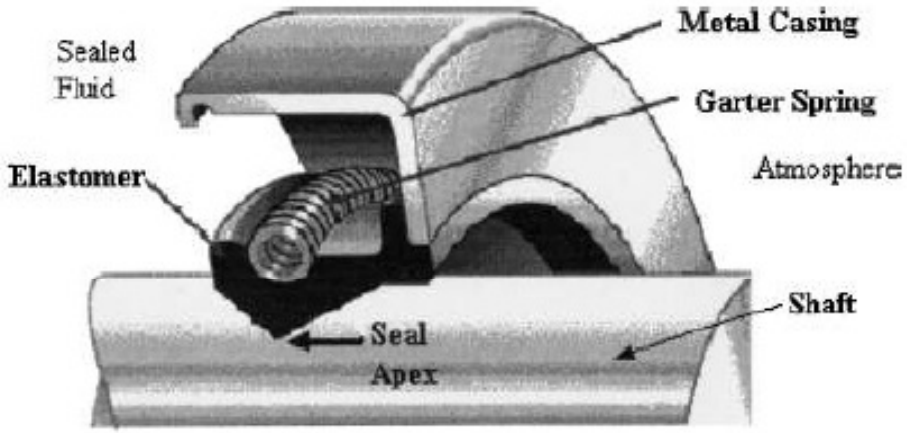

Figure 4-2[50]. The elastomer component of a radial lip seal provides a barrier between lubricant and the atmosphere.

Since the UV-lithography process irreversibly alters the substrate surface, several mock mold inserts were fabricated to preserve the original tooling. Samples were machined from 6" round stainless steel barstock provided by a local metal supplier; designated as SAE type 420, the composition of this alloy is outlined in Table 4-1 [51]. To conserve material and reduce machining complexity, portions of the original mold insert shape were excluded when fabricating the mock versions. As shown in Figure 4-3, these exclusions did not compromise the relevancy of the micro-texturing technique; the surface identified to receive micro-textures remained dimensionally accurate.

Table 4-1 Composition of SAE 420 Stainless Steel[51].

Element	Maximum Percent Composition
Chromium (Cr)	12.0 - 14.0%
Carbon (C)	> 0.15%
Manganese (Mn)	1.00%
Silicon (Si)	1.0%
Phosphorus (P)	0.04%
Sulfur (S)	0.03%

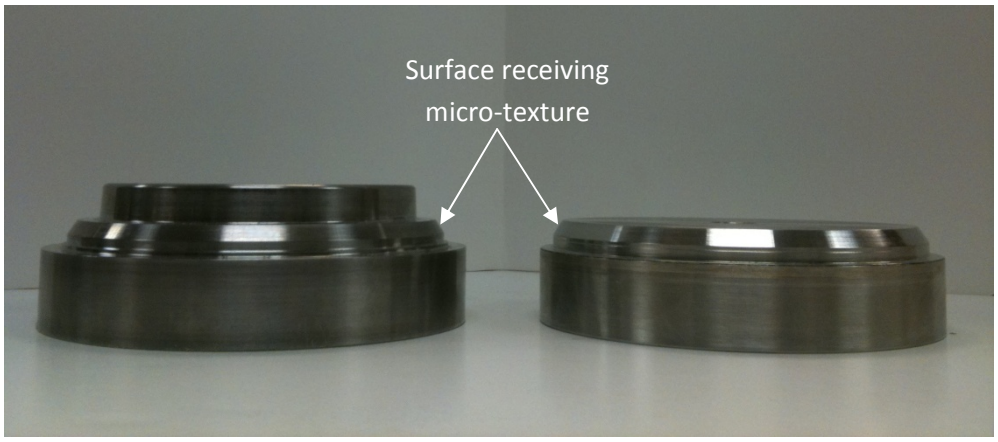

Figure 4-3. Features of the original tooling (left) are excluded from the mock mold insert (right) to simplify machining.

To verify accurate duplication of the original tooling, specifications of the mock mold inserts were measured with various instruments. Using a digital vernier caliper, the bulk dimensions were collected for comparison with machinist drawings (Appendix A). Special consideration was paid to the chamfer angle. Utilizing symmetry and basic trigonometry, this angular dimension could be calculated from the bulk dimensions; any excessive deviation from spec (±½°) was promptly addressed, and the corrected chamfer angle was verified using a machinist's sine plate. Referencing the highlighted dimensions in Figure 4-4, the following Table 4-2 summarizes the measurements acquired for 10 mock mold inserts and the comparative measurements from the original tooling.

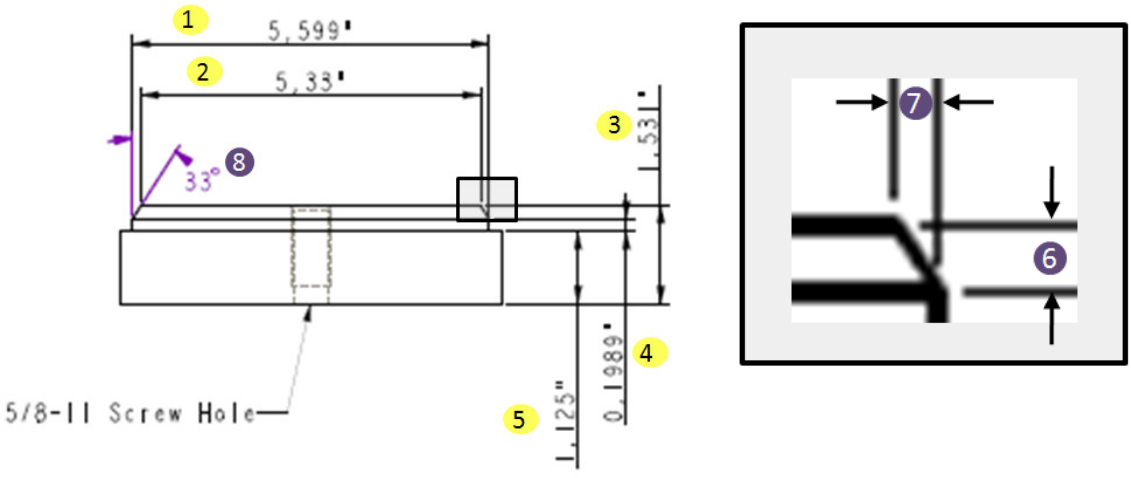

Figure 4-4. Bulk dimensions of the mock mold insert measured (1-5) and the chamfer angle verified by applying symmetry and basic trigonometry (6-8).

Table 4-2 Dimensions of Conical Mold Insert.

Sample	Measured Dimension *(inches)*					Calculated Dimension			Corrected Chamfer Angle
	1	2	3	4	5	6 *(in)*	7 *(in)*	8 *(deg)*	8 *(deg)*
Original	5.599	5.333	1.531	0.199	1.125	0.207	0.133	32.721	--
1	5.599	5.333	1.531	0.199	1.125	0.207	0.133	32.721	33.000
2	5.597	5.331	1.533	0.199	1.127	0.207	0.133	32.721	33.000
3	5.599	5.333	1.497	0.185	1.095	0.217	0.133	31.504	32.500
4	5.597	5.320	1.514	0.185	1.118	0.211	0.139	33.281	--
5	5.599	5.334	1.531	0.190	1.145	0.196	0.133	34.059	32.500
6	5.599	5.303	1.528	0.175	1.136	0.217	0.148	34.295	32.500
7	5.599	5.313	1.543	0.180	1.148	0.215	0.143	33.629	32.500
8	5.599	5.340	1.543	0.199	1.153	0.191	0.130	34.138	32.500
9	5.606	5.363	1.673	0.210	1.273	0.190	0.122	32.598	--
10	5.604	5.336	1.528	0.198	1.122	0.208	0.134	32.791	--

Surface finish was also an important specification to consider. If too smooth, electroplated metal may bond poorly to the substrate, and any engineered surface features would quickly be removed when submitted to the rigors of injection molding. If too rough, photoresist may persist on the surface despite efforts to develop the desired pattern. Moreover, excessive roughness may adversely affect part ejection after molding. A balance must be satisfied.

In the case of the conical mold insert, the average surface roughness (R_a) served as the primary parameter to consider when specifying surface finish. This parameter commonly appears on part drawings, and machinists typically resort to a set of standard specimens to gauge the roughness of a particular surface. The defining equation for average surface roughness is shown below; essentially, this definition accounts for variations in the surface height about a mean plane. In Figure 4-5, this concept is illustrated in a three-dimensional representation.

$$R_a = \frac{1}{ab} \iint |\eta(x, y)| \, dxdy \tag{1}$$

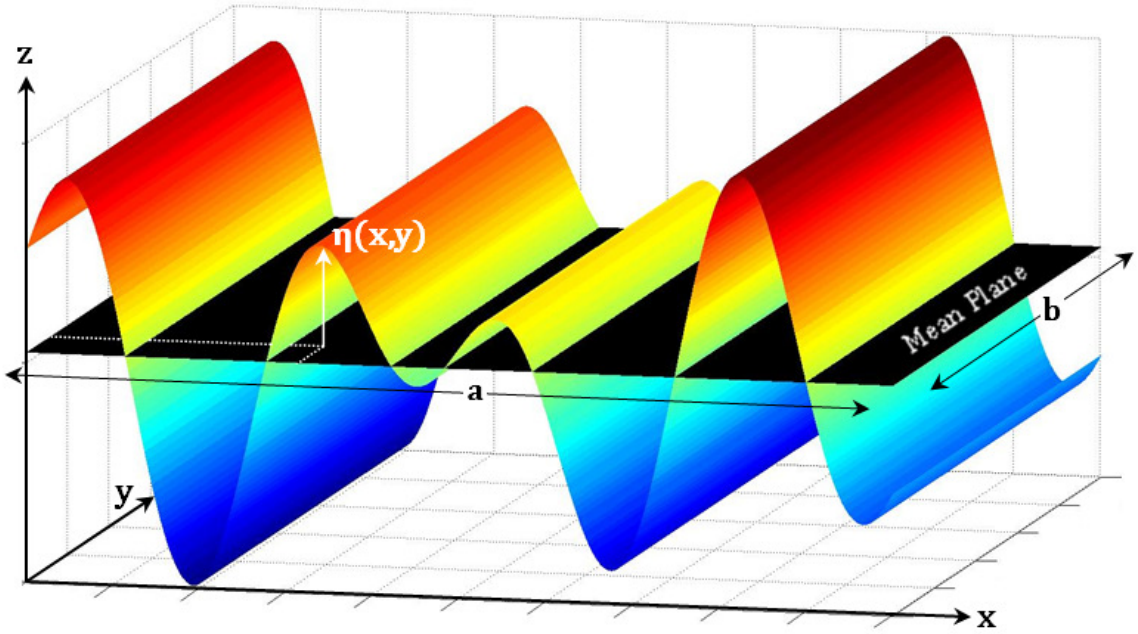

Figure 4-5. Three-dimensional representation of parameters used to define average surface roughness (R_a).

For the mock mold inserts, the surface to receive micro-textures was machined to match the finish of the original tooling within a relatively tight tolerance. The chosen specification designated an average surface roughness ranging from 10-25µinch. Typically, this spec was achieved during the bulk machining performed in a metalworking lathe. If unsatisfactory, the surface was further refined using a grinding wheel. None of the samples required surface roughening; however, if necessary, sandblasting was recognized as a capable technique used in previous micro-texturing studies [33].

To adequately verify surface roughness, samples were measured using a non-contact surface profilometer. The Zygo® NewView™ 5000 system depicted in Figure 4-6 performs measurements by exploiting white light interferometry [52]. Light reflected from the specimen surface can be compared to light reflected from a reference surface; processing the data with a MetroPro™ software package, the results can be translated into a three-dimensional plot. Moreover, the software graphical user interface (GUI) offers access to a variety of powerful algorithms including average surface roughness computation and best-fit geometry removal. As shown in Figure 4-7, the latter feature proved a necessary analytical tool to handle the unique curvatures of the conical mold insert.

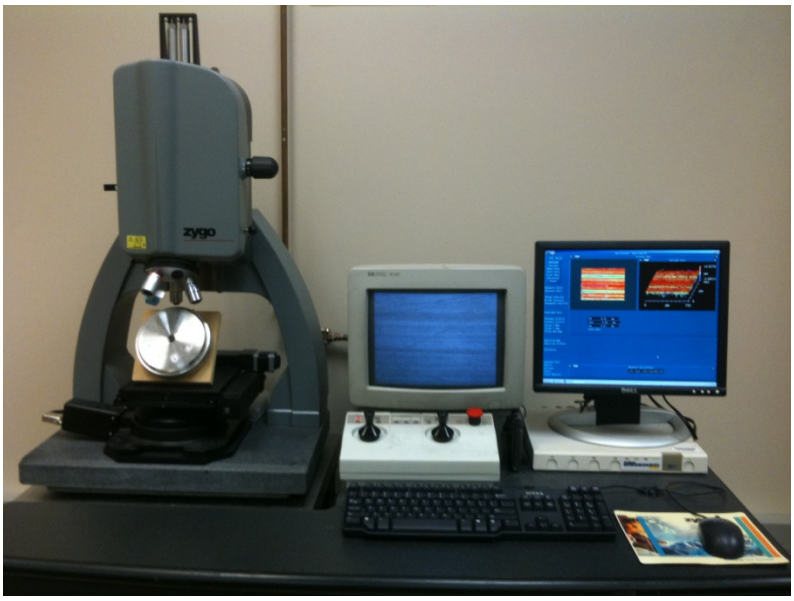

Figure 4-6. Zygo® NewView™ 5000 system.

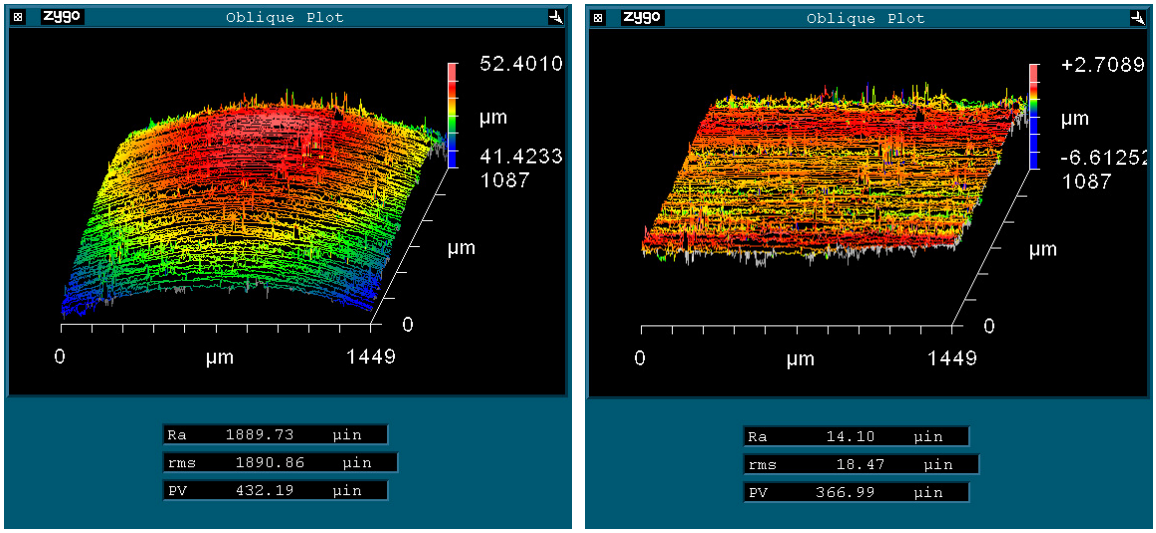

Figure 4-7. Using algorithms integral to MetroPro™ software, a best-fit cylindrical geometry could be removed from the acquired data to facilitate more accurate analysis of surface characteristics (i.e. R_a).

The aforementioned surface profilometer facilitated analysis of average surface roughness. For each mock mold insert, a mean value was based on at least 8 separate measurements equally spaced around the circumference of the specimen as illustrated in Figure 4-8. The original tooling was also inspected for the sake of comparison. To further improve measurement confidence, raw data was exported to MATLAB® for a secondary analysis; specifically, a code was written to emulate the algorithms used by MetroPro™ software to calculate average surface roughness (Appendix B). The results from this data collection and secondary analysis are displayed in the following Table 4-3.

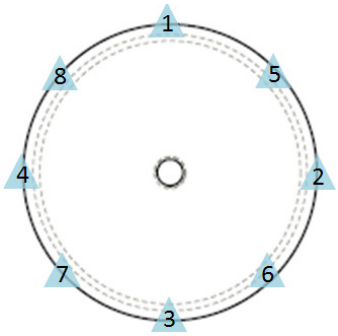

Figure 4-8. Average surface roughness (R_a) evaluated at several locations on each specimen.

Table 4-3 Average Surface Roughness of Conical Mold Insert.

Sample	Average Surface Roughness, R_a (μ-inches) MetroPro™ / MATLAB®								
	1	*2*	*3*	*4*	*5*	*6*	*7*	*8*	***Average***
Original	23.9 / -- 25.8 / --	20.9 / -- 27.3 / --	21.5 / -- 23.5 / --	25.6 / -- 23.2 / --	22.2 / -- 26.6 / --	21.6 / -- 24.5 / --	22.4 / -- 23.3 / --	25.8 / -- 24.7 / --	23.9 ± 1.93 / --
1	24.4 / 24.6	28.3 / 28.5	24.3 / 24.6	23.9 / 24.1	34.2 / 34.8	28.1 / 28.4	24.2 / 24.4	22.2 / 22.5	26.2 ± 3.86 / **26.5 ± 3.96**
2	22.0 / 19.0	20.9 / 18.2	19.9 / 17.8	19.2 / 16.7	21.7 / 20.6	20.1 / 16.9	20.6 / 17.5	20.2 / 17.3	20.6 ± 0.93 / **18.0 ± 1.28**
3	26.8 / 24.2	21.2 / 18.7	26.1 / 24.5	28.2 / 26.6	28.2 / 26.6	26.5 / 23.4	22.9 / 21.4	25.3 / 24.5	25.7 ± 2.47 / **23.7 ± 2.64**
4	18.2 / 18.2	19.0 / 19.0	27.0 / 27.0	23.3 / 23.3	15.9 / 15.9	21.9 / 21.9	25.3 / 25.3	19.1 / 19.1	21.2 ± 3.81 / **21.2 ± 3.81**
5	13.7 / 13.8	13.0 / 13.0	14.1 / 14.1	14.2 / 14.2	13.7 / 13.7	14.5 / 14.5	13.6 / 13.6	13.0 / 13.0	13.7 ± 0.54 / **13.7 ± 0.54**
6	12.0 / 12.0	13.4 / 13.4	13.7 / 13.6	14.4 / 14.4	13.5 / 13.5	12.6 / 12.6	15.4 / 15.3	12.7 / 12.7	13.5 ± 1.08 / **13.4 ± 1.05**
7	14.4 / 14.4	15.7 / 15.8	15.6 / 15.5	15.9 / 15.9	14.1 / 14.1	14.6 / 14.6	16.7 / 16.7	15.3 / 15.3	15.3 ± 0.87 / **15.3 ± 0.87**
8	18.2 / 18.2	20.9 / 20.9	18.8 / 18.8	19.8 / 19.8	20.2 / 20.2	22.1 / 22.1	20.3 / 20.3	20.5 / 20.5	20.1 ± 1.21 / **20.1 ± 1.21**
9	11.9 / 11.8 12.2 / 11.3	12.7 / 12.7 10.6 / 10.4	10.1 / 10.1 9.1 / 8.9	9.4 / 9.4 9.8 / 7.6	11.6 / 11.6 7.9 / 9.6	9.5 / 9.5 9.8 / 7.7	11.1 / 11.2 7.9 / 7.7	10.8 / 10.8 9.8 / 9.6	10.3 ± 1.41 / **10.9 ± 1.16**
10	25.6 / 25.6	27.6 / 27.5	23.6 / 23.8	20.9 / 21.1	21.3 / 21.2	20.1 / 20.2	23.6 / 23.7	33.1 / 33.2	24.5 ± 4.29 / **24.5 ± 4.28**

Slight discrepancies were noticed when comparing values obtained with MetroPro™ to values calculated with the MATLAB® code. This may have been due to errors in data acquisition. Namely, the Zygo® system collects a matrix of surface heights; each value is associated with a particular coordinate in the measured area. In some instances, a surface height was not associated, which resulted in a gap in the matrix. Although the source of error could not be pinpointed, Table 4-4 provides documentation of the occurrences. The MATLAB® code disregarded these gaps when determining average surface roughness. The manner by which MetroPro™ handled these gaps was unknown; the software may have incorporated an interpolation scheme to fill missing data points. Regardless, since the algorithms implemented through MATLAB® were known, the results of the secondary analysis were deemed more reliable. This data hence served as a foundation for future analytical work.

Table 4-4 Erroneous Data Collection by Zygo® System.

Sample	Missing Data Points								
	1	*2*	*3*	*4*	*5*	*6*	*7*	*8*	***Total***
1	1	6	2	1	7	10	0	1	**28**
2	13	13	21	19	27	9	50	7	**159**
3	15	32	40	19	19	14	14	20	**173**
4	3	2	5	0	0	0	2	2	**14**
5	0	0	0	1	0	1	1	0	**3**
6	2	1	0	9	1	5	6	4	**28**
7	1	2	0	0	0	52	1	4	**60**
8	12	1	1	2	1	3	5	6	**31**
9	5 6	2 14	3 3	3 6	1 8	2 19	0 15	0 8	**95**
10	1	14	1	0	1	1	0	1	**19**

For a majority of mock mold inserts, the surface finish fell within the specified limits. However, at least one sample approached the upper boundary and one sample the lower boundary. Reworking these samples was considered, but this step might have further exacerbated deviations from the specifications. For the present study, these samples were decidedly sufficient; furthermore, these extremes offered insight into designing appropriate dimensional tolerances.

Besides surface finish of the conical mold inserts, alignment of the threaded thru-hole was another important consideration. This hole was a pre-existing feature in the original tooling. To facilitate masking during the UV-lithographic process, it was exploited to secure a clamp plate. Ensuring an evenly distributed clamp pressure relied on accurate machining. In particular, the thru-hole axis needed to intersect the mold's top planar surface at a perpendicular angle. This specification was verified by securing the clamp plate to the mold; if gaps were observed, these were measured using digital calipers. As shown in Figure 4-9, the maximum gap measurement (y) was combined with simple trigonometry to evaluate thru-hole alignment (θ).

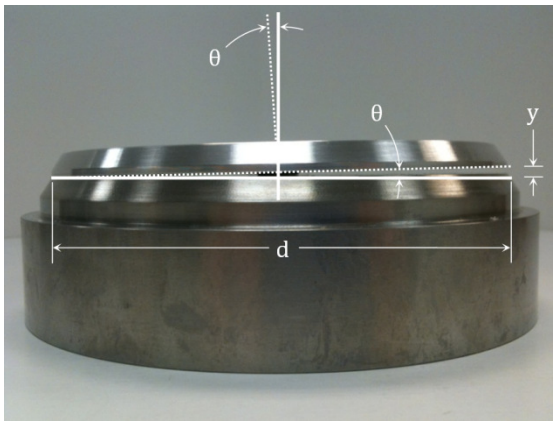

Figure 4-9. After securing the clamp plate, observed gaps enabled calculation of thru-hole misalignment.

Misalignment was calculated by applying the equation below. Results are summarized in Table 4-5; only three of the samples were found to have a detectable misalignment, and the threaded thru-hole was reworked to eliminate this issue.

$$\theta = \tan^{-1}\left(\frac{y}{d}\right) \tag{2}$$

Table 4-5 Misaligned Thru-Hole.

Sample	Diameter, d (*inches*)	Gap, y (*inches*)	Thru-Hole Misalignment, θ (*deg*)
Original	5.333	0.000	0
1	5.333	0.009	0.1
2	5.331	0.000	0
3	5.333	0.000	0
4	5.320	0.000	0
5	5.334	0.009	0.1
6	5.303	0.000	0
7	5.313	0.008	0.09
8	5.340	0.000	0
9	5.363	0.000	0
10	5.336	0.000	0

4.2 Description of Photomask

The photomask is a reflection of the desired surface texture; this texture is a reflection of progressive studies. Based on a numerical analysis of radial lip seals, Hadinata demonstrated the potential of deterministic microasperities on the shaft [39]. Realizing this setup in an experimental study, Warren supplied evidence that specific shaft textures elicited considerable friction reductions as well as a preferential pumping phenomenon [13]. Shinkarenko provided further innovation; in collaboration with Etsion, a theoretical study suggested the potential of microasperities on the elastomer [40]. An appropriate photomask may prove the crucial link to actualizing this textured elastomer.

Design of the photomask reflected two scientific pursuits. First, prove the capability of UV-lithography to micro-texture a conical mold insert. The bulk shape of the mask developed from this goal. Secondly, experimentally demonstrate the potential of a textured elastomer to reduce friction and pump preferentially. The intricate mask pattern emerged from this objective.

When dimensioning the bulk shape of the mask, a simple right circular cone served as the foundation to understanding. As shown in Figure 4-10, a three-dimensional cone is formed from a circular section. The measurements of the required circular section depend on desired cone specifications. Applying basic trigonometry, radius of the circular section (r_c) is a function of the cone base radius (r_b) and the cone pitch angle (α). Recalling the concept of arc length (s), the sweep angle (θ) of the circular section is simply a function of the cone pitch angle. The following equations summarize these relationships.

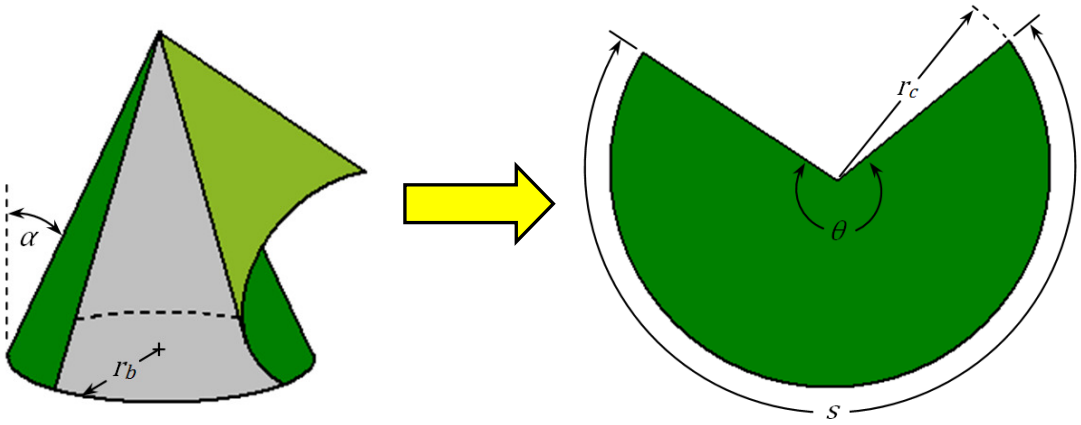

Figure 4-10. A right circular cone (left) formed from a circular section (right).

$$r_c = \frac{r_b}{\cos(90 - \alpha)} \tag{3}$$

$$\theta = \frac{s}{r_c} = \frac{2\pi \cdot r_b}{r_b/\cos(90 - \alpha)} = 2\pi \cdot \cos(90 - \alpha) \tag{4}$$

In actuality, the mask conformed to a frustum; recognizing this shape as the difference of two cones, the previous methods could be extended to determine proper dimensions. As figure 4-11 suggests, radii of the circular strip depended on radii of conical sections. This relationship is represented in the following equations. The sweep angle was unaffected as this value remained dependent only on the cone pitch angle.

$$r_{c,1} = \frac{r_{b,1}}{\cos(90 - \alpha)} \tag{5}$$

$$r_{c,2} = \frac{r_{b,2}}{\cos(90 - \alpha)} \tag{6}$$

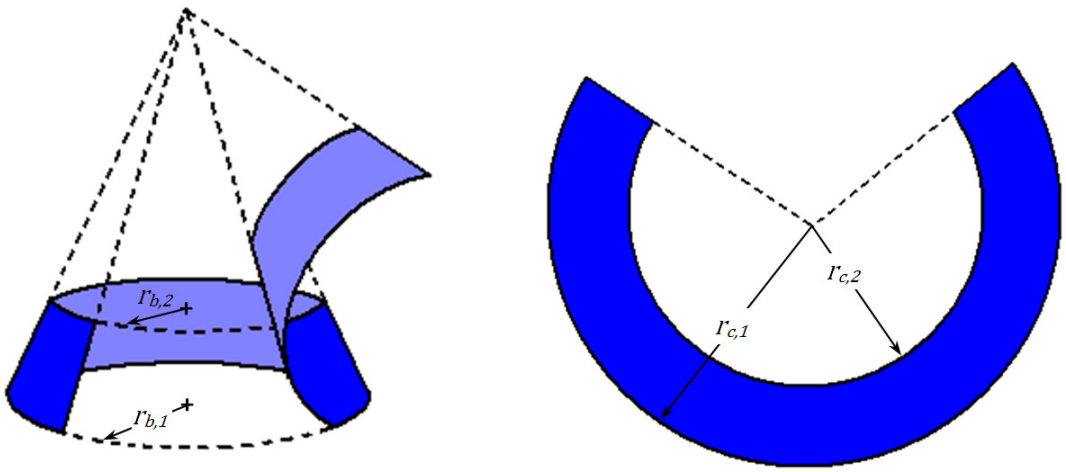

Figure 4-11. Frustum (left) formed from a circular strip (right).

With measurements from the conical mold insert, the previous equations were applied to design the planar image of the photomask. This two-dimensional image could then be transformed into a three-dimensional form by attaching the appropriate edges with clear adhesive tape. To improve adhesion, extra material was intentionally added to the mask by slightly increasing the outer radius of the planar image. This modification is portrayed in the final part drawing of the photomask's bulk geometry (Appendix C).

The overall mask geometry was dictated by shape of the conical mold insert; however, the mask pattern offered some design freedom and allowed consideration for the molded elastomer's future potential. With this in mind, the pattern was engineered towards manufacturing micro-cavities as opposed to micro-asperities. As illustrated in Figure 4-12, this decision maximized the integrity of photoresist during the lithography process. Beyond this consideration, the design offered a degree of flexibility. To exploit this flexibility, effort was focused on mimicking the designs used by Warren; her work investigated fields of triangular cavities oriented in certain directions to elicit desirable dynamic behavior [13]. The present study incorporated a comparable pattern into the photomask.

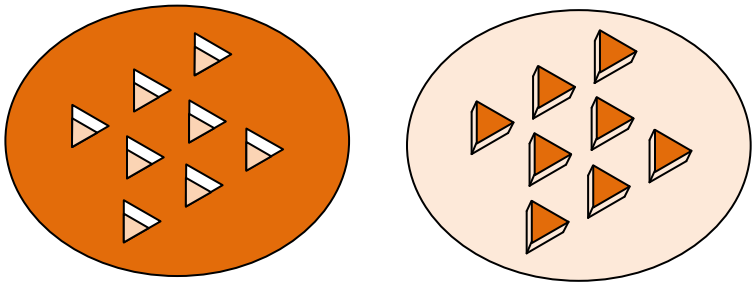

Figure 4-12. Micro-textures built from cavities in photoresist (left) are preferred to textures built around asperities (right) to maximize photoresist integrity and adhesion.

Understanding the pattern design requires thoroughly grasping the relationship between mask image and the final molded elastomer. Referring to Figure 4-13, consider first the image of triangles printed onto a mask. When dealing with a negative-acting photoresist, the printed regions correspond to areas of resist intended for removal. Upon photoresist development, the resulting template comprises a field of triangular cavities. These cavities provide access to the bare metal substrate beneath, and if submitted to an electrodeposition process, these empty cavities are replaced with metal posts. In subsequent injection molding, a field of these metal posts imprints a field of depressions in the elastomer. Thus, an identical geometry is shared between the final elastomer and the initial mask image.

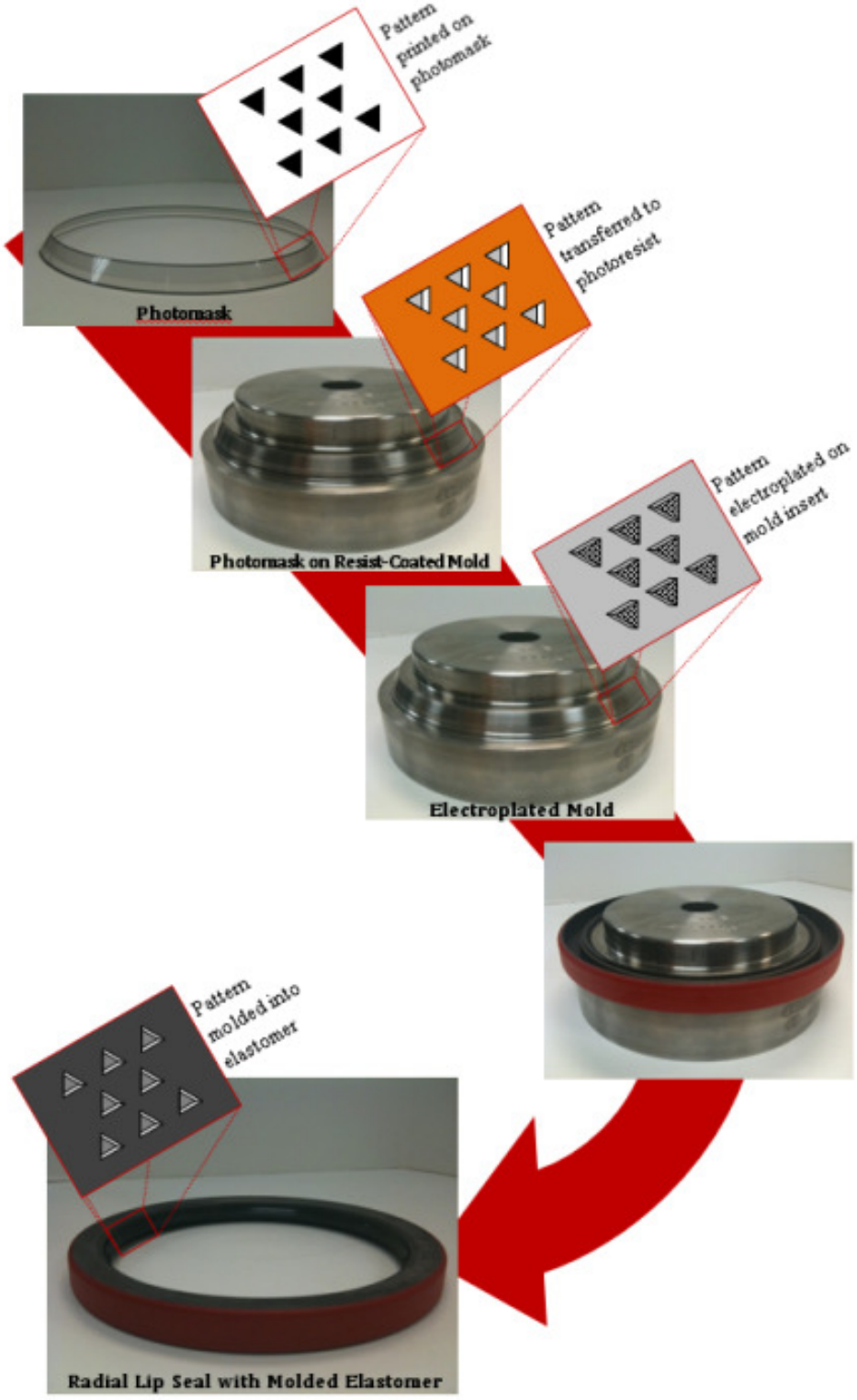

Figure 4-13. Illustration of relationship between mask image (top) and the final molded elastomer (bottom), which is mounted in a finished radial lip seal. Patterns not shown to scale.

With proper orientation of a triangular pattern, Warren demonstrated that friction could be drastically reduced over 50% and absolute pumping rate could be simultaneously maximized [13]. The present study attempted to implement this pattern. With a base measuring 107μm and a height of 78μm, dimensions of the isosceles triangles exactly duplicated that used by Warren. However, the spacing around the triangles was slightly modified; unlike a straight masking strip, the planar image of the conical mask introduced a curvature. To account for this, the circumferential spacing between triangles increased slightly with each successive row of the pattern. Spacing of the initial row resembled that used by Warren; as shown in Figure 4-14, spacing in subsequent rows was dictated by radial guidelines.

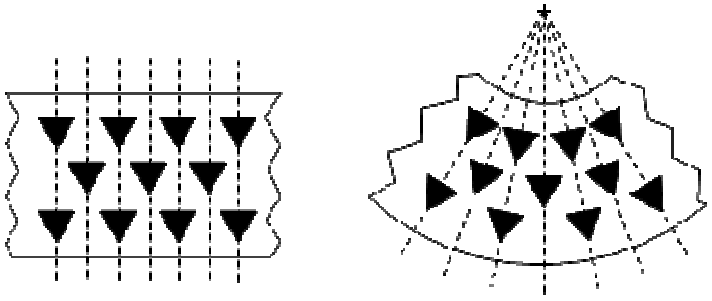

Figure 4-14. Compared to a straight masking strip (left), spacing was adjusted to account for curvature of the conical mask (right). Patterns not shown to scale.

Consequently, this modified spacing negated a useful condition—the unit cell. In previous numerical studies, the unit cell comprised a micro-feature surrounded by a consistent area, which provided periodic symmetry in the circumferential direction [39]. This greatly simplified modeling. However, the unit cell does not apply to the present study. That is, triangles in one row are surrounded by a different area compared to features in the adjacent rows. As a possible remedy, a consistent area ratio might have been achieved by varying the triangle sizes. However, such adjustment would adversely affect downstream processing; in particular, the electroplating step would suffer [18]. Smaller triangular features would be deposited at a higher rate than larger ones leading to irregularities in plating thickness.

Final design for the mask pattern was documented via CAD software (AutoCAD® R14). To manufacture a physical mask, part drawings were generated and submitted to a precision printing vendor (Appendix D). Headquartered in Minnesota, Infinite Graphics Incorporated specializes in creating high-resolution masks for photolithography applications. Services were employed to produce a sufficient inventory of plastic masks for the present study; Figure 4-15 displays a sample of the final printed image.

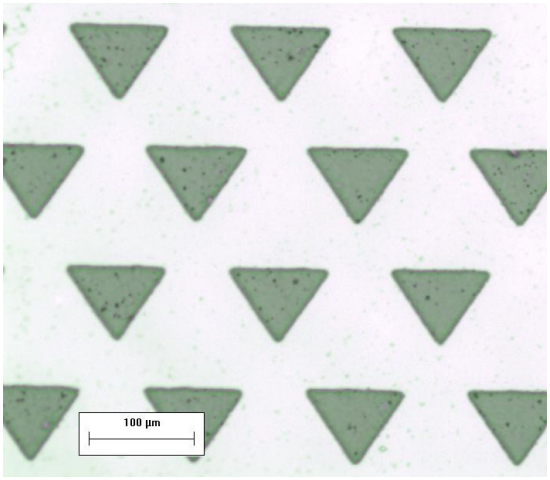

Figure 4-15. Sample of printed mask captured by optical microscopy.

With several full patterns duplicated on a large plastic film, cutting out the mask profiles was a critical step toward the finished product. An imprecise cut would have contradicted any prior efforts to design a form-fitting mask. To avoid this issue, three excision methods were developed: (i) hand-cutting by scissors; (ii) cutting with a custom jig; and (iii) cutting with a die. As expected, scissors proved highly dependent on the skill of the operator; the resulting parts exhibited jagged edges and poor repeatability. A jig provided improvements. As shown in Figure 4-16, this jig comprised a circular mat cutter purchased from a local craft store and an aluminum pressure plate machined to match the mask curvature. Though this method achieved smoother edges, the blade tended to stray from the desired path. As a final remedy, the precision printing vendor offered a die-cut solution. By translating the mask outline into a continuous blade contour, each mask image could be excised with precision and repeatability.

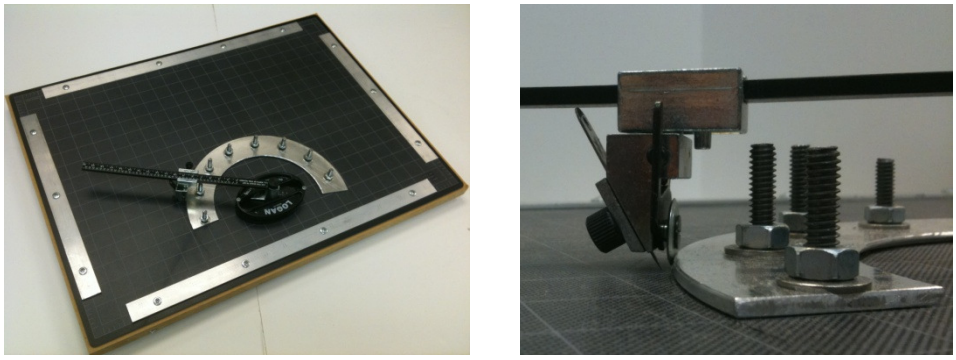

Figure 4-16. Jig (left) comprising a mat cutter and aluminum pressure plate (right).

4.3 Procedure for UV-Lithographic Patterning

Since inception, lithography techniques have gradually progressed. Alternative photoresist formulations and exposure sources have allowed major shifts in both the process and application [10,20]. The present study adopts this innovative mindset in an effort to further expand the technology. Spanning the course of three-days, a modified manufacturing method accommodates the unique geometry of a mold insert in hopes of micro-texturing the conical surface.

4.3.1 Day 1 – Surface Cleaning and Photoresist Application

Surface contamination may negatively impact photoresist adhesion and bond strength of electroplated nickel. To avoid these issues, several cleaning methods were implemented including acid treatment, degreasing, and ultrasonic bath. By eliminating microscopic organic debris, these techniques prevented formation of a weak boundary layer that would be detrimental to adhesion on the stainless steel substrate [53,54].

Using a non-conductive plastic shaft, the mock mold insert was first suspended in a solution of acetic acid (71%), chromium trioxide (24%), and water (5%). The submerged mold was surrounded by a stainless steel drum as shown in Figure 4-17. A wire soldered to the mold surface and a wire attached to the drum provided connection points for a potentiostat. Operating in a galvanostat mode, this instrument supplied a constant current (0.5A) between the anode (mold insert) and the cathode (steel drum). This setup drove a movement of metal ions from the mold surface to the drum, which effectively removed a thin layer of metal from the mock mold.

Figure 4-17. In preparation for photoresist application, the mock mold insert is submerged in an acidic solution.

Following acid treatment and a thorough rinse in de-ionized water, the work piece was processed through a compilation of degreasing steps. First, the mold insert was submerged in a bath of boiling isopropyl alcohol for approximately 10 minutes, which was immediately followed by suspension in alcohol vapors for another 5 minutes. The next step utilized a proprietary cleaner (Caswell SP Degreaser). Available in powder form, a degreaser solution was prepared per the manufacturer's instructions. The mock mold was submerged in this solution for 20 minutes; a solution temperature of roughly 40°C was sustained via hotplate, and light agitation was provided by a magnetic stirrer operating at 200rpm. After submersion, another rinse in de-ionized water removed any residual solution from the substrate surface.

Ultrasonic cleaning has been shown to improve cleaning efforts [53]. Placing the mold insert within a wide-mouth 2000mL glass bowl, approximately 1L of acetone was added to completely submerge the work piece. This setup was then transferred to an ultrasonic bath (Cole-Palmer Model #8893), and the bowl was surrounded with water. Providing a 40kHz frequency, the ultrasonic bath in acetone continued for 4 minutes. With gloved hands, the sample was then removed and wiped dry using low-lint absorbant cloth (Kimwipes®). Afterward, a commercial cleaner (EZ-Clean™ All Purpose Hand Cleaner) was applied with gentle agitation. Following a de-ionized water rinse, the mold insert dried in a convection oven at a temperature of 110°C for 20 minutes. Lastly, an additional 7 minute ultrasonic bath in isopropyl alcohol was followed by two successive, 2-minute submersions in acetone ultrasonic bath.

The aforementioned cleaning prepared the conical mold insert for a crucial step—photoresist application. Throughout literature, a variety of techniques have been investigated to improve the quality and uniformity of deposition. Spin coating predominates in planar applications [7,10,14,15,33]. By adjusting rotational speed and photoresist viscosity, layers can be applied with highly predictable and consistent thicknesses. Alternatively, meniscus and capillary coating methods introduce an upside-down substrate directly to a reservoir of photoresist, which significantly reduces material waste compared to spin coating [15]. However, when considering non-planar applications, gravity presents challenges to these methods. To circumvent this issue, several studies have focused on mechanically clamping a preformed polymer template to the substrate [1,5,19]. Post-machining of a cast photoresist layer may also compensate for gravity-induced thickness variations [5,17].

The present work exploited a spray method. Despite past critics, recent findings support the potential of spray application, especially in regards to non-planar substrates [15,55]. To achieve this potential, careful attention must be shared among several process variables including solids content, solvent evaporation rate, incidence angle, and distance between spray nozzle and substrate [55,57]. Successfully balancing these parameters can provide exceptional reproducibility and a uniformity that rivals conventional spin-coating [55].

Located in Massachusetts, the MicroChem Corporation manufactures Microspray™–a line of commercially available photoresist products engineered into aerosol form. The current study employed two such products: (i) a proprietary formulation known as XP Microspray™ Negative and (ii) an adapted SU-8 formulation known as XP SU-8 Microspray™. As negative photoresists, both products exhibit similar chemical behavior upon ultraviolet exposure; SU-8 formulations generate strong acids when irradiated [20]. In subsequent heat treatment, this photoacid catalyzes a cross-linking reaction. Thus, exposed regions become solidified whereas unexposed regions are susceptible to chemical removal.

Photoresist application was performed within a spray booth constructed inside a chemical fume hood. To facilitate coatings, the mock mold insert was placed on a pivoting platform with 360° rotational motion as shown in Figure 4-18. Focusing on a single eighth section, the spray nozzle was distanced approximately 3" from the surface per the manufacturer's recommendation [16,56]. To avoid the appearance of pinholes within the photoresist, the spray stream was administered normal to the desired surface [57]. Spray was dispensed to each eighth section in a smooth back and forth sweeping motion. A full revolution constituted a single coat. For increased thickness, successive coats were applied 5 minutes apart.

Figure 4-18. Working within a spray booth (left), a pivot platform (center) facilitated spray application (right) of Microspray™ photoresist on the conical mold insert.

After spray-coating, the mold insert was stored in a dark location overnight. Bubbles inadvertently created within the photoresist during application were able to dissolve during this time. Otherwise, these pockets of air may have lead to pronounced gaps in coverage; these gaps would have translated to undesirable anomalies in the developed photoresist. The absence of ambient light ensured that photoacid generation would not cause premature cross-linking and solidification of the resist.

4.3.2 Day 2 – Bake and Exposure

Processing during the second day represented a culmination of knowledge and experience spanning several decades of lithography research. By precisely controlling the location and duration of chemical reactions in the photoresist, a microscopic pattern can be achieved. Ultraviolet exposure provokes formation of a catalyst. This catalyst instigates cross-linking of molecular branches. Finally, heat drives the reaction to completion.

Prior to irradiation, the resist-coated mold insert received a preliminary heat treatment. Several concerns had to be balanced during this prebake step. Pattern quality may suffer if insufficient heat applied, and the photoresist may inadvertently adhere to the masking element [14]. However, a shorter prebake may improve aspect ratio and pattern fidelity [6]. Too much heat may desensitize the resist to subsequent UV exposure [10]. Applying or removing heat too quickly may create thermal stresses that degrade surface adhesion [18]. With proper application, a prebake effectively removes solvents, relieves internal stresses, and promotes adhesion of photoresist to the substrate [10]. In the present study, a convection oven heated the work piece at a temperature of 60°C for a period of 30 minutes followed by 70 minutes at a temperature of 100°C. With oven door closed, heat application was then stopped, and the mold insert cooled slowly for 3 hours.

Masking followed this prebake. As mentioned previously, bulk geometry of the mask was designed such that the desired 3-dimensional structure could be created from a planar 2-dimensional image. With gloved hands and tweezers, the appropriate edges of the mask were joined by a strip of transparent packing tape measuring approximately 1/8” wide. In addition, another tape strip was applied to the non-patterned region of the mask juncture to increase its integrity. Figure 4-19 depicts the mask in its initial planar form and final conical shape.

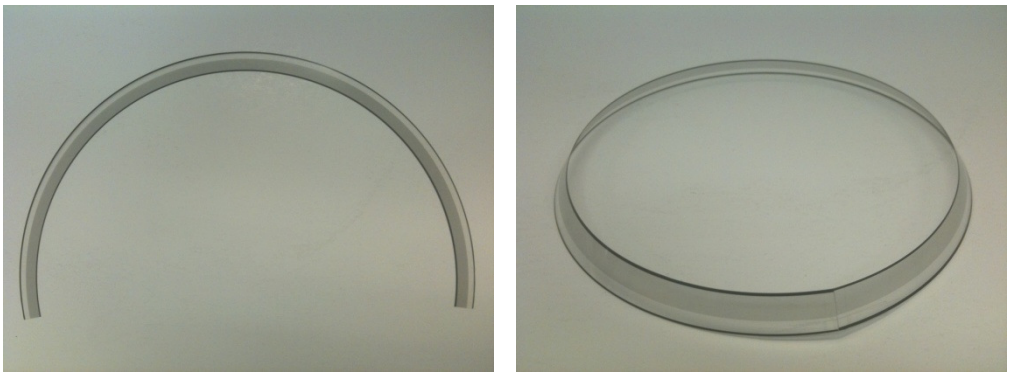

Figure 4-19. Planar image (left) used to construct the final form of the photomask (right).

For applying the photomask, several considerations influenced the approach. Foremost, modifications to the conical mold insert required thorough scrutiny. Any features machined into the mold—whether they were alignment pinholes, tapped machine holes, or reference marks—could compromise the substrate's primary function as a template for injection molding. In addition, the success of UV exposure depended on intimate contact between the mask and the substrate [6]. Air gaps due to inadequate contact could allow excessive light diffraction, which negatively impacts pattern quality [58].

A clamp plate addressed the aforementioned considerations. By exploiting pre-existing threads in the mold insert, unnecessary machining was avoided. Fabrication by a conventional metal lathe ensured perpendicularity between the clamping surface and the threaded stud axis; this facilitated an evenly distributed pressure along the entire photomask perimeter. Preliminary tests supported this notion. However, these tests also revealed an unforeseen consideration. As shown in Figure 4-20, if the outer lip of the clamp plate protruded excessively, regions of photoresist risked under-exposure due to a shadowing effect. This risk was eliminated with a simple turning operation, and the clamp plate design was finalized (Appendix E).

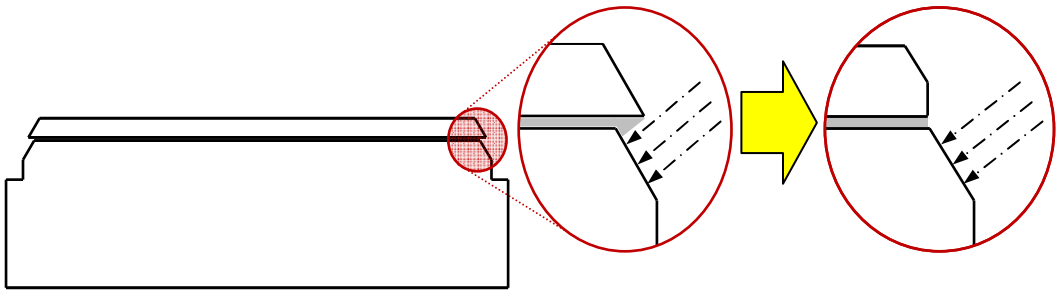

Figure 4-20. Machining step implemented to avoid a potential shadow cast by protruding lip of clamp plate.

Photoresist and mask application precluded one of the most critical factors of photolithography—exposure [8]. Ultraviolet light must be delivered at appropriate wavelengths to adequately penetrate the resist layer, and the dosage must be selected to optimize quality of the desired pattern. Underexposure decreases the generation of catalytic photoacids required to promote molecular cross-linking; photoresist becomes susceptible to degradation during ensuing process steps [59]. Overexposure may lead to expanded structures with poor dimensional accuracy [60]. Moreover, it may induce easier delamination of resist in subsequent heat treatments [61]. However, a negative-acting resist such as SU-8 has been shown to endure exceptionally high dosages with little concern for damage [5].

With an assortment of specialized equipment, the present study administered varying exposure dosages to the substrate. Furnished by ABM Incorporated, a stand-alone ultraviolet exposure station offered adjustable power settings. Measuring light intensity at a wavelength of 365nm, power was set to achieve approximately 26.56mW/cm^2 as sensed directly beneath the lamp bulb. A stage placed beneath the lamp introduced a 0.22cm wide slit to help collimate light. When positioning the mold insert beneath the ultraviolet source, care was taken to ensure light encountered the desired surface at a normal angle [30]. Accomplishing this feat required use of a custom jig fabricated by Daniel Impellezerri for previous work at the Bearing and Seals Laboratory. As shown in Figure 4-21, this jig facilitated the necessary orientation, and it also provided a controllable rotation. Using a controls program developed with National Instruments™ Labview™ software, the conical mold surface was revolved through the path of ultraviolet light at a constant rate of 0.825rpm.

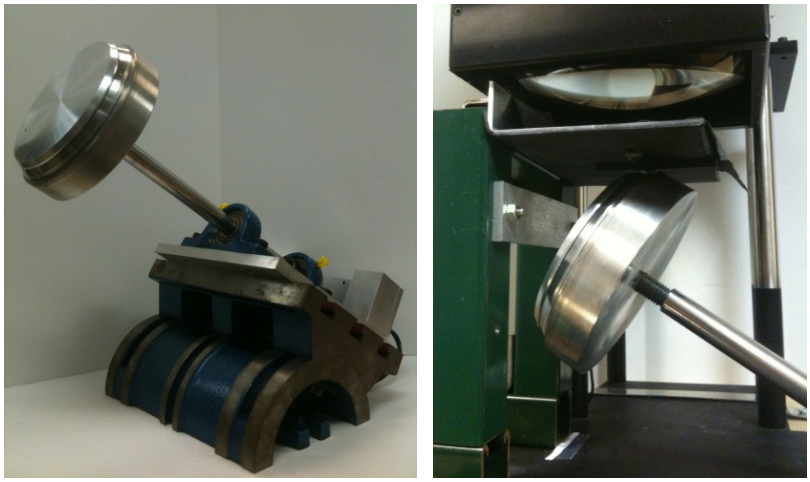

Figure 4-21. Jig developed by Impellezerri to position and rotate conical mold insert beneath ultraviolet source.

With constant light intensity, the dosage depended on the overall time of exposure. This relationship became evident by considering a point (P) on the rotating mold surface. As shown in Figure 4-22, the mold radius (r) and basic trigonometry could be combined to determine the angular displacement (θ) necessary to move this point through the width of the collimating slot (x). Recalling the constant rotational speed (ω), this angular displacement could be translated to a time interval. For each revolution of the mold insert, this singular point would pass through light of fixed intensity (I) for a determinate length of time. Thus, energy delivered to that point during a single rotation (e) could be calculated with the equations below.

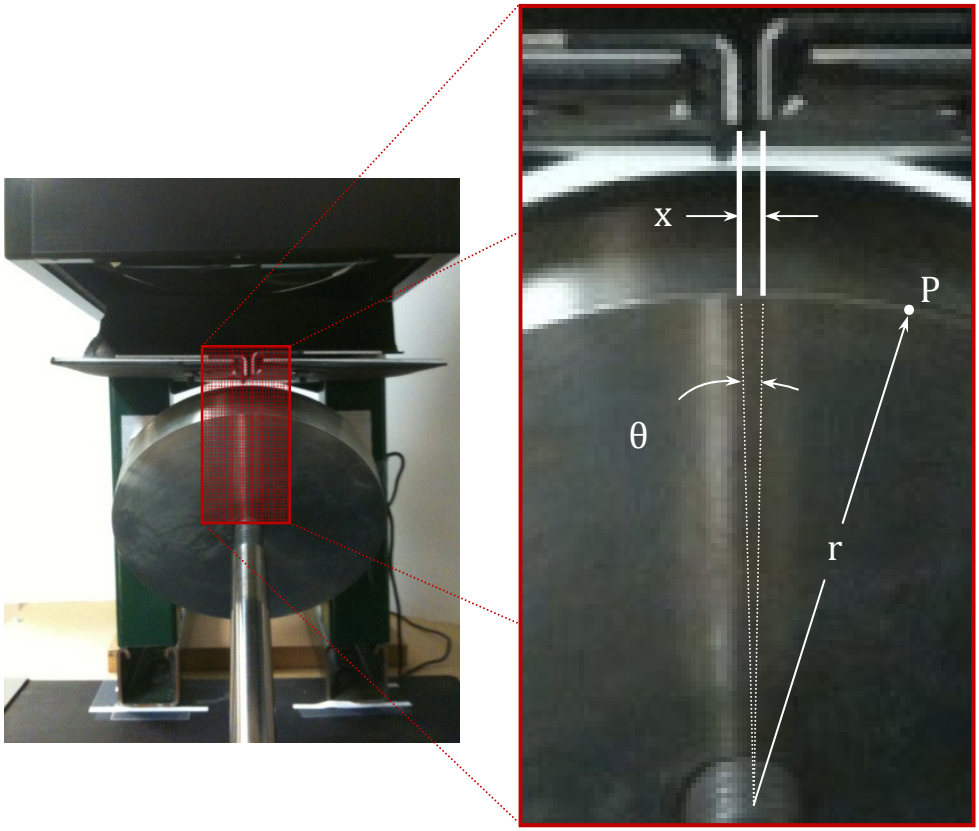

Figure 4-22. Illustration of parameters used to determine angular displacement (θ) of conical mold insert during exposure.

$$\sin\left(\frac{\theta}{2}\right) = \frac{x/2}{r} \rightarrow \theta = 2 \cdot \sin^{-1}\left(\frac{x/2}{r}\right) \quad (6)$$

$$e = I \cdot \left(\frac{\theta}{2\pi \cdot \omega}\right) \quad (7)$$

Achieving the desired dosage (*E*) then relied on providing sufficient rotations (*rev*) to repeatedly introduce this single point into the beam of ultraviolet light. The proper number of rotations could be realized by applying the constant angular velocity for a specified duration—this duration equated to the overall time of exposure (Δt). The governing relationship is summarized by the following expression.

$$E = e \cdot rev = [I \cdot \left(\frac{\theta}{2\pi \cdot \omega}\right)][\omega \cdot \Delta t] \;\rightarrow\; \Delta t = \frac{2\pi \cdot E}{I \cdot \theta} \tag{8}$$

Upon exposure to ultraviolet light, photoacids generated within the photoresist catalyze a cross-linking reaction. This chemical activity occurs relatively slowly at room temperature. To accelerate the process, an additional heat treatment can be applied to drive the reaction forward. Several concerns are associated with this post-exposure bake (PEB). For instance, a suboptimal PEB may cause internal stresses within the photoresist. Rapid heating and cooling could magnify mismatches in thermal expansion coefficient; resulting stresses at the substrate-photoresist interface could lead to delamination issues [14,59,61]. Moreover, an inappropriate PEB could produce unacceptable pattern distortions [6]. Adjusting temperatures and baking duration may avoid these issues. However, lower temperatures may impede the desired chemical reaction, and compensating with longer bake times could allow unintended photoacid diffusion [59]. Previous research has suggested the benefits of ramping techniques to manage heat and internal stresses, but the degree of benefit has been shown to plateau [33,62].

In the present work, the exposed mold insert was unmasked and promptly placed in a convection oven. Temperature was increased from ambient to 60°C and held for 20 minutes. Next, temperature was increased to 80°C and maintained for another 20 minutes. Finally, a temperature of 100°C was set and maintained for 1 hour and 25 minutes. With door closed, the convection oven was then turned off and the sample cooled overnight. The temperature profile is depicted in the following Figure 4-23.

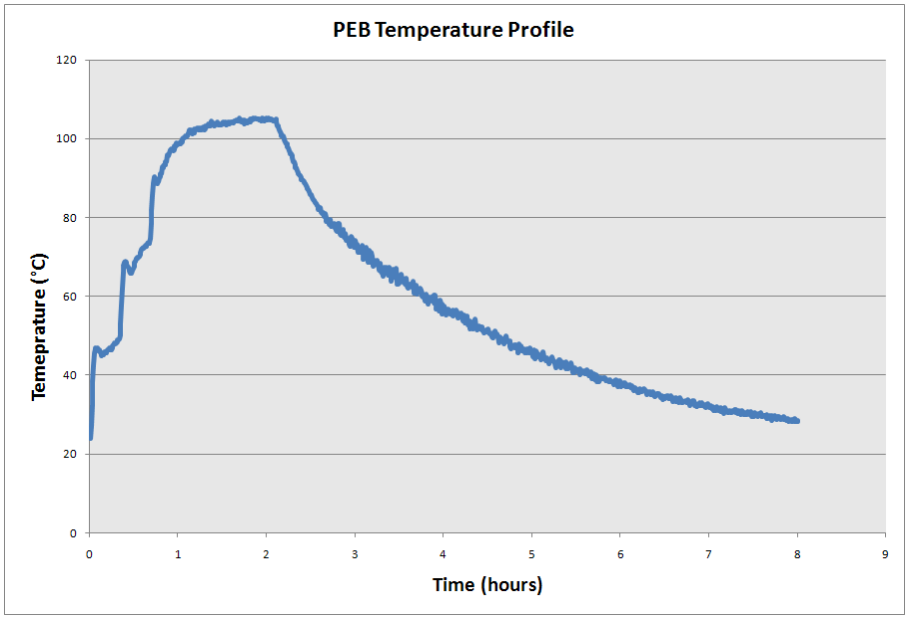

Figure 4-23. Temperature profile applied during post-exposure bake.

4.3.3 Day 3 – Development, Electroplating, and Removal

The success or failure of previous processing became apparent during the final day. Upon development, a pattern emerged from the resist-coated surface. This pattern provided a template for subsequent nickel electroplating. After removal of any remaining photoresist, the quality of surface texturing was revealed.

Development relied on dissolution rates. Regions of photoresist exposed to ultraviolet light exhibit a cross-linked structure less susceptible to solvents. Unexposed areas lack this structure and dissolve more rapidly. Thus, exposure provides control of dissolution. Moreover, the action of solvents can be augmented by varying developer temperature and duration. Low temperatures may expand feature size while high temperatures provide the opposite effect; the current study utilized room temperatures to ensure straight sidewalls within the micro-features [63]. Time could be increased to ensure thorough development at the risk of unintentionally removing exposed photoresist. In the present work, the mold insert was submerged in proprietary solutions recommended by the manufacturer [16,56]. A slight agitation was applied by a magnetic stirrer operating at 400rpm. The appropriate duration of development was judged by incrementally removing and inspecting the substrate surface via optical microscopy.

Following sufficient development, a snapshot of the conical surface was captured using the Zygo® system. Specifically, a total of 8 sample areas were measured on each mold insert. As shown in Figure 4-24, the data could then be stored and viewed in bitmap format to facilitate qualitative observations. Various forms of quantitative analysis were available through the Metropro™ software package. In addition, the data could be exported to MATLAB®—a third party software program offering an extensive toolset for mathematical analysis.

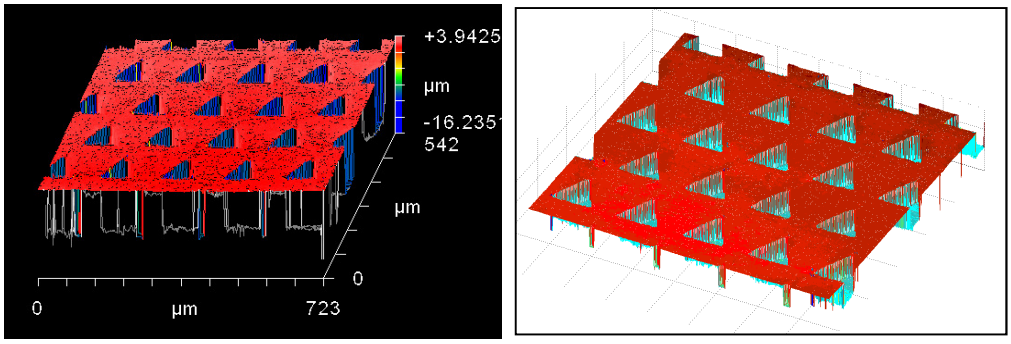

Figure 4-24. After development, a surface measurement captured with Zygo® system (left) and visualized in MATLAB® (right).

Electroplating follows development. In a plating solution, an electric current etches positively charged metal ions from a sacrificial anode, and these ions travel down a potential gradient until depositing on the target surface of a negatively biased cathode [33]. The stainless steel conical mold insert served as cathode in the present study. Choice of anode depended on the choice of plating metal. Nickel exhibits only minor internal stress upon deposition, which improves bond strength with the substrate. Moreover, it can be deposited at relatively high rates [17]. Thus, nickel comprised the sacrificial anode.

Nickel-plating may be performed in various solutions. First published in 1916, the Watt's bath achieved considerable popularity due to the increased plating speed it facilitated at relatively high temperatures and current densities [64]. Variants of this solution have demonstrated further improvement. At Louisiana State University, a modified Watt's bath allowed even higher current densities and faster deposition, which limited the possible swelling and delamination that photoresist may experience during extended submersion. Moreover, this solution fostered finer-grain deposition, which improved hardness of plated nickel—an attractive aspect when considering molding [18]. The following Table 4-6 details the composition of the aforementioned solutions as well as the nickel-sulfamate bath used in the current work.

Table 4-6 Nickel Plating Solutions Prepared in De-ionized Water[18,64,65].

Watt's Bath		Modified Watt's Bath		Nickel-Sulfamate Bath	
Compound	*Concentration (g/L)*	*Compound*	*Concentration (g/L)*	*Compound*	*Concentration (g/L)*
Nickel Sulfate, $NiSO_4 \bullet 7H_2O$	240	Nickel Sulfate, $NiSO_4 \bullet 6H_2O$	300	Nickel Fluoborate, $Ni(SO_3HN_3)_2 \bullet 4H_2O$	340-450
Nickel Chloride, $NiCl_2 \bullet 6H_2O$	20	Nickel Chloride, $NiCl_2 \bullet 6H_2O$	45	Nickel Chloride, $NiCl_2 \bullet 6H_2O$	0-20
Boric Acid, H_3BO_3	20	Boric Acid, H_3BO_3	45	Boric Acid, H_3BO_3	30-40
		Sodium Lauryl Sulfate	0.3-0.5		
		Saccharin	0.5-1.0		
		Coumarin	0.5		

Effectiveness of the nickel-sulfamate bath depended on appropriate temperature, pH, and electrode arrangement. The plastic tub containing the plating solution was placed in a thermostat-controlled heated water bath. Using a digital sensing element, solution temperature was maintained at approximately 50°C. Addition of amidosulfonic acid increased hydrogen content (lowering pH), and addition of nickel carbonate reduced hydrogen content (raising pH). Measuring with a digital sensing element and adjusting as necessary, a pH level of 4 was attained to optimize plating efficiency [33,65]. To distribute metal ions for uniform plating coverage, the conical mold insert was surrounded by a cylindrical mesh basket of nickel pellets. The axisymmetric orientation of this sacrificial anode ensured a consistent nickel deposition rate on the cathode—the substrate surface [5].

To prepare the conical mold insert for electroplating, preliminary measures were taken. First, a soldered wire offered a path for current flow. A threaded plastic shaft was attached to facilitate submersion in the nickel-sulfamate bath. The electrically neutral shaft ensured negligible interaction with metal ions. To prevent unintended plating, areas of the mold insert were covered by a layer of liquid electrical tape. As depicted in Figure 4-25, this layer confined metal deposition to the conical surface of interest. To avoid possible passivation of the stainless steel substrate, the work piece was submerged in a proprietary solution for approximately 1 minute (C-12 Activator by Puma Chemical). Applying constant potential (2V) between the mold insert and a stainless steel counter electrode, this step effectively eliminated a strong oxide layer [5]. Lastly, a thin starter layer of nickel was applied using a Wood strike solution. Upon submersion, a constant current (0.5A) was delivered between the mold insert and a surrounding nickel shroud for 2½ minutes. This initial layer of metal increased the bond strength of subsequent plating [5].

Figure 4-25. Preparations of the conical mold insert prior to electroplating.

Electroplating a desired thickness depended on several considerations. Foremost, the surface area (*A*) receiving nickel needed to be calculated. Referencing the triangular dimensions printed on the mask image, area of a single feature was found using basic geometry. By determining feature population, total area could be computed by simple multiplication. With this figure and the following equation, an appropriate current (*I*) could be selected to generate the desired current density (*J*) of 10mA/cm^2.

$$I = J \cdot A \tag{9}$$

Illustrated in the formula below, the duration of electroplating (Δt) depended on the aforementioned current density and the desired plating thickness (h) [66]. An interpretation of Faraday's Law, this equation includes a unique coefficient derived from the molecular weight of nickel-sulfamate, density of nickel, transferred electrons, and Faraday's constant [33].

$$\Delta t = \frac{h}{1220 \cdot J} \tag{10}$$

After the allotted time, the conical mold insert was extracted from the plating bath. Following a thorough rinse in de-ionized water, the liquid electrical tape was peeled away, the soldered wire detached, and the plastic shaft unscrewed. The photoresist template was degraded using an appropriate remover solution. Heat and mechanical agitation improved this dissolution process. After additional rinsing with de-ionized water and drying with pressurized air, the mold insert underwent final documentation. Images were captured through optical microscopy and snapshots were acquired with the Zygo® system.

CHAPTER 5 – RESULTS AND DISCUSSION

5.1 Overview

Performing and refining the procedure required a considerable investment. The mock mold inserts necessitated a ready supply of stainless steel, an assortment of machinery, and the experience of trained machinists. High-precision printing services preempted photomask development. Lithography methods depended on a variety of chemicals and laboratory instrumentation. Spanning multiple days, the duration of the overall process demanded substantial focus and patience.

The principles of Design of Experiments (DOE) and Analysis of Variance (ANOVA) proved to be critical tools in managing limited resources and achieving meaningful results. An initial fractional factorial experiment revealed sources of process variation while minimizing the number of runs [67]. This screening step identified the relative significance of four process variables, the influence of interactions, and the contribution of experimental error. A full factorial experiment followed. With emphasis placed on two factors, this experiment further substantiated a data trend observed during the initial screening. This trend revealed an important process parameter to consider when incorporating XP Microspray™ products into photolithography.

An unforeseen complication diverted experimental efforts. Due to a shortage in Microspray™ availability, an alternative photoresist product was introduced into the process. This introduction prompted an additional full factorial experiment, which exactly mimicked the previous full factorial study. Although marketed as a comparable aerosol form of photoresist, the unique characteristics of this alternative Microchem® product became thoroughly evident during experimentation. Despite the diversion, this additional study complimented overall efforts to further refine the photolithography process and to progress the limits of micro-texturing applications.

5.2 Defining a Measurable Outcome

Past studies have demonstrated the robustness of nickel deposition techniques [13,34]. Thus, successfully building micro-textures on the conical mold insert relied primarily on the formation of a quality template. The geometric accuracy of electroplated features directly reflected the accuracy of the exposed and developed photoresist layer. Achieving appropriate micro-asperity heights depended on administering photoresist with sufficient thickness. With this recognition, refinements to the lithographic process were accomplished by focusing analysis on photoresist quality after UV-exposure and development.

Analysis was facilitated by two instrumental tools. With magnifications ranging from 50X to 1000X, an optical microscope provided key qualitative observations, which could be digitally recorded using a supplemental camera and software. As previously described, the Zygo® system offered an added dimension to visual inspection. Moreover, the data acquisition enabled quantitative measurements through both the integrated MetroPro™ software and within the MATLAB® environment. The capabilities of these instruments are illustrated in Figure 5-1.

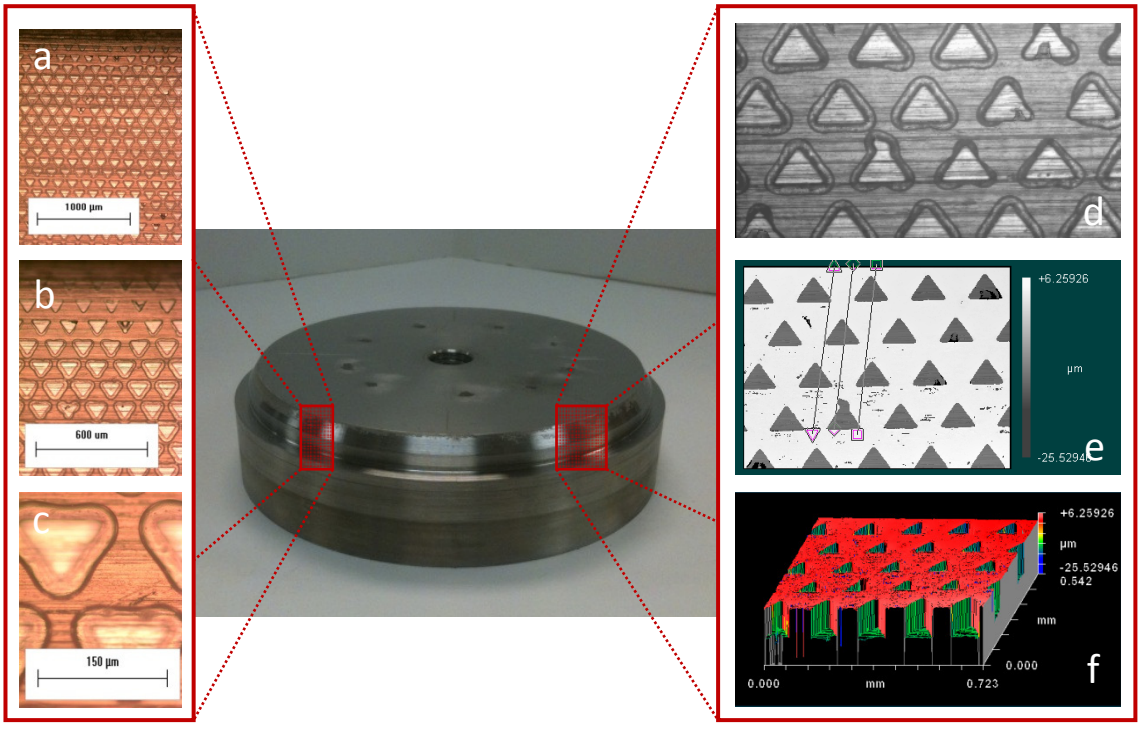

Figure 5-1. To assess photoresist quality, optical microscopy could be applied at 50x (a), 100x (b), and 500x (c) magnifications. Inspection with the Zygo® system provided intensity maps (d), surface plots (e), and oblique plots (f).

To improve utility and efficiency, measurement efforts were localized to a specific region of the mold insert critical to elastomer function. During operation, a radial lip seal interacts with the shaft in locations near the apex of the elastomer. After proper installation, this apex deflects and flattens against the shaft creating a sealing zone as shown in Figure 5-2 [50]. Hydrodynamic behavior within this zone has been augmented with shaft micro-textures [13]. A future aim is to facilitate elastomeric micro-textures in this sealing zone.

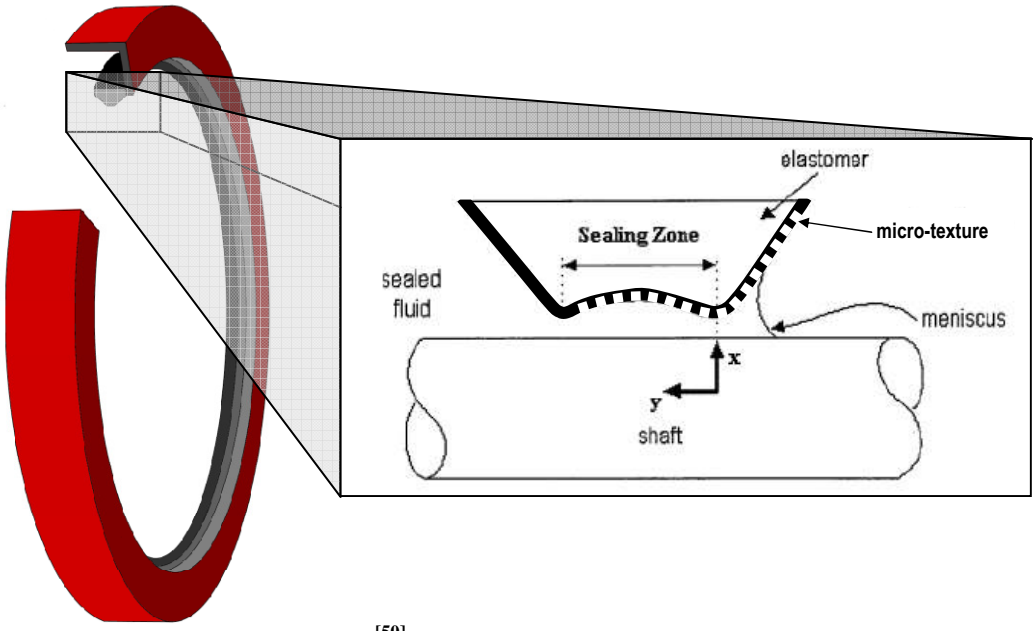

Figure 5-2[50]. Analysis methods aimed to facilitate elastomeric micro-textures in the sealing zone.

To realize this aim, micro-texturing on the mold insert needed to be guaranteed in a particular region. During injection molding, microasperities within this region will transfer the desired pattern to the expected sealing zone of the elastomer. Per conversations with industry representatives, this region was known to fall 0.076" below the top of the conical section [68]. This location is clarified in Figure 5-3. Recalling angle specifications for the mold insert, basic trigonometry was applied to translate this value to a distance measured parallel to the surface of interest (0.0906"). Thus, although the intent was to cover the entire conical surface of the mold insert, successful micro-texturing of this region would ensure pattern transfer to the elastomeric sealing zone. Analysis efforts focused on this area.

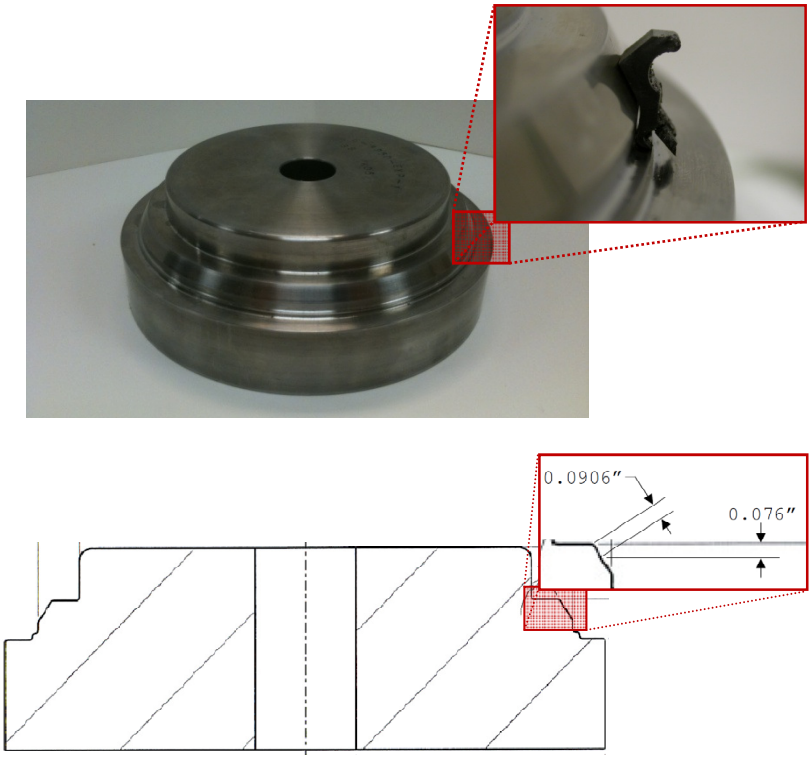

Figure 5-3. To ensure micro-textures in the sealing zone of the elastomer, a corresponding region was identified on the mold insert (above). Analysis efforts focused on this location (below).

Quantifying photoresist quality became a challenging task. Past studies have considered various aspects including pattern distortion, sidewall angle, pinhole density, and surface adhesion [6,8,14,57,63]. Among the possibilities for measurement, the experimental outcome needed to satisfy several key considerations. It needed to be extractable from data acquired with the Zygo® system. If it relied on assumptions, these needed to be reasonable and defendable. Moreover, the outcome needed to appropriately reflect the scope and objective of the project.

To satisfy these concerns, a parameter was constructed that emphasized the surface coverage achieved following photoresist development. Termed as coverage ratio (CR), this measurement indicated the amount of substrate surface area that successfully received photoresist. By comparing this to an ideal case, the degree of success could be encapsulated by a basic percent error calculation. The concept of CR is expressed in the equation below:

$$Coverage\ Ratio\ (CR) = \frac{Resist\ Coated\ Area}{Total\ Area} \tag{11}$$

Calculating CR depended on the criteria used to distinguish resist-coated areas from vacant areas. With regards to the Zygo® data acquisition, this implied determining which data points corresponded to photoresist and which data points corresponded to the bare stainless steel substrate. Inevitably, a numerical approach ensued. Specifically, an algorithm was developed that inspected each unique data point and its associated height (Z-dimension). The effectiveness of this algorithm inherently relied on three conditions: (i) defining an appropriate baseline; (ii) defining a reasonable threshold; and (iii) implementing comparisons in an efficient manner. This methodology is illustrated in the following Figure 5-4.

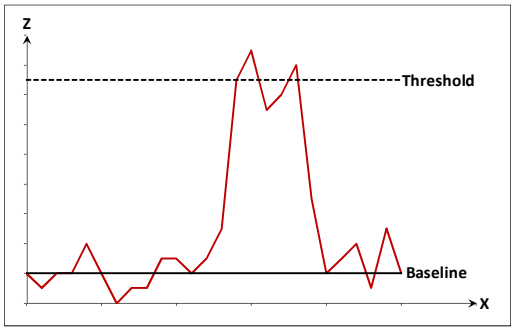

Figure 5-4. Two-dimensional illustration of algorithm to calculate CR.

Determining the baseline proved exceptionally difficult. Ideally, after the Zygo® system acquired measurements, the distribution of Z-heights revealed a certain minimum, and this value reflected a potential base reading. However, suspect data greatly skewed this ideal situation. As depicted in Figure 5-5, a few data points often exhibited a noticeable difference as compared to the remaining sample population. These readings impacted the range of data and disguised the appropriate baseline value.

Outlier removal represents a substantial branch of statistics beyond the scope of the present study. However, fairly trivial techniques may be applied when filtering suspect data from normal distributions. In the Grubbs method, the acceptance or rejection of data depends on its variation from the mean value relative to the standard deviation [69]. An even more basic technique uses box plots. Using such plots, suspect values may be confirmed by noting their positions relative to the lower and upper quartiles. These simple approaches quickly lose relevance when facing non-Gaussian distributions. Due to thickness imparted by photoresist, the current work encountered obvious bimodal distributions, which hampered efforts to identify suspect data.

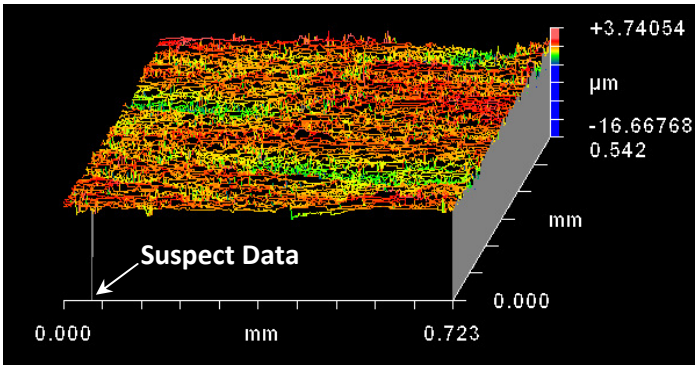

Figure 5-5. Suspect data acquired by Zygo® system.

To accommodate the unique distributions, a histogram-based method was developed. This technique concentrated on removing suspect data located near the extremes, which consequently improved accuracy of the minimum value and baseline determination. As the terminology suggests, the over 300,000 data points collected during each Zygo® measurement were categorized into bins to visualize the frequency distribution. The identification of erroneous data began by inspecting bin sizes near the lower limits of the population. Bins below a prescribed size were removed, which eliminated the data points therein. Progressing towards the distribution mean, eventually bins exceeded the prescribed size and subsequent data was preserved. An analogous progression was administered to upper limits of the population. Using three-dimensional plots to gauge effectiveness, the number of bins and prescribed bin size were adjusted until satisfactory removal of suspect data. Divided into 2000 bins, the finalized algorithm removed bins containing fewer than 15 data points, which represented less than 0.005% of the entire data. The following Figure 5-6 depicts an exemplary distribution before and after implementing this histogram-based method. The impact of this filtering scheme is reflected in Figure 5-7.

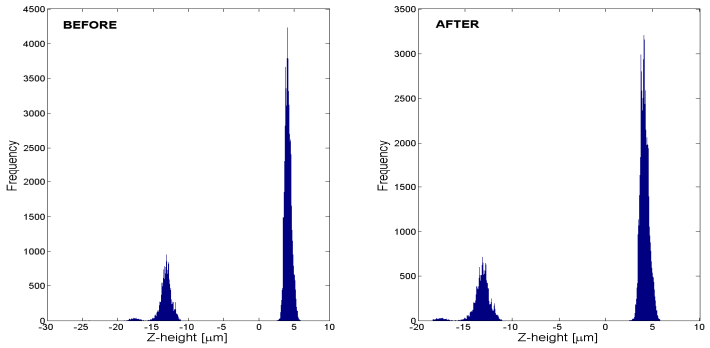

Figure 5-6. Distribution of Z-heights acquired during a single Zygo® measurement before (left) and after (right) filtering suspect data.

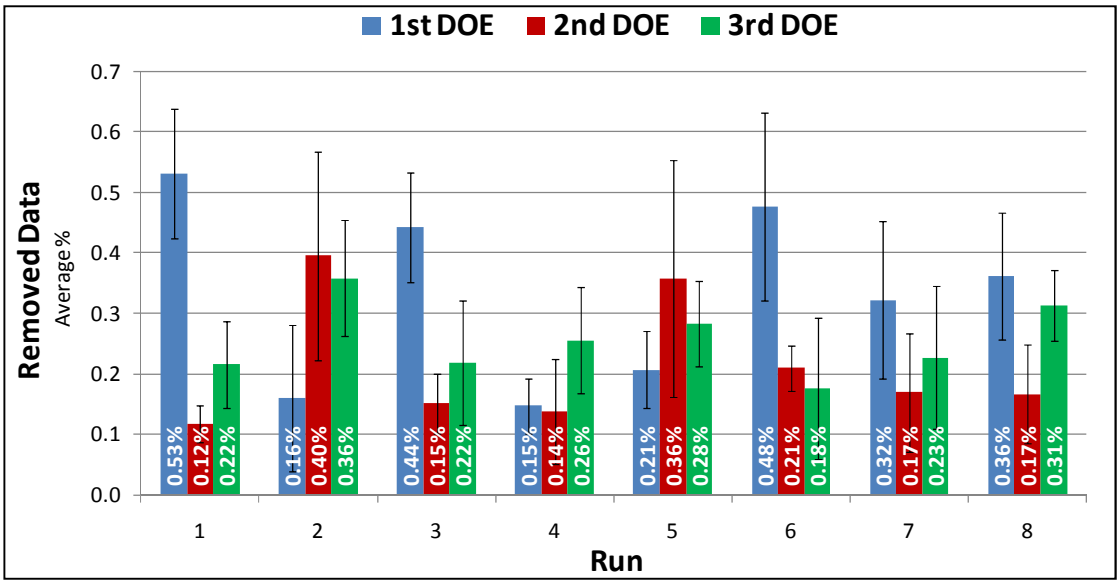

Figure 5-7. Average percentage of data filtered during each experimental run.

With an established baseline, determining an appropriate threshold became the next priority. This task incorporated two components: (1) average surface roughness (R_a) of the substrate and (2) photoresist thickness. The prior element accounted for normal height variations inherent to the stainless steel mold insert after machining, and this value was previously measured. The latter element proved more critical due to its relative magnitude and its variability. This variability directly correlated to the number of resist coats administered in each unique experimental run, and quantifying this correlation proved crucial.

To achieve this correlation, data acquired by the Zygo® system was exploited. Namely, each experimental run involved a specified number of photoresist layers. Noting this discrete value and measuring the resulting resist thickness, a collection of 100 data points provided a foundation for a linear correlation. Figure 5-8 and Figure 5-9 illustrate the measurement approach and the determined correlation, respectively.

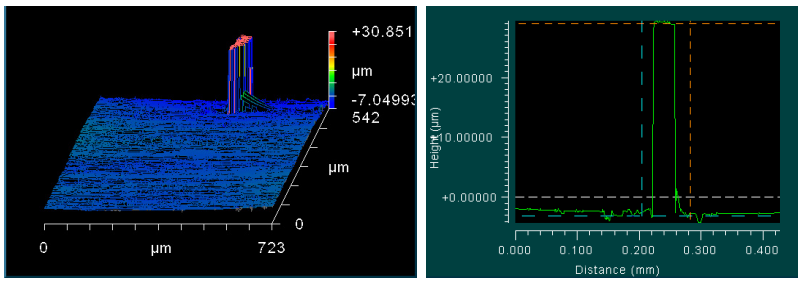

Figure 5-8. Zygo® measurements (left) revealed photoresist thickness (right).

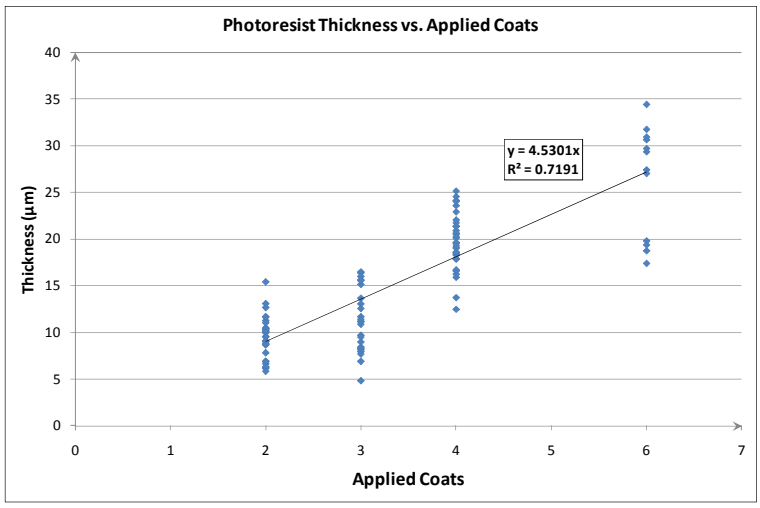

Figure 5-9. Correlation between photoresist thickness and applied coats using Microchem® XP Negative Microspray™.

A final algorithm encompassed the aforementioned baseline and threshold. Data exported from the Zygo® system was analyzed within a MATLAB® environment to ultimately calculate the desired coverage ratio (Appendix F). First, the histogram-based filter removed suspect data from the extremes of the data distribution, and a newly refined minimum represented the base reading. Next, the threshold comprised the substrate's average surface roughness and the photoresist thickness as predicted by the linear model. With the efficiency of computation, each data point could then be categorized based on its associated Z-height. A final accounting step summarized the results into a single numerical value. The following Figure 5-10 depicts an orthogonal plot of filtered data, the threshold plane, and the calculated CR.

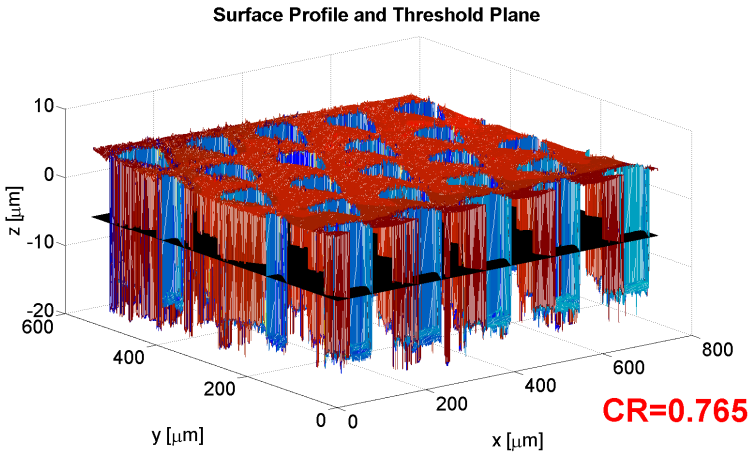

Figure 5-10. Algorithm implemented in MATLAB® to compute coverage ratio (CR) for a Zygo® measurement.

Ideally, the lithography process transfers the photomask pattern directly to the resist-coated substrate yielding a specific value of CR. Determining this ideal CR became crucial to the application of ANOVA techniques. Two methods provided insight. By extracting dimensions from the mask design, a CR value could be calculated by simple geometry. Table 5-1 displays the results of this geometric approach. Of note, the population of triangles included several partial entities, which were managed with CAD software to calculate appropriate areas.

Table 5-1 Geometric Approach to Determine Ideal CR.

	Population	Area (μm^2)	Total Area (μm^2)	Area Ratio (Triangles:Overall Mask)	Coverage Ratio (CR)
Full Triangles	155980	4173.0	$6.5090 \cdot 10^8$	0.2371	**0.7629**
Partial Triangles #1	27	2086.5	$5.6336 \cdot 10^4$		
Partial Triangles #2	28	1462.5	$4.0950 \cdot 10^4$		
Overall Mask	--	--	$2.7456 \cdot 10^9$		

Alternatively, the photomask was directly analyzed with the Zygo® system to compute an ideal CR measurement. Ink invariably introduced a minute thickness. This thickness was easily detectable using light interferometry, and measurements were exported to MATLAB® for analysis. Applying a trivial algorithm, the printed regions of the plastic film were distinguished from the surrounding areas, and an ideal value of CR was obtained (Appendix G). As Figure 5-11 shows, the results appeared visually accurate.

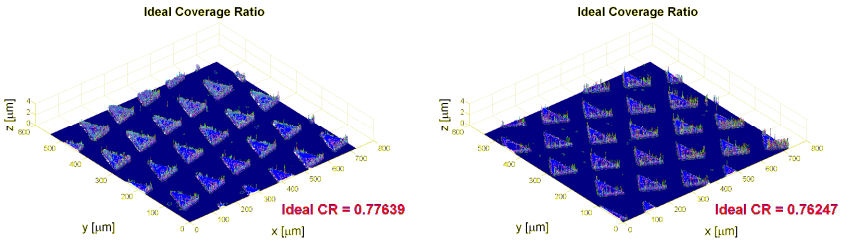

Figure 5-11. Ideal CR based on Zygo® measurements.

Displayed below, Table 5-2 summarizes the values obtained using both techniques. Compared to the geometric approach, the Zygo® inspection method provided a decidedly truer reflection of the ideal scenario.

Table 5-2 Results for Ideal CR.

Method	Ideal Coverage Ratio (CR)
Geometric	0.7629
Zygo®/MATLAB®	0.7694†

†Averaged value

By comparing experimental CR to ideal CR, photoresist quality could then be quantified. As shown in the equation below, a basic percent error calculation facilitated this comparison. Thus, larger values suggested poor quality whereas smaller values implied a desirable outcome. An accepted pitfall of this technique concerned pattern definition; that is, attaining ideal CR could have occurred coincidentally without achieving the desired pattern. Of course, qualitative observations through optical microscopy and light interferometry allowed identification of such coincidences, but these subjective assessments offered limited value. However, this pitfall was minimized by averaging 8 separate measurements for each experimental run. Furthermore, the associated standard deviations helped elucidate measurement reliability.

$$\%Error = \frac{\left|CR_{experimental} - CR_{ideal}\right|}{CR_{ideal}} \cdot 100\% \tag{12}$$

5.3 First Design of Experiments

The initial DOE served as a screening step. Although conclusive results were unlikely, a variety of process variables could be investigated using minimal resources. Specifically, four factors were studied in a 2^{4-1} fractional factorial experiment, which allocated two levels per factor by definition. The study comprised a total of eight unique treatments, and each treatment was performed on a dedicated conical mold insert (Sample #1 – #8). Manufactured by Microchem® Corporation, a product marketed as XP Negative Microspray™ served as the negative-acting photoresist, which employed a novel aerosol form. Every mold insert underwent the full 3-day lithographic process with documentation facilitated by optical microscopy and the Zygo® system.

The primary drawback of any fractional experiment rests on the creation of aliases and confounding. However, this risk can be managed. As main effects and lower order interactions likely drive the process, higher order interactions become prime candidates for intentional confounding [67]. In the present study, the highest order interaction served as the identity, which reduced experimental runs at the expense of disguising effects cause by this fourth-order interaction. This design promoted meaningful results by confounding main effects with the presumably negligible third-order interactions. In contrast, this fractional-factorial design supplied poor feedback on secondary interactions as these inevitably confounded with other second-order interactions. Of course, suspicions of these effects could easily be expounded with ensuing experimental designs.

Final considerations for the initial DOE concerned blocking and randomization. Due to time constraints encountered during mask procurement, a blocking scheme separated the full study into two subsets of four experimental runs. This implementation facilitated timely completion of the screening process, but it also increased risk. As the blocked experiments occurred on separate days, the delay allowed unforeseen factors to potentially impact results. For example, a convection oven may have inexplicably varied a few degrees, or an experimenter may have slightly shifted work habits from one day to the next. However, this potential risk was offset by introducing randomization. The present study utilized random permutations created by MATLAB® to arrange experimental runs in a non-distinct order. Table 5-3 displays the finalized design for the initial fractional-factorial experiment.

Table 5-3 Fractional-Factorial Design of 1st DOE.

Treatment	Run†	(A) Layers of Photoresist		(B) Exposure Dosage		(C) Pre-Bake Times		(D) Mask Cutting	
		(-) 3 Coats	*(+) 6 Coats*	*(-) 1x Recommended (400mJ/cm²)*	*(+) 2x Recommended (800mJ/cm²)*	*(-) None*	*(+) As Is*	*(-) By Hand*	*(+) Die-Cut*
1	*3*	-		-		-		-	
2	*7*	+		-		-		+	
3	*8*	-		+		-		+	
4	*1*	+		+		-		-	
5	*5*	-		-		+		+	
6	*2*	+		-		+		-	
7	*4*	-		+		+		-	
8	*6*	+		+		+		+	

†Run order randomized using the "randperm" function in MATLAB®.

Confounding and Aliases

A=BCD	B=ACD	C=ABD
D=ABC	AB=CD	AC=BD
	AD=BC	

	For the first block of testing, the "Mask Cutting" factor is set at the "(-) By Hand" level.
	For the second block of testing, the "Mask Cutting" factor is set at the "(+) Die-Cut" level.

Factor selection bore from two motives: (i) the need to investigate process variables unique to the present work and (ii) the desire to substantiate findings from previous literature. Past research has supported the feasibility of building photoresist thickness through layering [6,10]. The current study attempted to develop this technique further and gauge its potential with respect to a complex substrate. Exposure dosage has proven to be a critical element to lithography-based methods [8,59,60,61]. Understanding this parameter became especially important when considering the relatively novel Microspray™ photoresists. The prebake step has been recognized as a means to remove solvents from deposited resists [6]. However, based on surveyed literature, the significance of this heat treatment remained questionable. Lastly, a conical masking element represents a relatively novel approach to micro-texturing non-planar surfaces. Its usefulness would benefit by identifying specifications crucial to its function.

For each experimental treatment, 8 separate measurements were captured by the Zygo® system and processed in MATLAB® (Appendix H). Measurement locations were spaced equally around the perimeter of the conical surface and were focused on the regions relevant to the elastomeric sealing zone. Thus, the experimental outcome comprised a total of 64 separate calculations of percent error in CR. To interpret these results, ANOVA techniques were performed to identify factors contributing significant process variation (Appendix I). This variance was gauged using Fisher's *F* Statistic [67]. The following Table 5-4 summarizes the results of this analysis.

Table 5-4 ANOVA Results for 1st DOE.

Source of Variation	SS	df	MS	F	F'	% Contribution
A (Layers of Photoresist)	9567.1409	1	9567.141	18.65244	2.8	10.56%
B (Exposure Dosage)	10495.851	1	10495.85	20.46309	2.8	11.59%
C (Pre-Bake Times)	5490.9193	1	5490.919	10.70529	2.8	6.06%
D (Mask Cutting)	1013.6734	1	1013.673	1.976294	2.8	1.12%
AB	31463.926	1	31463.93	61.34319	2.8	34.75%
AC	1699.0276	1	1699.028	3.312485	2.8	1.88%
AD	2102.8427	1	2102.843	4.099777	2.8	2.32%
Error	28723.316	56	512.9164			31.72%
Total	90556.697	63				

Results from the initial screening experiment highlighted significant sources of process variation. Photoresist layering and exposure dosage introduced comparable contributions (10.56% and 11.59%, respectively). The secondary interaction of these two factors appeared to impact photoresist coverage the greatest (34.75%). However, this latter observation suffered from two shortcomings. Experimental error proved a prominent detractor (31.72%). Though neglected third-order interactions may have slightly inflated the computed contribution, the noticeable presence of error suggested several process variables were not recognized. Furthermore, the nature of the fractional-factorial design limited reliable conclusions. As mentioned previously, two-factor interactions were inevitably confounded by other two-factor interactions. Thus, the interactive effect of photoresist layering and exposure dosage may have been skewed by the interaction of pre-baking and mask cutting. Regardless, this screening exercise provided direction for an ensuing full factorial experiment.

5.4 Second Design of Experiments

Results from the initial screening were honed during a subsequent full factorial experiment. Several features of the initial study persisted into the second experimental design. The XP Negative Microspray™ remained a core element in the process. Photoresist layering and exposure dosage continued to be interesting factors as alluded by their considerable contribution to variation during the 1st DOE. Their inclusion was further supported due to a perceived significant interaction. As before, the secondary study comprised a total of 8 unique treatments, which were executed in a randomized fashion dictated by MATLAB® permutations.

Despite similarities, the 2nd DOE exhibited key differences. The elimination of two factors represented the most obvious change. Due to relatively minor contributions, the prebaking and mask cutting variables were not considered. This decision helped further conserve limited resources, and it facilitated a more extensive investigation of the remaining factors. With regard to the remaining variables, these also experienced modification. Slightly different photoresist layering schemes reduced material usage. However, these schemes diversified practical experience with the Microspray™ product while continuing themes of the initial study. Regarding exposure dosage, the number of levels doubled. This expansion reflected a desire to more fully understand underexposure, overexposure, and the behavior between these extremes. Considerable changes also affected the overall lithographic process. Foremost, nickel deposition was neglected. As parameters for this relatively robust step relied heavily on the recipient surface

area, photoresist coverage became a more prominent focus. Elimination of electroplating facilitated another change. Each treatment no longer required a unique conical mold insert. Without permanent nickel features, a pristine substrate surface could be realized by chemically removing developed photoresist. Invariably, this decision implied that no physical specimen would be preserved after each treatment; documentation served as the primary means to analyze process outcome. However, by submitting a single mock mold (Sample #9) to repeated treatments, the consistent surface characteristics helped improve experimental confidence.

The finalized 2nd DOE offered several additional advantages. Characteristic of full-factorial experiments, aliases were eliminated, which likewise removed concerns about confounding. With adequate resources procured and an abbreviated lithographic process, blocking no longer became necessary. Table 5-5 depicts the final structure of the second experimental design.

Table 5-5 Full-Factorial Design of 2nd DOE.

		(A) Layers of Photoresist		(B) Exposure Dosage (mJ/cm^2)			
		2 Coats	*4 Coats*	*300*	*600*	*900*	*1200*
Treatment	**Run†**						
1	*6*	✓		✓			
2	*3*		✓	✓			
3	*7*	✓			✓		
4	*8*		✓		✓		
5	*5*	✓				✓	
6	*1*		✓			✓	
7	*2*	✓					✓
8	*4*		✓				✓

†Run order randomized using the "randperm" function in MATLAB®.

Documentation of each treatment consisted of 8 separate measurements acquired by the Zygo® system and processed in MATLAB® (Appendix J). As before, snapshots were spaced equally along the conical surface with emphasis placed on regions relevant to the elastomeric sealing zone. In total, 64 separate calculations of percent error in CR were computed. Results were interpreted using ANOVA to quantify contributions to process variation (Appendix K). Fisher's *F* Statistic facilitated this analysis of variance, and the following Table 5-6 summarizes the results.

Table 5-6 ANOVA Results for 2nd DOE.

Source of Variation	SS	df	MS	F	F'	% Contribution
A (Layers of Photoresist)	71.592752	1	71.59275	0.329631	2.8	0.15%
B (Exposure Dosage)	7484.0084	3	2494.669	11.48608	2.14	15.38%
AB	28935.277	3	9645.092	44.4084	2.14	59.47%
Error	12162.679	56	217.1907			25.00%
Total	48653.558	63				

The outcome closely mimicked trends observed after the initial screening. Exposure dosage continued to impart significant variation (15.38%). Furthermore, the interaction of exposure dosage and photoresist layering impacted results considerably (59.47%)—an effect noted during the previous study. However, a noticeable gap developed between process variables. That is, differing layers of photoresist provided only minor influence on photoresist coverage. Based on the critical Fisher statistic (*F'*), this factor proved to be an insignificant contributor (0.15%). Of course, conclusive evidence was combated by error. Though reduced substantially (from 31.72% to 25.00%), the contribution of error remained an indicator of uncontrolled experimental factors. Despite this pitfall, the full factorial study eliminated confounding effects, and it localized attention to an important factor. Exposure dosage played a conspicuous role. Recommendations from the photoresist manufacturer provided a reference point, but with regards to an unconventional substrate, these dosage specifications proved to be insufficient [16].

5.5 Third Design of Experiments

Progress was hampered by an exceptional obstacle. According to Microchem® representatives, the XP Negative Microspray™ was discontinued due to concerns about raw material availability. This photoresist product represented a major component of the developing UV-lithographic process. Its exclusion from progressive work posed serious ramifications. However, its continued inclusion also presented considerable risks. Although a short supply remained, this stock pile was inadequate for extensive use. Moreover, any scientific discoveries would be superfluous without the primary ingredient at a user's disposal.

In response, alternative photoresists were considered. Among products marketed by Microchem®, two potential replacements were readily available: (i) XP Positive Microspray™ and (ii) XP SU8 Microspray™. Supplied in aerosol form, both products permitted spray application. However, distinct characteristics existed. As the name suggests, XP Positive Microspray™ exhibits fundamentally different chemical behavior. Upon irradiation, the photoresist experiences excisions on a molecular level, which facilitate preferential removal of exposed regions. In contrast, the behavior of XP SU8 Microspray™ resembles the negative-acting photoresist originally incorporated in the present work. This chemical reactivity is achieved through a different formulation though, which introduces a degree of unpredictably. Given the perceived options, the SU8-based photoresist seemed more viable and less disruptive to the envisioned process.

Thus, a third experimental design ensued with two objectives. First, demonstrate the feasibility of this alternative product in an effort to promote continued research. Secondly, provide a comparative study to highlight key aspects of XP Negative Microspray™ and XP SU8 Microspray™. To realize these objectives, a full factorial experiment was designed with a structure identical to the previous. A majority of the lithographic procedure remained intact with a few exceptions. To accommodate the different molecular structure, an appropriate developing solution was prepared per manufacturer's recommendation. Moreover, a more aggressive remover solution was applied to overcome the strong adhesiveness typical to SU8 formulations [20]. This removal step allowed a single conical mold insert to be processed repeatedly (Sample #10).

As in previous experiments, 8 treatments were performed in a randomized manner. For each treatment, 8 separate measurements were captured with the Zygo® system (Appendix L). Percent error in CR was calculated for each measurement, and ANOVA techniques were applied to analyze variance (Appendix M). The overall experimental design and results are displayed in Table 5-7 and Table 5-8, respectively.

Table 5-7 Full-Factorial Design of 3rd DOE.

		(A) Layers of Photoresist		(B) Exposure Dosage (mJ/cm^2)			
		2 Coats	*4 Coats*	*300*	*600*	*900*	*1200*
Treatment	**Run†**						
1	*8*	✓		✓			
2	*3*		✓	✓			
3	*6*	✓			✓		
4	*7*		✓		✓		
5	*5*	✓				✓	
6	*1*		✓			✓	
7	*2*	✓					✓
8	*4*		✓				✓

†Run Order randomized using the "randperm" function in MATLAB®.

Table 5-8. ANOVA Results for 3rd DOE.

Source of Variation	SS	df	MS	F	F'	% Contribution
A (Layers of Photoresist)	6.3378063	1	6.337806	0.00455	2.8	0.00%
B (Exposure Dosage)	16352.353	3	5450.784	3.913264	2.14	11.58%
AB	46881.522	3	15627.17	11.21917	2.14	33.19%
Error	78002.381	56	1392.9			55.23%
Total	141242.59	63				

Results from this final study appeared to corroborate findings from the previous 2nd DOE. Layering of photoresist provided negligible impact (0.00%), and exposure dosage persisted as a significant factor (11.58%). As before, a second-order reaction appeared a substantial source of variation (33.19%). However, the contribution of experimental error was profound as evidenced by the over two-fold increase (25.00% to 55.23%). This finding suggested a significant source of variability remained unknown.

Several probable sources were identified. The XP SU8 Microspray™ exhibited drastically different optical properties compared to the XP Negative Microspray™. Namely, the SU8 formulation was noticeably more transparent. This characteristic may have negatively impacted the accuracy of light interferometry readings. In addition, development of the SU8-based photoresist revealed another issue. After prolonged submersion in developer solution, unexposed regions of photoresist persisted. Regardless of the cause, this underdevelopment hindered recognition of the stainless steel substrate during documentation. Consequently, algorithms executed in MATLAB® may have misidentified minimums in the surface. Inflated baseline assumptions were the major concern. Moreover, inaccurate minimums obstructed efforts to model thickness of the XP SU8 Microspray™. Unpredictable thickness translated to unreliable threshold values as computed by the MATLAB® routine. Ultimately, the linear model determined for the 2nd DOE was adopted, which implied the Microspray™ products shared similar correlations. This assumption was not ideal, and threshold accuracy suffered. This scenario is apparent in Figure 5-12, which depicts an image captured by optical microscopy and the associated analysis.

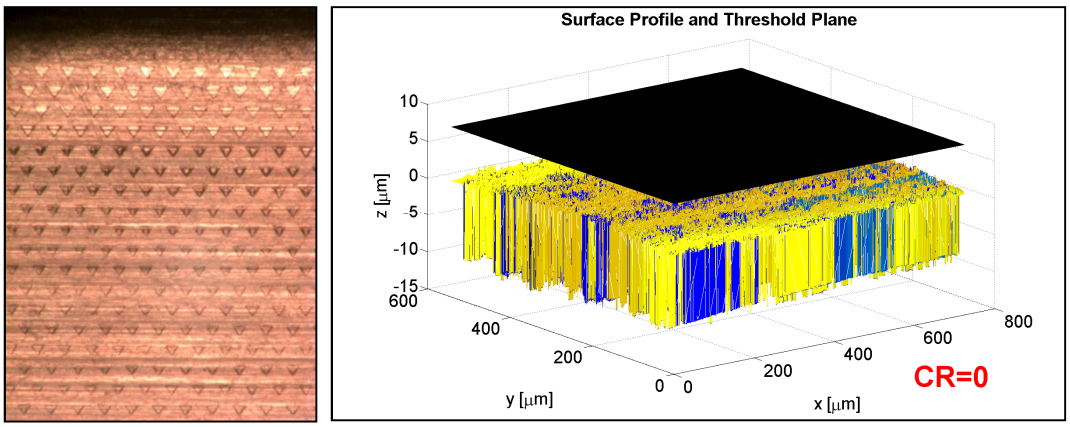

Figure 5-12. Underdevelopment of XP SU8 Microspray™ (left) complicated threshold determination during the MATLAB® analysis (right).

5.6 Discussion

Realization of a textured conical mold insert proved elusive. Despite complications, the experimental designs offered insight into a feasible UV-lithographic patterning process. The following discussion highlights several aspects to consider in future research efforts.

5.6.1 Challenges to Micro-texturing

Successive application of DOE techniques revealed several challenges to achieving the micro-textured conical mold insert. Delamination considerably impeded progress. Evidence of an adhesion loss between the photoresist and substrate emerged during the initial screening study. However, conclusive proof was hampered by the limitations of optical microscopy and light interferometry. As depicted in Figure 5-13, magnified images depicted a peculiar phenomenon affecting the fringes of developed micro-features.

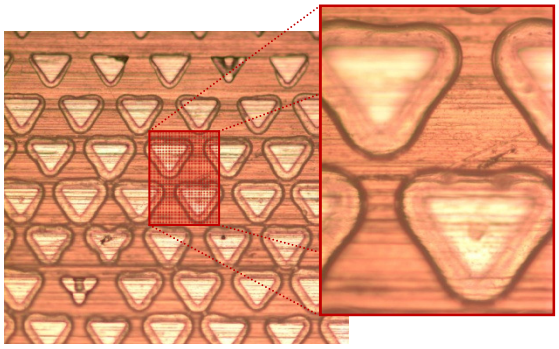

Figure 5-13. Phenomenon observed at fringes of micro-features during the initial screening study.

Early notions focused on the possibility of a degrading photoresist surface. Namely, the fringes might have resulted from an overly aggressive developer solution, which partially dissolved the perimeter of micro-cavities. The edges may have suffered an undesirable rounding effect, which would conceivably produce fringes. However, two observations discounted this theory. First, measurements acquired by the Zygo® did not indicate a curvature forming at the upper boundaries of micro-features. Secondly, results from electroplating shifted attention from the upper surface to the basal interface between photoresist and stainless steel. These observations are illustrated in Figure 5-14.

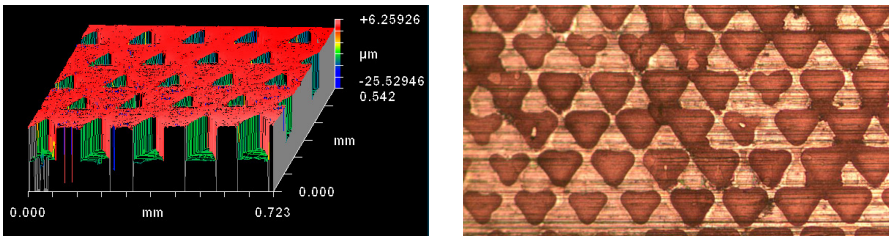

Figure 5-14. Zygo® measurements contradicted a degradation effect at the surface (left). Electroplating results shifted attention to the photoresist-substrate interface (right).

Optical microscopy offered evidence of adhesion loss. If photoresist detached from the substrate, then the resulting gap allowed nickel to deposit beneath, which exacerbated the problem. Indeed, documentation of photoresist coverage provided significant evidence of delamination as show in Figure 5-15. This issue has pervaded several previous studies [1,18,19,61]. Although mechanical clamping has been identified as one possible solution, the complex conical geometry complicates implementation. Furthermore, XP Negative Microspray™ exhibited a noticeable brittleness after development as determined by a simple scratch test. This charactersistic would prove problematic if excessive pressures were created by a clamping technique.

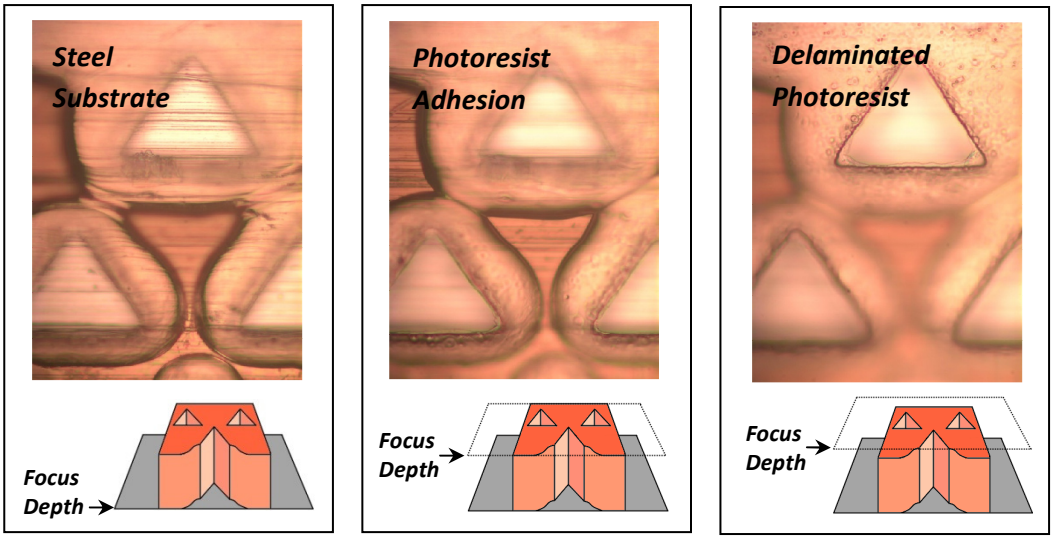

Figure 5-15. By observing the substrate-photoresist interface (left), regions of successful adhesion (center) are distinguished from regions of delamination (right).

On the contrary, the XP SU8 Microspray™ presented unique obstacles at the opposite spectrum. As past research has shown, this photoresist formulation exhibits high adhesive strength [20]. This characteristic contributed to relatively long development times in the current work. Durations on the order of hours were common—a stark contrast compared to the minutes required when developing the XP Negative Microspray™.

Despite longer durations, developer solutions inadequately dissolved unexposed regions of SU8 photoresist. As mentioned earlier, this issue complicated analysis efforts. Several possible explanations emerge. Diffraction of ultraviolet light might have unintentionally exposed areas of masked photoresist. Glycerin offers a means to combat this effect by eliminating air gaps between the mask and substrate [5,62]. However, constraining this liquid on a non-planar surface proved a difficult task in the present experimental setup. Alternatively, underdevelopment might have resulted from overexposure. SU8 gained popularity due to its increased sensitivity to light exposure [10]. This characteristic might have amplified the undesirable effects of diffraction. Lastly, the relative transparency of XP SU8 Microspray™ could have facilitated reflection [14,70]. Instead of being absorbed or diffused, radiation might have reflected from the stainless steel surface causing a drastically increased exposure dosage.

5.6.2 Coverage Ratio and Contributing Factors

Achieving ideal coverage ratio (CR) required identifying significant process variables. Several possible factors were evaluated by DOE and ANOVA methods. Based on the initial screening study, photoresist layering and exposure dosage contributed considerable variation to the process. A noticeable second-order interaction supplemented suspicions. To further elucidate, a 2nd DOE focused on these variables, and correlations were computed with respect to the defined process outcome—percent error in CR. The following Figure 5-16 illustrates the findings.

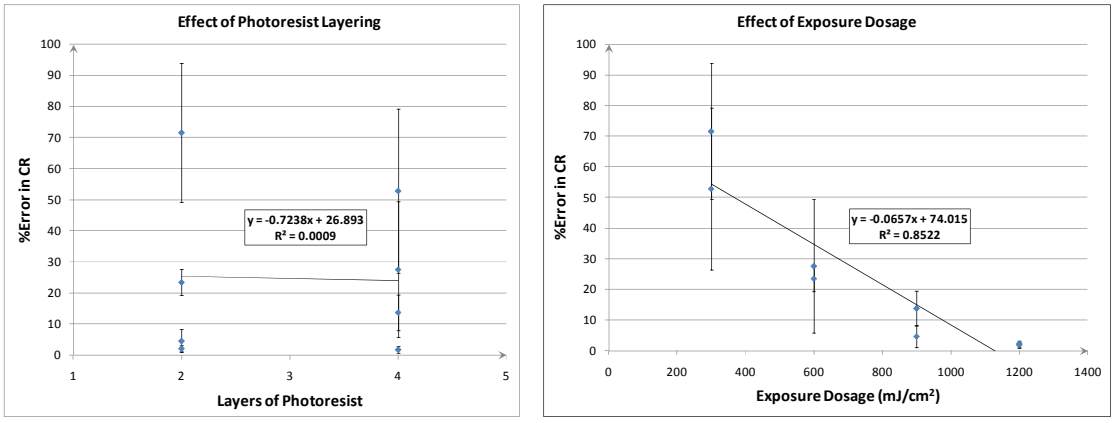

Figure 5-16. Based on the 2nd DOE, the photoresist layering (left) exhibited a negligible correlation whereas the exposure dosage (right) exhibited a relatively strong correlation.

The computed correlations were not surprising. With regards to layers of photoresist, the poor correlation ($R^2 = 0.0009$) reflected its low contribution to variation (0.15%) during the 2nd DOE. Considering the impact of exposure dosage, the strong correlation ($R^2 = 0.8522$) supported legitimacy of the ANOVA analysis (15.38%). From a qualitative perspective, optical microscopy further evidenced this correlation as depicted in Figure 5-17. Thus, results indicated exposure dosage was a significant parameter when applying XP Negative Microspray™ in a UV-lithographic process. Moreover, the manufacturer's recommendation (400mJ/cm^2) proved an underestimate when processing the conical mold insert.

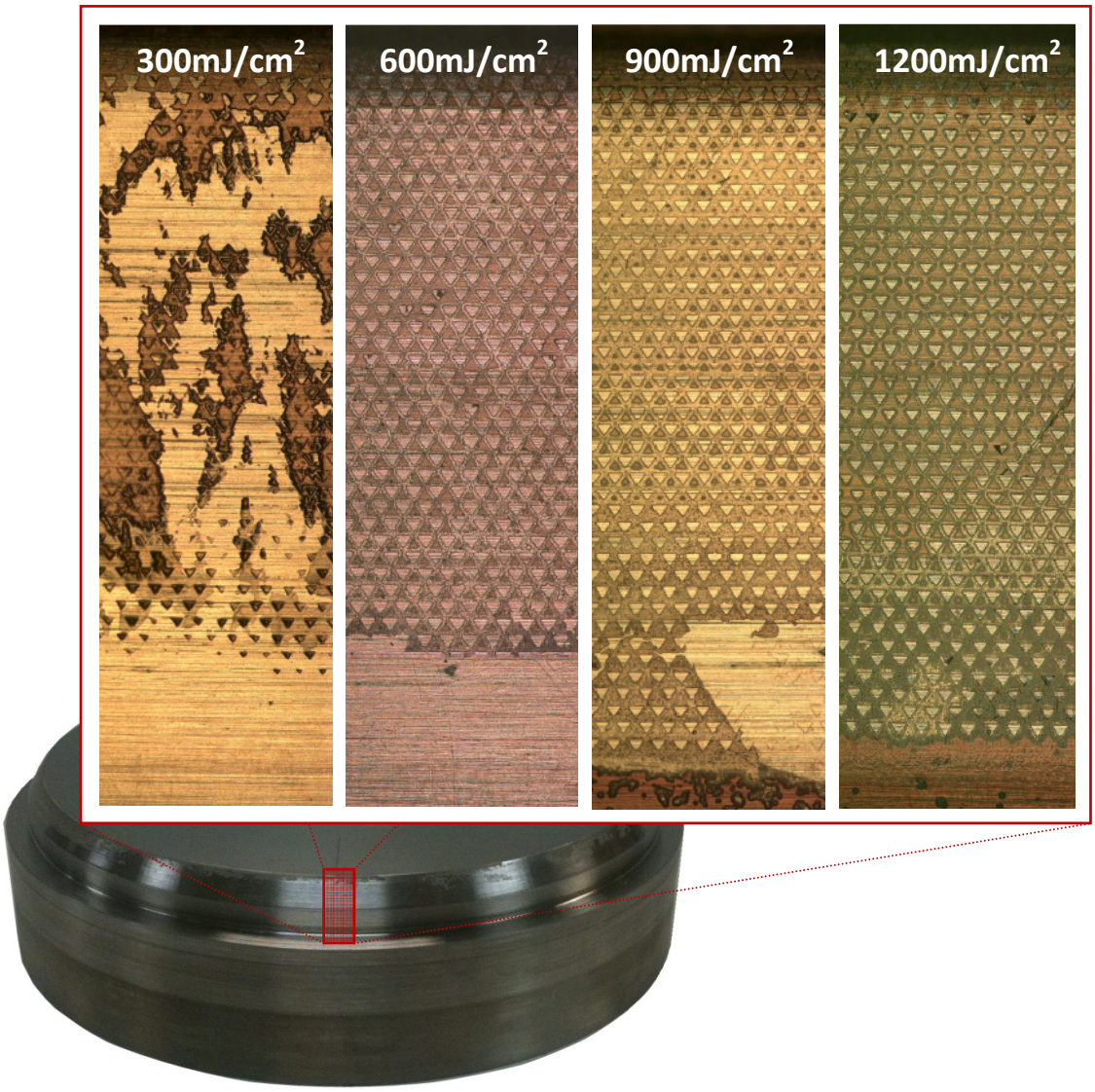

Figure 5-17. For treatments receiving 4 layers of photoresist, images captured during the 2nd DOE suggested a trend with respect to exposure dosage.

However, with respect to exposure dosage, the aforementioned correlation suffers a degree of uncertainty. Namely, an aspect of the conical mold geometry was overlooked. Due to the angled surface, the mold radius was not a constant value (r_o) as assumed in Equation 6. As illustrated in Figure 5-18, the radius varied slightly with respect to the exposed surface. Applying basic trigonometry, this variation in radius (r) can be expressed by the equation below.

$$r(y) = r_o + y\cos 57° \tag{13}$$

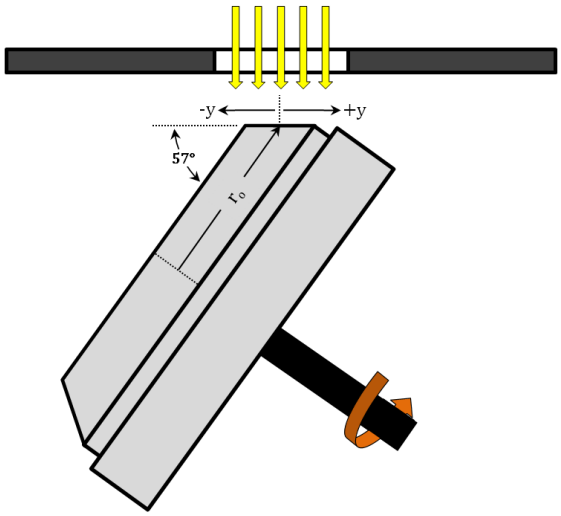

Figure 5-18. With regards to the exposed surface, the dosage deviated slightly from the intended value due to variations in the mold radius caused by the chamfer angle.

Recalling the exposure durations (Δt), light intensity (I), and exposure slit width (x), the following equation provides a more accurate model of exposure dosage. As displayed in Table 5-9, the deviations in dosage relative to the intended value were minor (< 4%).

$$E(y) = \frac{I \cdot \Delta t}{\pi} \cdot \sin^{-1}\left(\frac{x/2}{r_o + y\cos 57°}\right) \tag{14}$$

Table 5-9. Deviations in Exposure Dosage

Radius (inches)	Exposure Dosage (mJ/cm^2) at various exposure times (Δt)					
	Δt = 2253.7 sec (Intended Dosage of 300mJ/cm^2)	Δt = 3005 sec Intended Dosage of 400mJ/cm^2	Δt = 4507.4 sec (Intended Dosage of 600mJ/cm^2)	Δt = 6009.9 sec Intended Dosage of 800mJ/cm^3	Δt = 6761.2 sec (Intended Dosage of 900mJ/cm^2)	Δt = 9014.9 sec Intended Dosage of 1200mJ/cm^4
2.665	309.6	412.9	619.3	825.7	928.9	1239
2.708	304.8	406.4	609.6	812.7	914.3	1219
2.750 *	300.1	400.1	600.1	800.2	900.2	1200
2.775	297.4	396.5	594.8	793.0	892.2	1190
2.800	294.8	393.0	589.5	786.0	884.3	1179

*Assumed radius, r_o

Besides the selected factors, another variable might have influenced results. The post-exposure bake (PEB) supplied heat to drive the cross-linking reaction in SU8 photoresist to completion. However, this heat might have induced an undesirable effect. As previously mentioned, mismatches in thermal expansion coefficient can conceivably create stresses at the photoresist-substrate interface. Delamination might ensue [14,59,61]. After the final experimental design, a brief investigation was performed. Four successive treatments were applied to a conical mold insert, and they shared the following characteristics: (i) 4 layers of XP Negative Microspray™ and (ii) an exposure dosage of 1200mJ/cm^2. The primary exception was a unique PEB temperature profile. Figure 5-19 illustrates these profiles and presents qualitative results. Photoresist quality appeared optimal after applying the normal baseline profile. The remaining PEB temperature profiles offered few perceived advantages. Furthermore, a lower maximum temperature was designed to reduce the effects of thermal stress; however, more pronounced delamination was observed in these cases, which rendered the theory unrealistic.

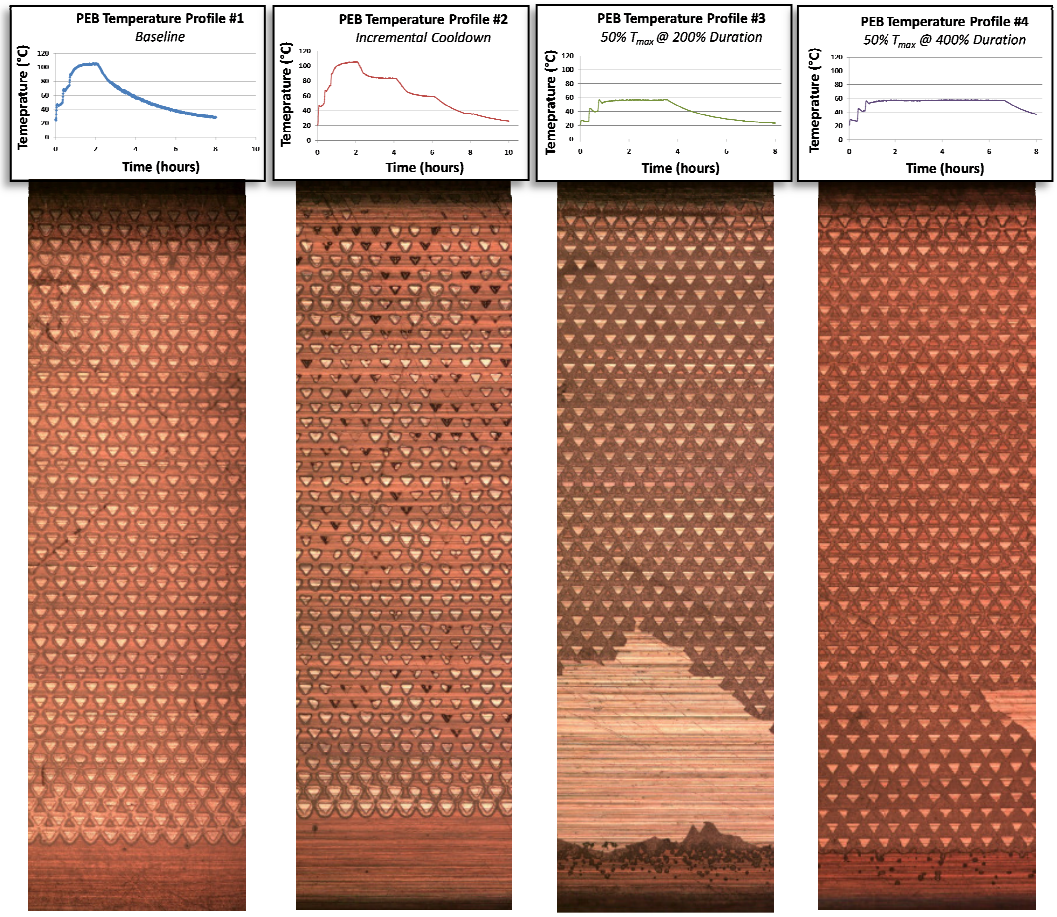

Figure 5-19. Alternative PEB temperature profiles applied to investigate possible thermally induced delamination of photoresist.

5.6.3 Challenges to Analysis

Interpreting the process outcome depended on the analytic methods. Several challenges hampered application of these methods. For instance, the underdevelopment of SU8 photoresist diminished accuracy of the MATLAB® algorithm. Inappropriate baselines and unpredictable photoresist thickness contributed to unreliable threshold values. As a result, confidence in the computed coverage ratio (CR) values was diminished. This issue was a plausible source of variation due to experimental error in the 3rd DOE (55.23%)

Surface defects introduced a similar obstacle to analysis. Namely, several defects presented extreme heights or depths relative to the average surface roughness. The MATLAB® routines potentially suffered due to these defects. However, as these anomalies typically occurred at a small frequency, the histogram-based filtering method offered a formidable defense. Illustrated in Figure 5-20, a Zygo® measurement shows a noticeable surface indentation.

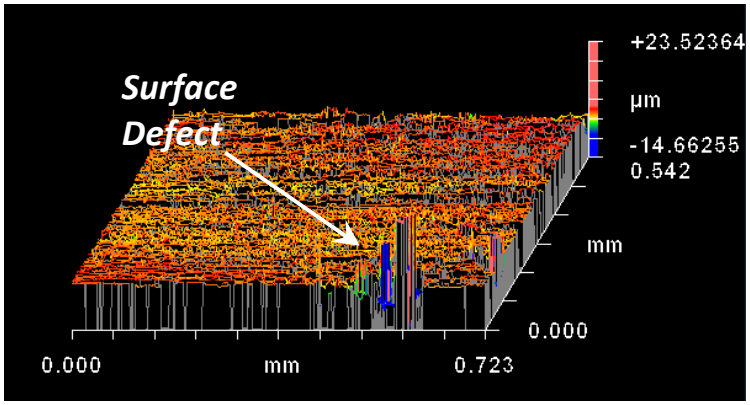

Figure 5-20. Visible defect in the substrate surface.

Lastly, incomplete Zygo® measurements persisted throughout the course of the study. Initially recognized during inspection of the conical mold inserts, this issue created gaps in the acquired data matrix. Specifically, values of surface height were nonexistent. Presumably, these gaps resulted from miscues during measurement digitization. Regardless, this missing data represented a potential source of experimental error. The frequency of this issue is reflected in the following Figure 5-21. Except for a single case, all 192 Zygo® measurements exhibited a minor data loss (less than 0.05%). The exception involved drastically higher casualties (with over 40% data loss). Due to multiple measurements, its impact on analysis was reduced, but this unique instance implores caution in future efforts.

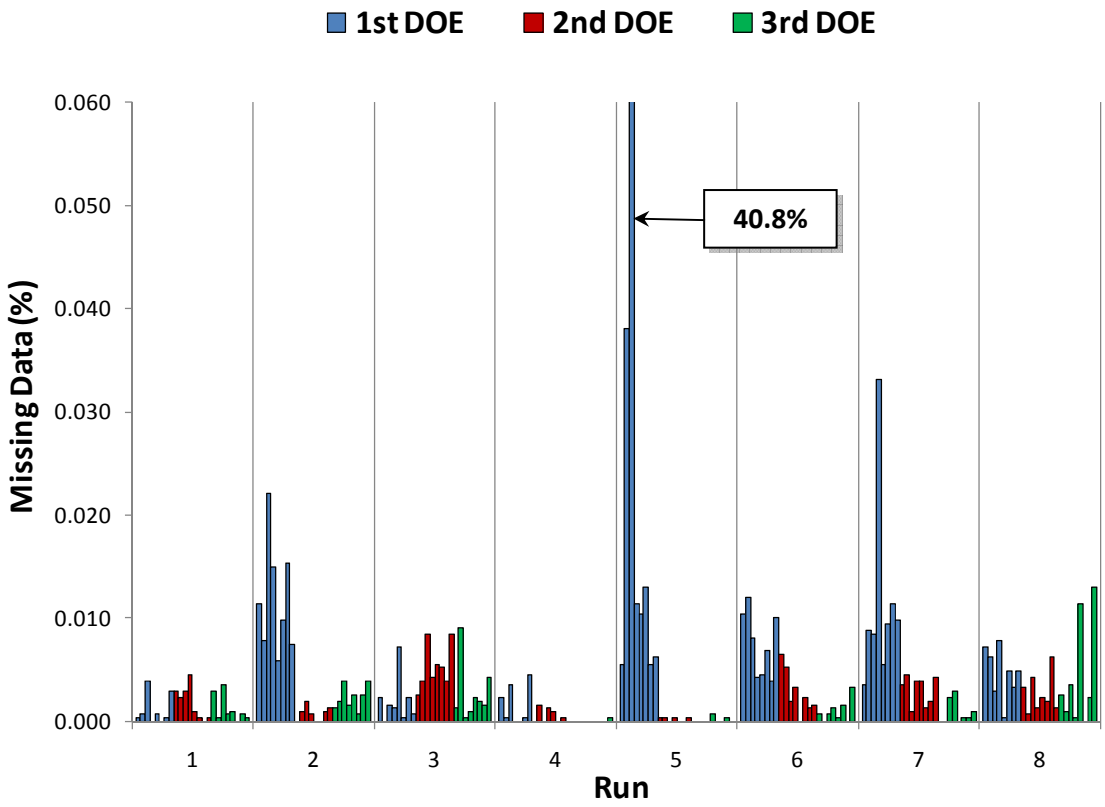

Figure 5-21. Data loss sustained during Zygo® measurements.

CHAPTER 6 – CONCLUSIONS

6.1 Conclusions

Extending the limits of UV-lithography will help introduce micro-texturing technology into new environments. Supported by the resources and facilities of the Bearings and Seals Laboratory at the University of Kentucky, the present study advanced efforts to manufacture fields of micro-features on a complex non-planar surface. Based on this research, the following conclusions have developed:

- The conical mold insert is a feasible candidate for surface engineering via a UV-lithographic process. It represents a threshold to new applications of lithography based methods.
- The commercially available Microchem® XP Microspray™ products offer an alternative means to apply photosensitive coatings to non-planar substrates.
- Exposure dosage is a significant factor to consider when using XP Negative Microspray™ to facilitate UV-lithographic patterning on an unconventional substrate.
- XP SU8 Microspray™ serves as a plausible solution to the delamination and availability issues associated with XP Negative Microspray™.
- By achieving an appropriate 2-dimensional design, a 3-dimensional masking element can be developed to conform to the non-planar surface of a conical mold insert.
- A clamp plate provides a simple means to secure and align a photomask to a complex substrate. Moreover, this technique minimizes unnecessary machining by exploiting pre-existing features of the substrate.
- Coverage Ratio (CR) is a capable measurement to consider when identifying significant process variables by Design of Experiments (DOE) and Analysis of Variance (ANOVA).

6.2 Future Considerations

The potential of a UV-lithographic patterning process continues to be unveiled. The present work revealed areas for further improvement. Foremost, certain measures might enhance the performance of XP SU8 Microspray™. Past studies suggest that reflectivity can be reduced by applying an appropriate base layer to the substrate surface [70,71]. Eliminating this issue will be crucial to refining exposure dosage. In addition, light diffraction could be minimized by developing methods to administer glycerine. Evidence supports this notion [5,62]. The

compensatory effect of glycerine may also relax the precision requirements during mask design and application. With regards to the photomask, design modifications could enhance the usefulness of experimental results. Namely, numerical studies have benefited greatly due the incorporation of a unit cell [39]. Realizing this concept in the conical mask design would enable critical comparisons between theoretical and experimental findings. Lastly, adjustments to masking and exposure steps might permit the manufacture of a tapered conical mold insert [33]. The inclusion of draft angles to micro-features could reduce ejection forces needed during molding, which could improve efficiency.

The limits of UV-lithography may be surpassed by investigating alternative methods for micro-texturing. Delamination issues might be circumvented by integrating the clamping techniques of previous studies [1,5,18]. These methods depended on development of a free standing polymethyl methacrylate (PMMA) pattern, which was secured mechanically to the substrate. With respect to the present work, techniques to create a three-dimensional photomask could be adapted to manufacture the appropriate PMMA template. Diffraction also proved problematic to UV-lithography. Gaps between mask and substrate amplified this diffraction, and these gaps indicated non-uniformities in the resist-coated surface. However, these gaps might be eliminated by introducing an intermediate machining step. In past research, an over-application of photoresist allowed a subsequent removal of excess material and a simultaneous planing effect [20]. A similar approach might enhance photomask contact with the conical mold insert.

Some limitations of a complex substrate may be unavoidable. For instance, post processing may be severely hampered. When manufacturing micro-features by electroplating, a polishing step removes characteristic surface variations due to metal deposition [17]. This step is trivial when considering planar substrates [34]. The task becomes impractical with respect to a conical mold insert. However, this limitation is not isolated to lithography techniques. Laser-based methods also rely on post-processing to remove undesirable bulge formations [11]. Thus, despite some limitations, UV-lithography remains a competitive approach to micro-texturing a conical mold insert.

APPENDIX A – MACHINIST DRAWING FOR MOCK MOLD INSERT

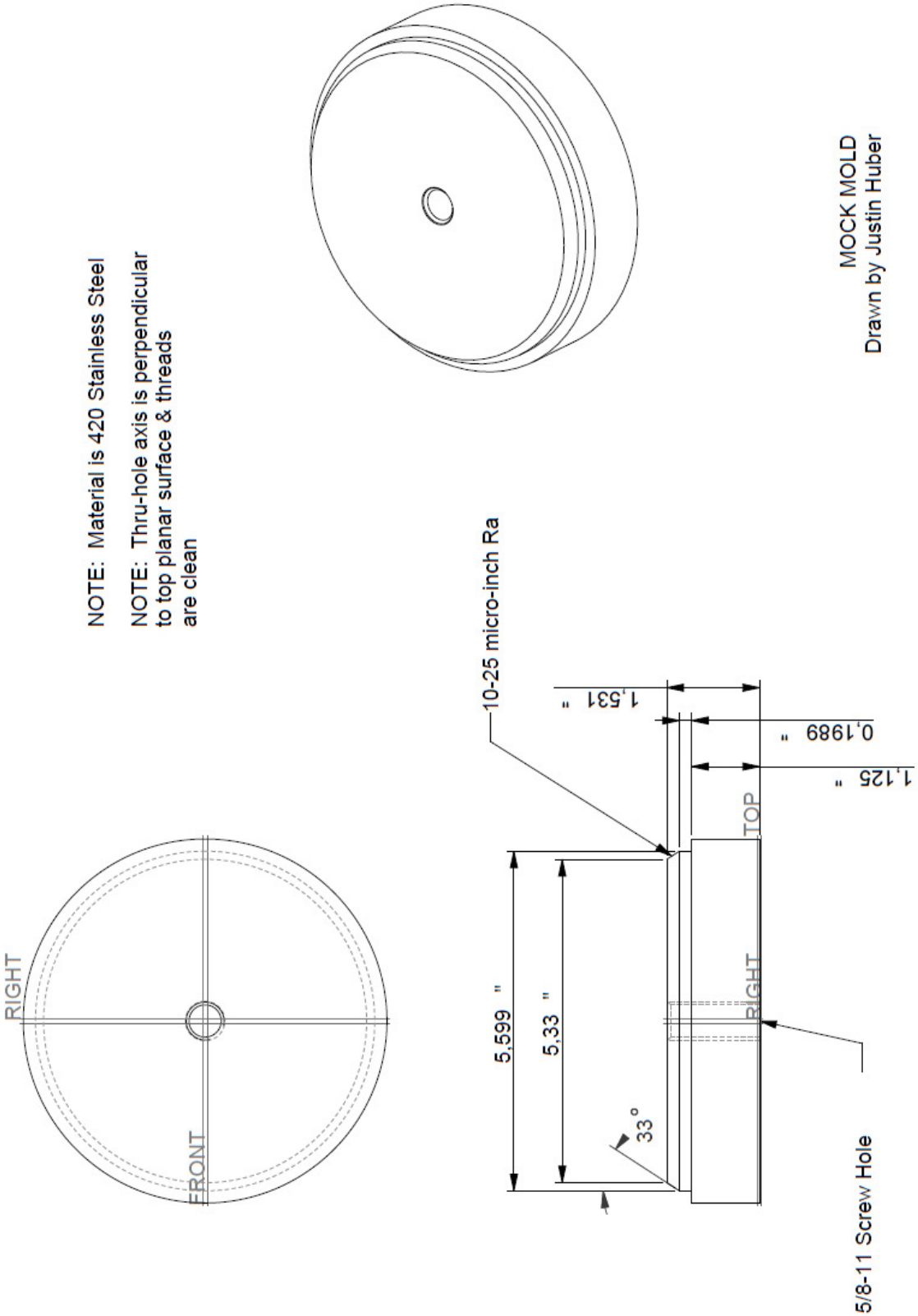

APPENDIX B – MATLAB® CODE TO FIND AVERAGE SURFACE ROUGHNESS

```
%Average Surface Roughness (Ra)

%The following code computes the surface roughness for a surface.  In
%particular, 8 separate values of Ra are determined for each of the 8
%separate measurements acquired per mold insert.

%Written by Justin Huber

clear all
directory=input('Please input the directory & mold number: ','s');
Ra=zeros(1,8);
count=zeros(1,8);

for N=1:8

    filename=[directory,'_m',int2str(N),'_xcylinder.xyz'];
    [X,Y,Z,x,y,z]=read_zygo_data(filename);
                                %Import the Zygo measurement data

    count(N)=0;     %Records the number of missing data points
    for I=1:640
        for J=1:480
            if isnan(Z(I,J))     %The 'isnan' function distinguishes
                count=count+1;   %between a number and a NaN
            end                  %(not-a-number)
        end
    end
    xi_count=0;     %xi_count records the number of data points
    xi_sum=0;       %xi_sum is a summation of z-heights
    for I=1:640
        for J=1:480
            if ~isnan(Z(I,J))
                xi_sum=xi_sum+Z(I,J);
                xi_count=xi_count+1;
            end
        end
    end
    xi_bar=xi_sum/xi_count;      %xi_bar is the mean plane
    eta_count=0;    %eta_count records number of data points
    eta_sum=0;      %eta_sum is summation of variations
    for I=1:640     %about mean plane
        for J=1:480
            if ~isnan(Z(I,J))
                eta_sum=eta_sum+abs(xi_bar-Z(I,J));
                eta_count=eta_count+1;
            end
        end
    end
    Ra(N)=eta_sum/eta_count;     %Calculation of average surface
end                              %roughness

Ra
count
```

APPENDIX C – PHOTOMASK BULK GEOMETRY

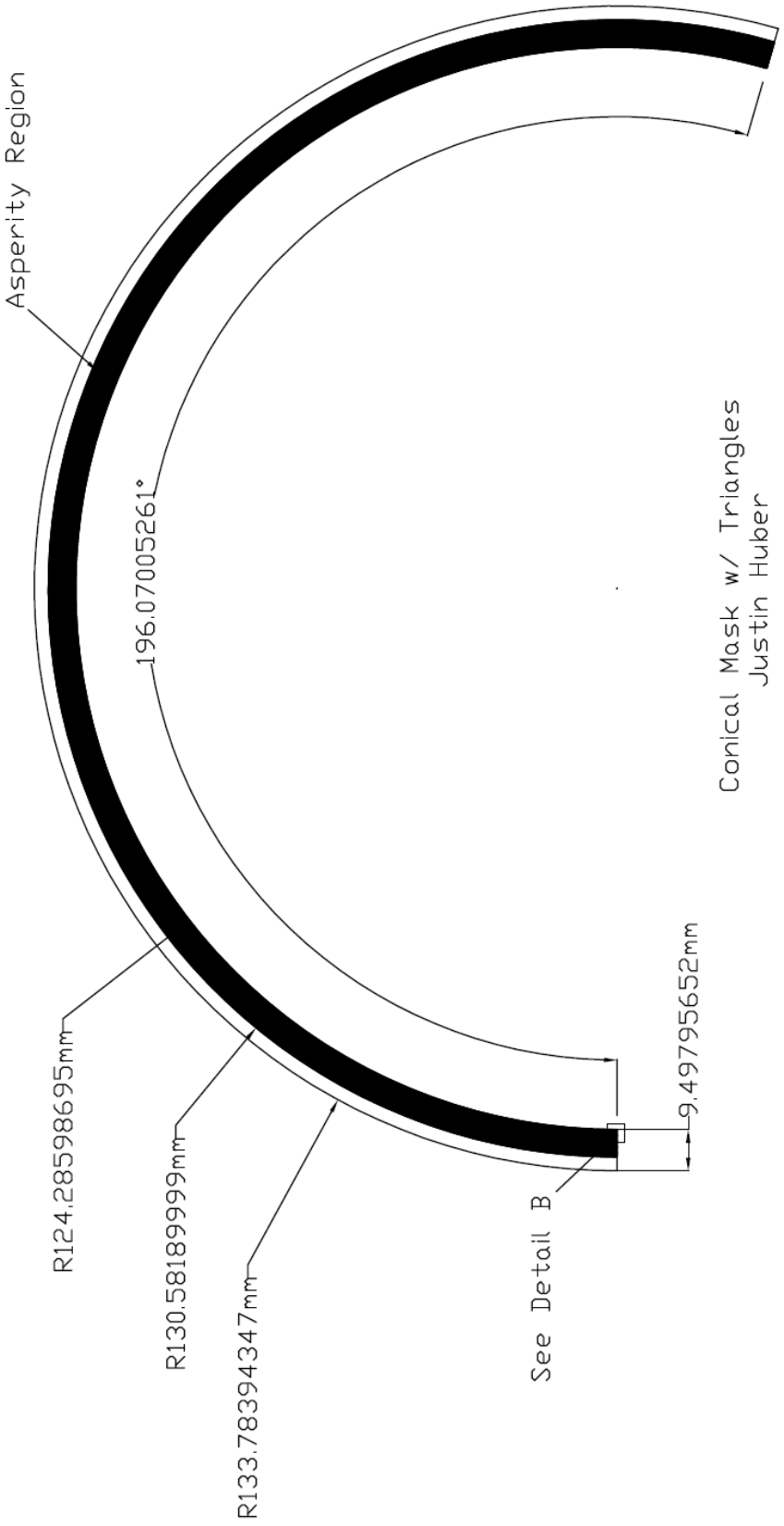

APPENDIX D – PHOTOMASK DETAIL GEOMETRY

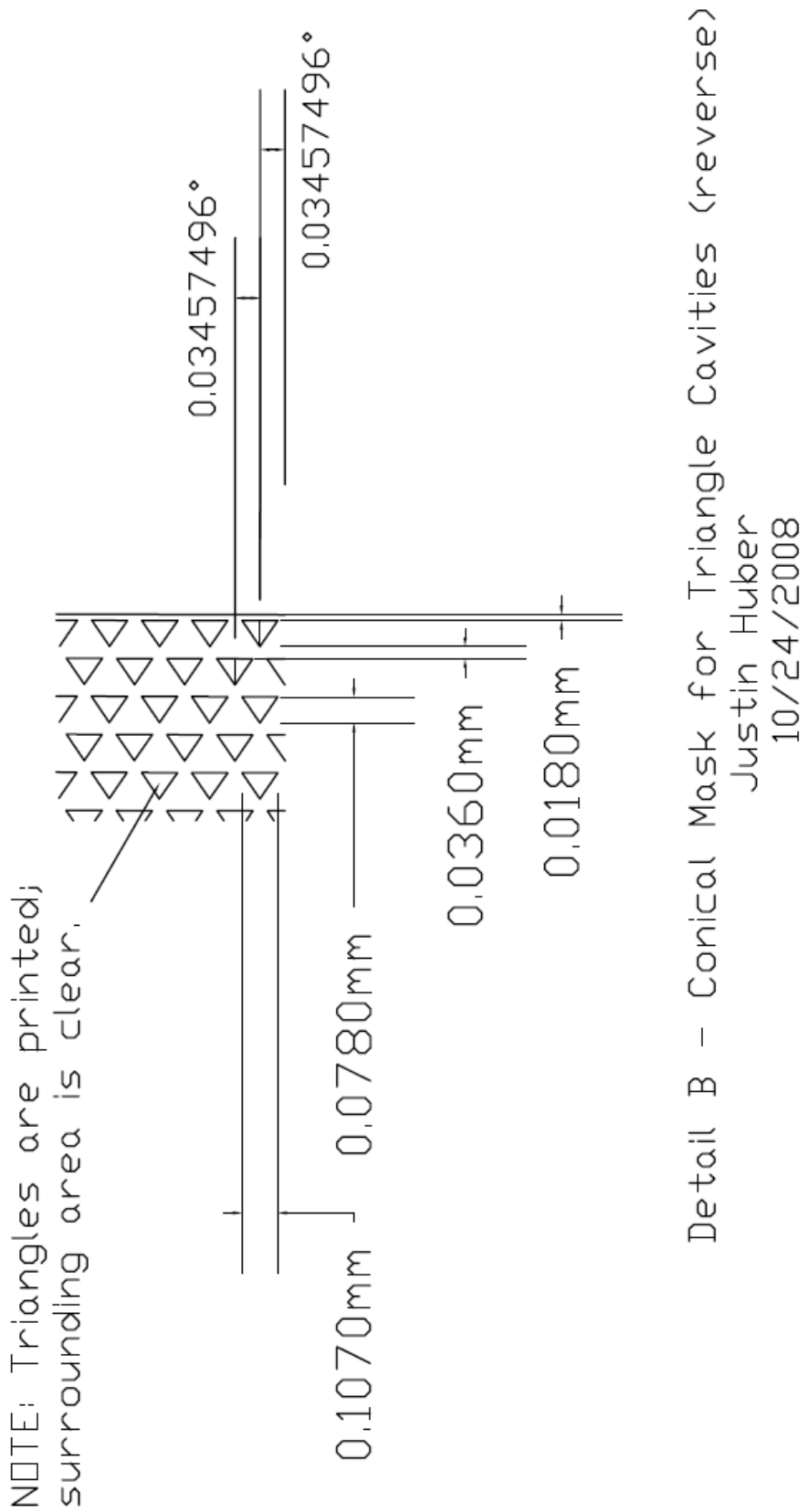

APPENDIX E – MACHINIST DRAWING FOR CLAMP PLATE

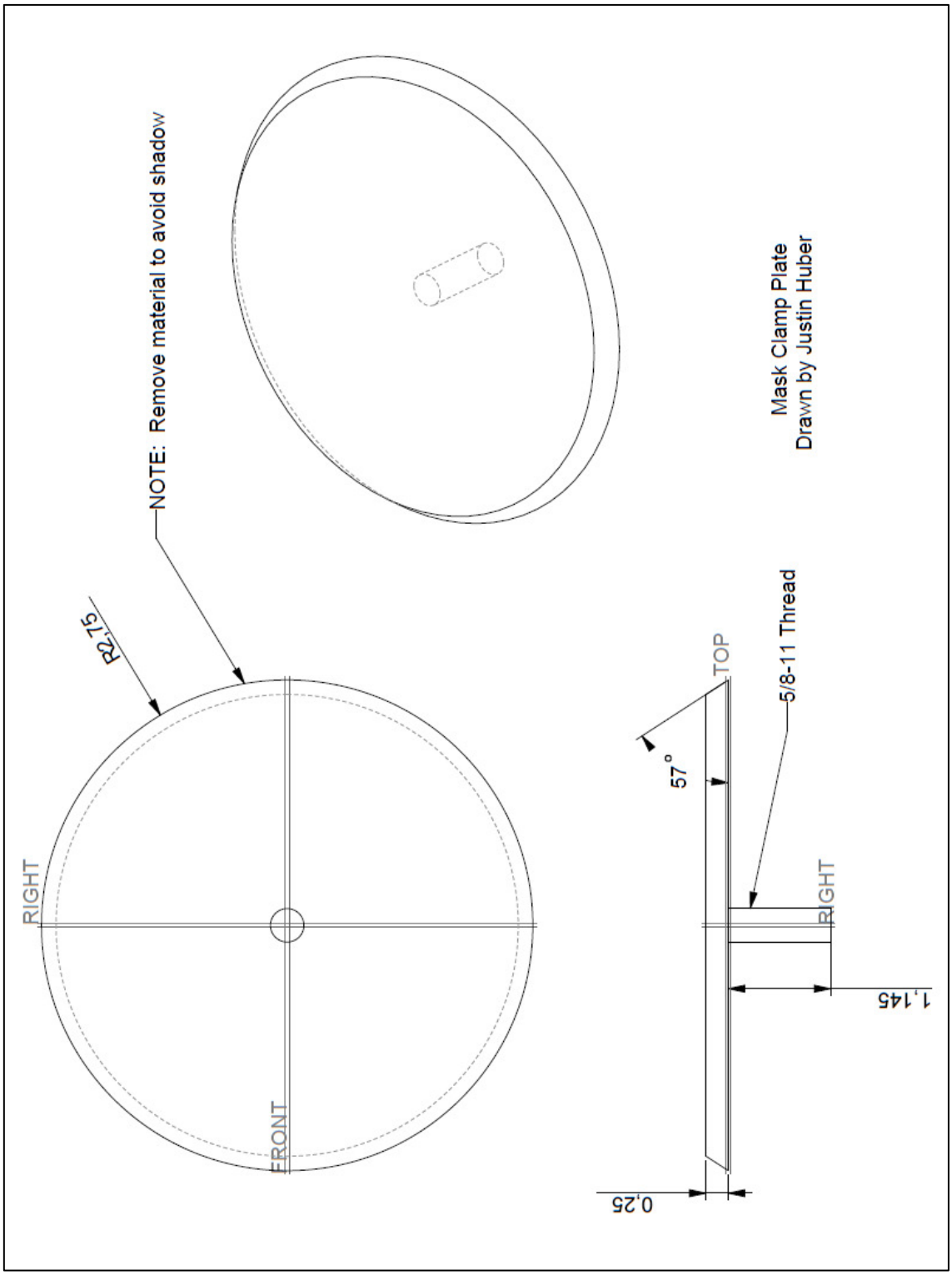

APPENDIX F – MATLAB® CODE TO FIND COVERAGE RATIO (CR)

```
%Coverage Ratio

%The following code computes values of coverage ratio (CR).
%In particular, 8 separate values of CR are determined for each of
%the 8 separate Zygo measurements acquired per mold insert.

%Written by Justin Huber

clear all;

%User is prompted to input information relevant to the code
directory=input('Please input the directory: ','s');
mold_number=input('Please input mold number: ','s');
run_number=input('Please input run number: ','s');
directory_save=input('Please input directory to save results: ','s');
coats=...
    input('Input the #coats of photoresist applied in this sample run:
');
if coats==2
else if coats==3
    else if coats==4
        else if coats==6
            else
                disp(sprintf('Input not recognized!!'));
                return
            end
        end
    end
end
base=input('Input "Ra" value of the unprocessed sample (microns): ');


area_ratio=zeros(1,8);  %Placeholders to save results of code
area_perc=zeros(1,8);
threshold=zeros(1,8);

removed=zeros(1,8);     %Counter for data points removed by filter
missing=zeros(1,8);     %Counter for data points containing "NaN"


for N=1:8
    filename=[directory,'\mold',num2str(mold_number),'_m',...
        num2str(N),'_xcylinder.xyz'];


    [X,Y,Z,x,y,z,resoln]=read_zygo_data(filename);
                %Function created by Chris Morgan to read
                %a Zygo "xyz" file.
```

```
%Histogram-based filtering method used to remove suspect data
%near the extremes of the distribution
edges=min(z):(max(z)-min(z))/1999:max(z);
M=histc(z,edges);
H=1;
while M(H)<15
    H=H+1;
end
lower=edges(H);     %Lower limit of accepted data points
H=2000;
while M(H)<15
    H=H-1;
end
upper=edges(H+1);   %Upper limit of accepted data points

for K=1:length(z);  %Limits applied to vector format of data
    if z(K)<lower
        z(K)=nan;       %Values below lower limit removed
        removed(N)=removed(N)+1;
    else if z(K)>upper
            z(K)=nan;   %Values above upper limit removed
            removed(N)=removed(N)+1;
        end
    end
end
for L=1:640         %Limits applied to mesh format of data
    for O=1:480
        if Z(L,O)<lower
            Z(L,O)=nan;
        else if Z(L,O)>upper
                Z(L,O)=nan;
            end
        end
    end
end


threshold(N)=min(z)+base+4.5301*(coats);
                %Threshold for covereage determination comprises
                %the sum of the min Z-height, Ra value, & coat
                %thickness

pixels=0;       %Pixels are data points at which z-height
                %exceeds threshold

for I=1:640
    for J=1:480                 %Inspect each point of the "xyz"
        if Z(I,J)>threshold(N)  %mesh and compare the z-heights
            pixels=pixels+1;    %to the threshold
        else if isnan(Z(I,J))
            missing(N)=missing(N)+1;
            end
        end
    end
end
```

```
    area=pixels*resoln*resoln;      %Conversion of pixel number to an
                                    %area value using the resolution
                                    %indicated in the "xyz" file.

    area_ratio(N)=area/((640*480)*resoln^2);
    area_perc(N)=100*area_ratio(N);
                %Approximate percent of area
                %covered by photoresist

    %Coverage ratio rounded to 4 decimal places
    CR=area_ratio(N);
    CR=CR*10000;
    CR=round(CR);
    CR=CR/10000;
    CR_disp=['CR=',num2str(CR)];

    %Plot created showing surface data, threshold, and calculated CR
    threshold_plane=threshold(N)*ones(640,480);
    figure(N),mesh(X,Y,Z),hold on,surf(X,Y,threshold_plane),hold off
    set(gcf,'Units','normalized','OuterPosition',[0 0.03 1 0.97]);
    set(gca,'fontsize',30)
    title('Surface Profile and Threshold Plane','fontsize',30,...
        'fontweight','bold')
    xlabel('x [\mum]','fontsize',30)
    ylabel('y [\mum]','fontsize',30)
    zlabel('z [\mum]','fontsize',30)
    zlimit=zlim;
    zpos=zlimit(1)-(0.4*((zlimit(2)-zlimit(1))));
    text(700,100,zpos,CR_disp,'fontsize',50,'color','r',...
        'fontweight','bold')

    %Plots saved to appropriate file directory
    save_name=[directory_save,'\mold',num2str(mold_number),'_m',...
        num2str(N),'_matlab_run',num2str(run_number)];
    saveas(N,save_name,'bmp');

end

area_perc
threshold           %Results from code
missing
removed

close all;
```

APPENDIX G – MATLAB® CODE TO FIND IDEAL COVERAGE RATIO

```
%Ideal Coverage Ratio

%Ideal coverage ratio determined by inspecting the printed
%conicalmasks.  That is, the desired value was acquired by
%distinguishing the inked areas from the non-inked areas.

%Written by Justin Huber

clear all;

%User prompted for information relevant to code
filename=input('Please input the appropriate directory: ','s');

[X,Y,Z,x,y,z,resoln]=read_zygo_data(filename);
            %Function created by Chris Morgan to read a
            %Zygo "xyz" file.

pixels=0;               %Pixels are data points with ink
missing=0;              %Counter for pixels containing "NaN"
for I=1:640
    for J=1:480                 %Each point of the "xyz" mesh inspected

        if Z(I,J)>0             %Positive values of "z" are defined as
            pixels=pixels+1;    %data points with ink
        else if isnan(Z(I,J))
            missing=missing+1;
            else
                Z(I,J)=0;       %Negative values assigned "0" to
            end                 %to clarify the visual plot
        end

    end
end

area=pixels*resoln*resoln;      %conversion of pixel number to an area
                                %using the resolution indicated in the
                                %"xyz" file.

inked_area_ratio=area/(((640*480)-missing)*resoln^2);
ideal_CR=(1-inked_area_ratio)
display=['Ideal CR = ',num2str(ideal_CR)];
                                %Since the non-inked areas would be
                                %equivalent to the areas covered by
                                %photoresist, then the percentage of
                                %the mask area that is non-inked is
                                %the value of interest.
missing
```

```
%Data is plotted in an isometric view
surf(X,Y,Z)
set(gcf,'Units','normalized','OuterPosition',[0 0.03 1 0.97]);
shading interp
view(320,80)
set(gca,'fontsize',20);
title('Ideal Coverage Ratio','fontsize',35,'fontweight','bold');
xlabel('x [\mum]','fontsize',35);
ylabel('y [\mum]','fontsize',35);
zlabel('z [\mum]','fontsize',35);
zlimit=zlim;
zpos=zlimit(1)-(1.25*((zlimit(2)-zlimit(1))));
text(400,0,zpos,display,'fontsize',40,'color','r','fontweight','bold')
```

APPENDIX H – 1st DOE RESULTS FOR COVERAGE RATIO

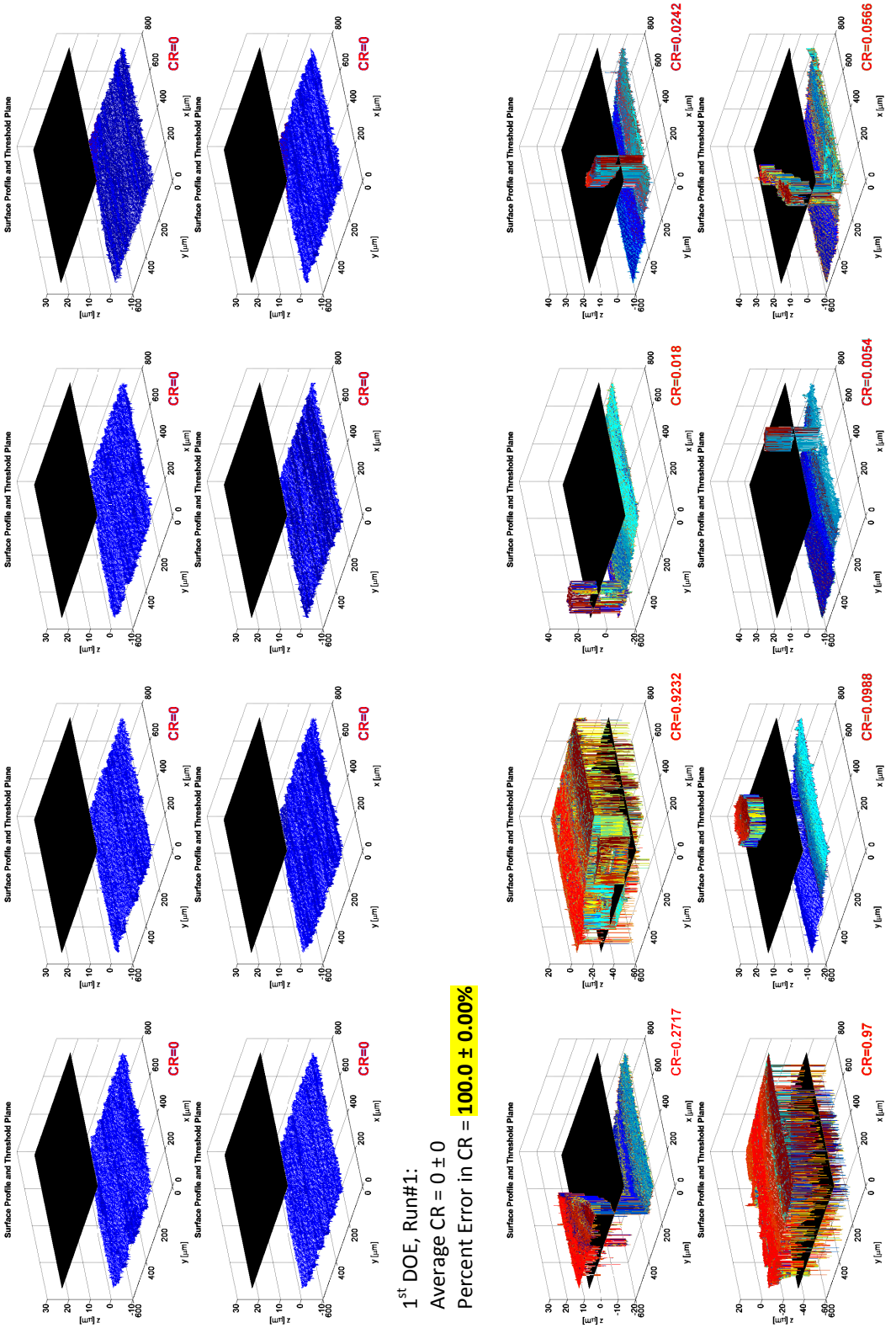

1st DOE, Run#1:
Average CR = 0 ± 0
Percent Error in CR = **100.0 ± 0.00%**

1st DOE, Run#2
Average CR = 0.3623 ± 0.437
Percent Error in CR = **73.04 ± 32.82%**

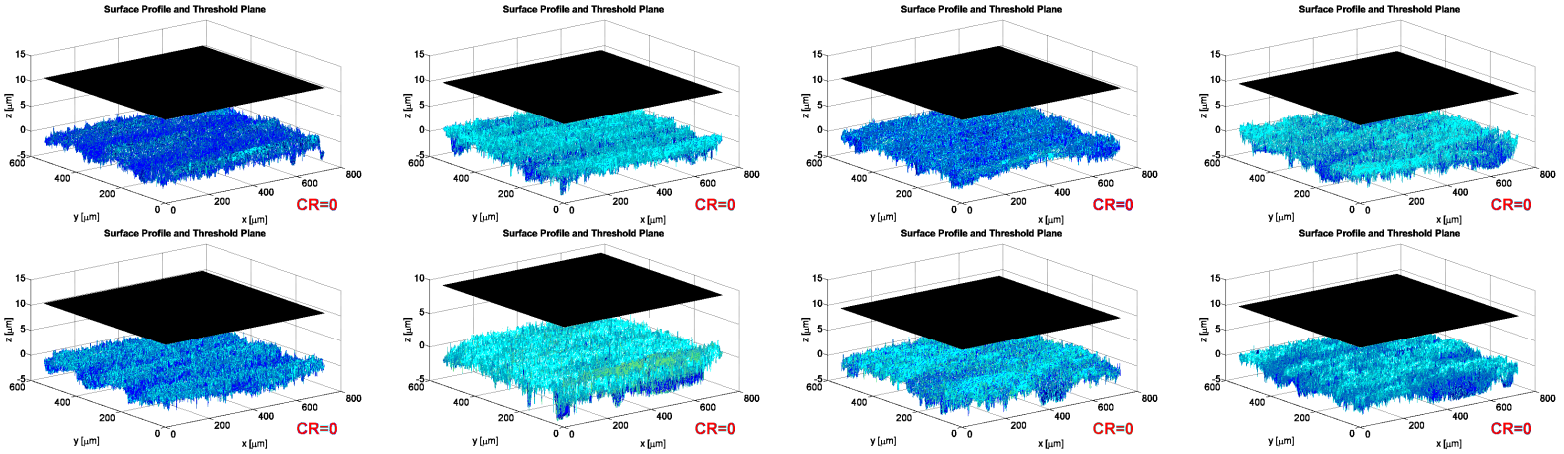

1st DOE, Run#3:
Average CR = 0 ± 0
Percent Error in CR = **100.0 ± 0.00%**

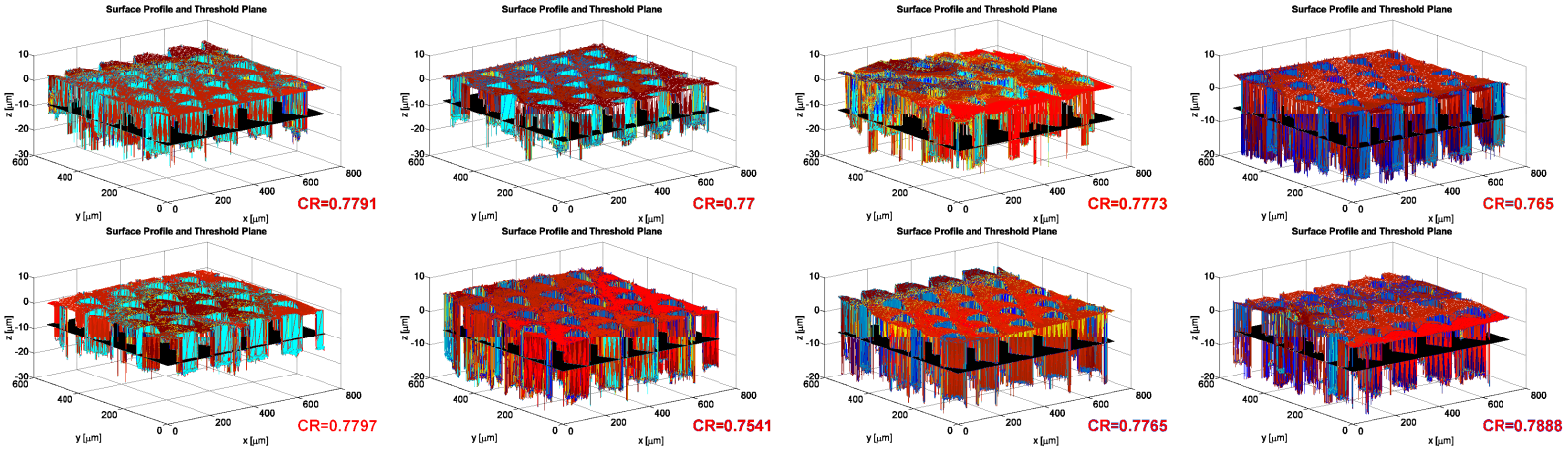

1st DOE, Run#4:
Average CR = 0.7738 ± 0.011
Percent Error in CR = **1.21 ± 0.77%**

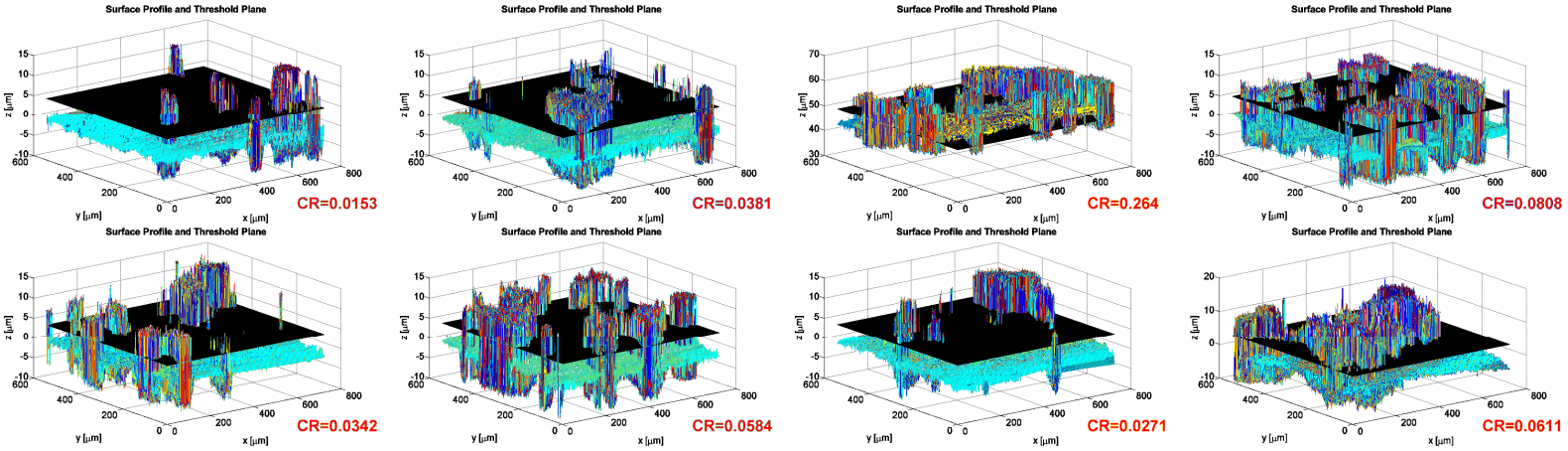

1st DOE, Run#5:
Average CR = 0.0724 ± 0.080
Percent Error in CR = **90.6 ± 10.43%**

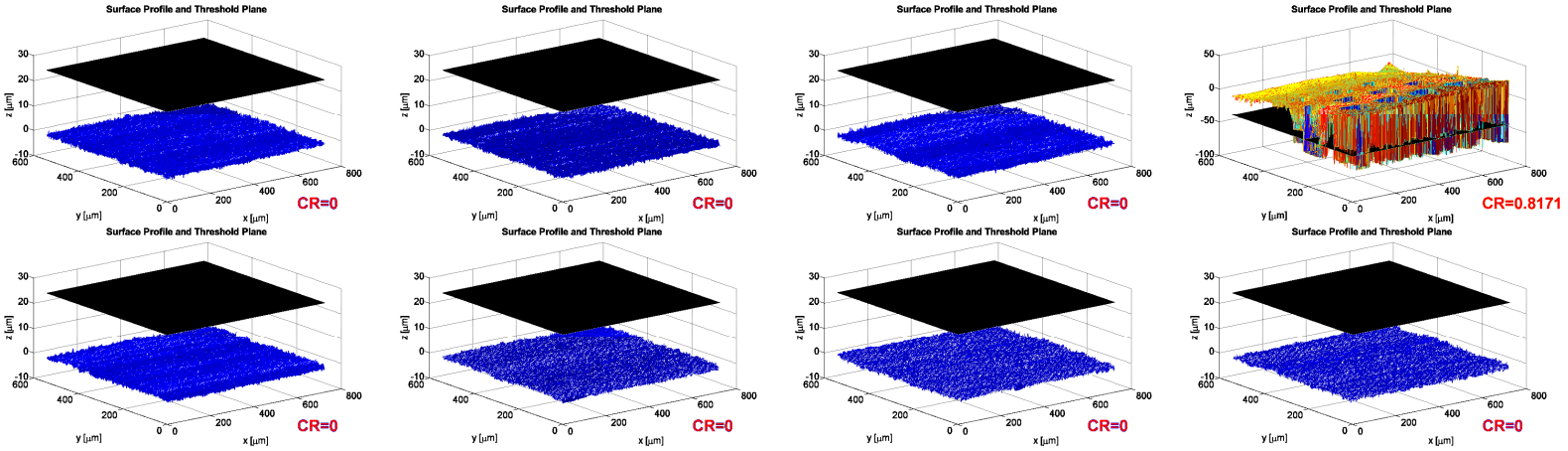

1st DOE, Run#6:
Average CR = 0.1021 ± 0.289
Percent Error in CR = **88.27 ± 33.16%**

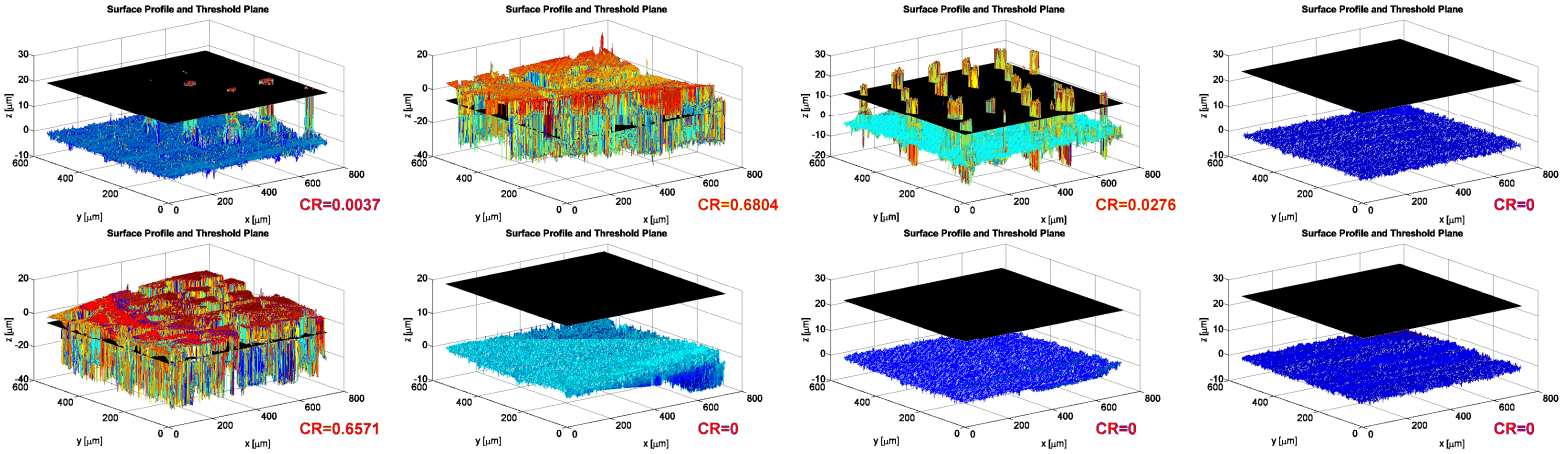

1st DOE, Run#7:

Average CR = 0.1711 ± 0.307

Percent Error in CR = **77.76 ± 39.95%**

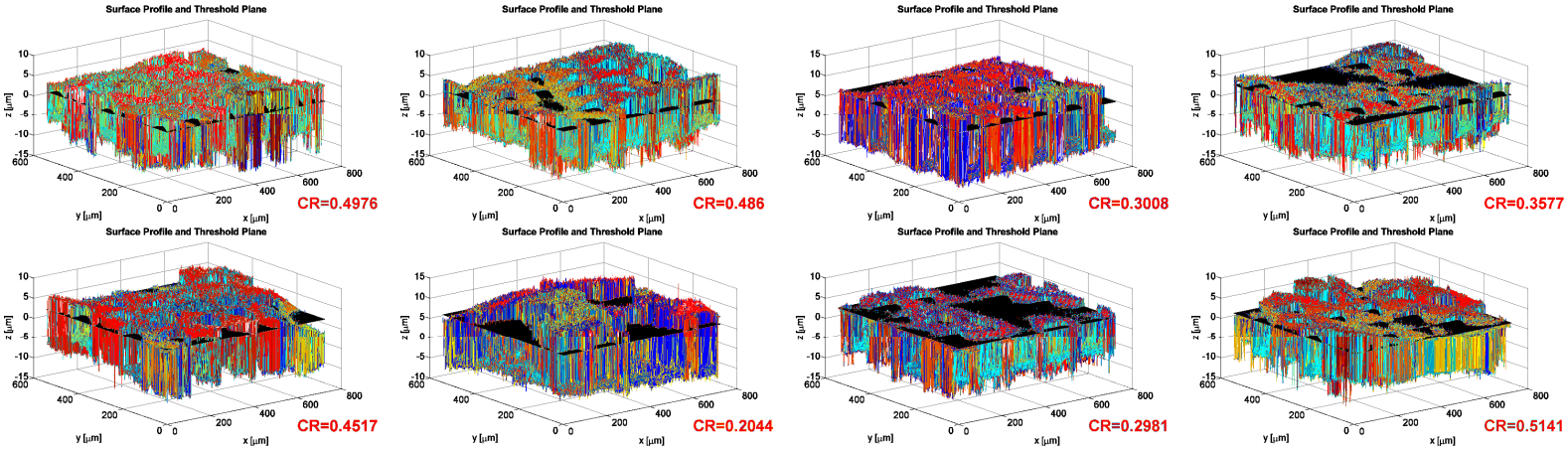

1st DOE, Run#8:

Average CR = 0.3888 ± 0.115

Percent Error in CR = **49.47 ± 14.89%**

APPENDIX I – 1st DOE RESULTS OF ANOVA

Treatment	Run	(A) Layers of Photoresist		(B) Exposure Dosage		(C) Pre-Bake Times		(D) Mask Cutting		AB	AC	AD	Measurement - Percent Error in Coverage Ratio							
		(-) 3 Coats	(+) 6 Coats	(-) 1x Recommended (400mJ/cm²)	(+) 2x Recommended (800mJ/cm²)	(-) None	(+) As Is	(-) By Hand	(+) Die-Cut				y1	y2	y3	y4	y5	y6	y7	y8	y_bar
4	1	+		+		-		-		+	-	-	100.00	100.00	100.00	100.00	100.00	100.00	100.00	100.00	100.00
6	2	+		-		+		-		-	+	-	64.69	19.98	97.66	96.86	26.08	87.16	99.30	92.64	73.05
1	3	-		-		-		-		+	+	+	100.00	100.00	100.00	100.00	100.00	100.00	100.00	100.00	100.00
7	4	-		+		+		-		-	-	+	1.26	0.08	1.02	0.57	1.34	1.99	0.92	2.52	1.21
5	5	-		-		+		+		+	-	-	98.01	95.05	65.69	89.49	95.55	92.42	96.48	92.06	90.59
8	6	+		+		+		+		+	+	+	100.00	100.00	100.00	6.20	100.00	100.00	100.00	100.00	88.28
2	7	+		-		-		+		-	-	+	99.52	11.57	96.41	100.00	14.60	100.00	100.00	100.00	77.76
3	8	-		+		-		+		-	+	-	35.32	36.83	60.91	53.51	41.29	73.43	61.26	33.18	49.47
	∑+		339.0843		238.9538		253.1280		306.0975	378.8688	310.7880	267.2500									
	∑-		241.2725		341.4030		327.2288		274.2593	201.4880	269.5688	313.1068									
	∑+/n+		84.7711		59.7384		63.2820		76.5244	94.7172	77.6970	66.8125									
	∑-/n-		60.3181		85.3508		81.8072		68.5648	50.3720	67.3922	78.2767									
	Effect		24.4529		-25.6123		-18.5252		7.9596	44.3452	10.3048	-11.4642									

Source of Variation	SS	df	MS	F	F'	%
A (Layers of Photoresist)	9567.1409	1	9567.141	18.65244	2.8	10.56%
B (Exposure Dosage)	10495.851	1	10495.85	20.46309	2.8	11.59%
C (Pre-Bake Times)	5490.9193	1	5490.919	10.70529	2.8	6.06%
D (Mask Cutting)	1013.6734	1	1013.673	1.976294	2.8	1.12%
AB	31463.926	1	31463.93	61.34319	2.8	34.75%
AC	1699.0276	1	1699.028	3.312485	2.8	1.88%
AD	2102.8427	1	2102.843	4.099777	2.8	2.32%
Error	28723.316	56	512.9164			31.72%
Total	90556.697	63				

NOTE: $F_{critical}$ obtained from Table A.2 of Appendix of "Practical Guide to Experimental Design" by Frigon & Mathews; Value corresponds to α=0.10.

APPENDIX J – 2nd DOE RESULTS FOR COVERAGE RATIO

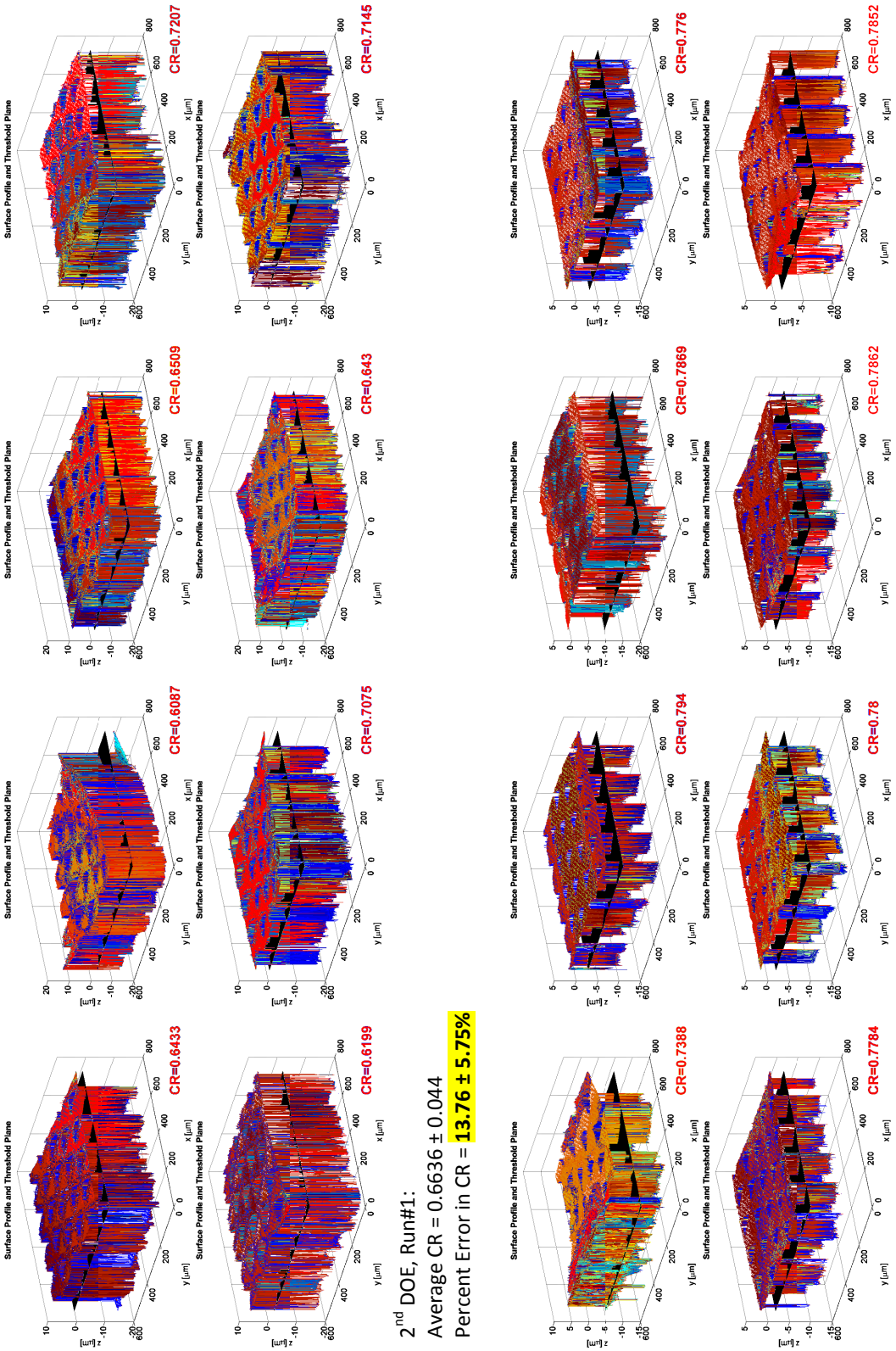

2nd DOE, Run#1:
Average CR = 0.6636 ± 0.044
Percent Error in CR = **13.76 ± 5.75%**

2nd DOE, Run#2:
Average CR = 0.782 ± 0.017
Percent Error in CR = **2.13 ± 1.05%**

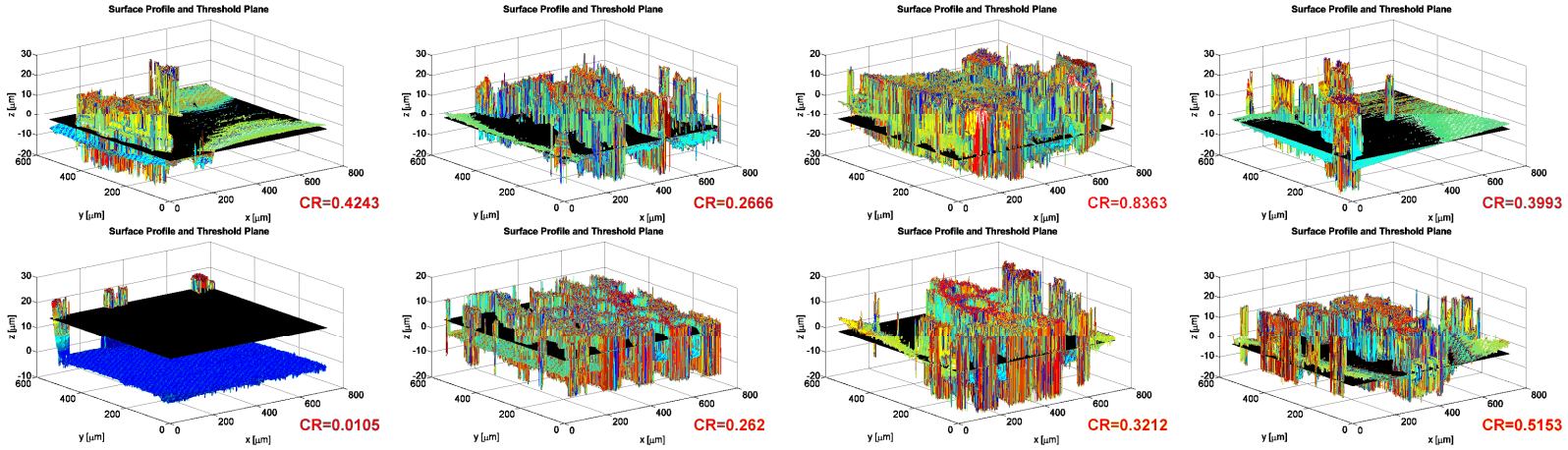

2nd DOE, Run#3:

Average CR = 0.3794 ± 0.238

Percent Error in CR = **52.86 ± 26.41%**

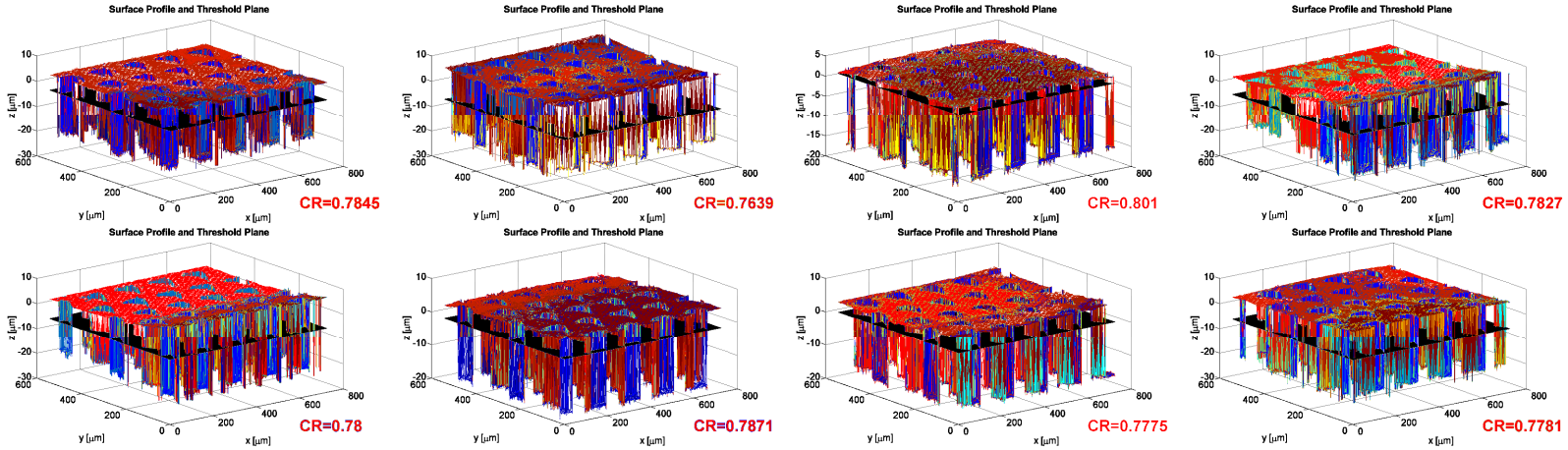

2nd DOE, Run#4:

Average CR = 0.7819 ± 0.01

Percent Error in CR = **1.79 ± 1.07%**

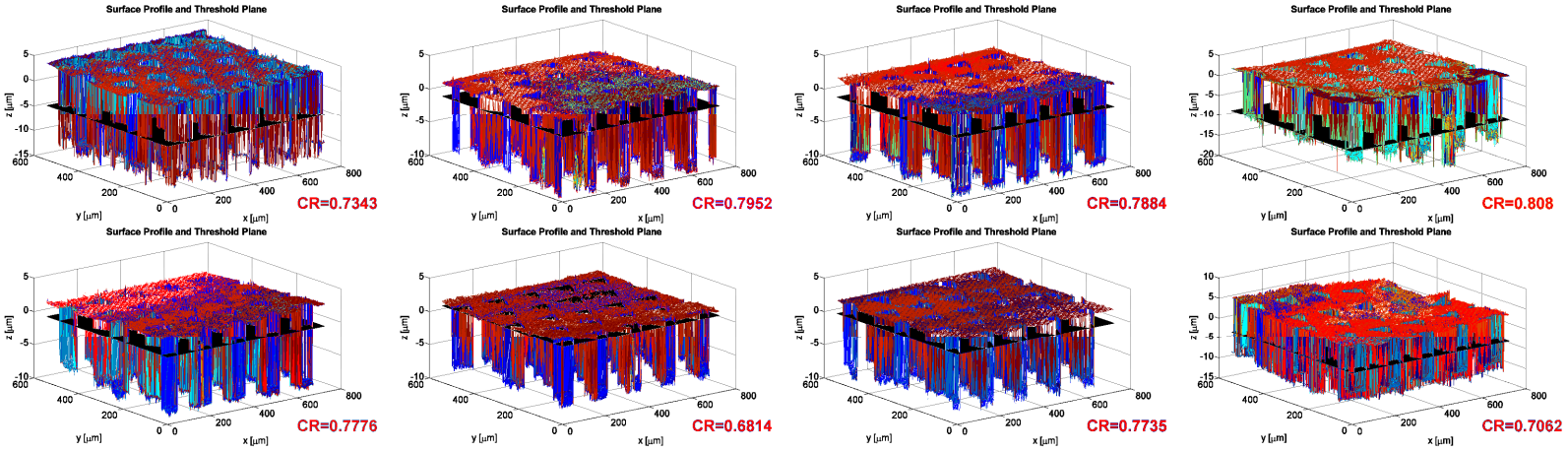

2nd DOE, Run#5:

Average CR = 0.7581 ± 0.046

Percent Error in CR = **4.58 ± 3.69%**

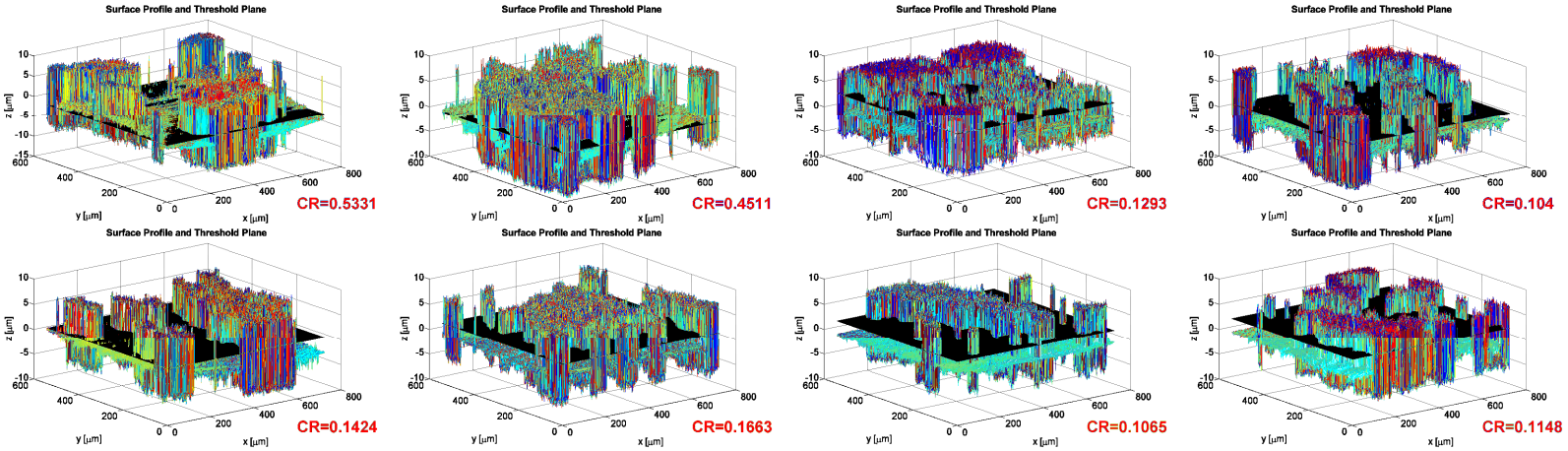

2nd DOE, Run#6:

Average CR = 0.2184 ± 0.172

Percent Error in CR = **71.61 ± 22.29%**

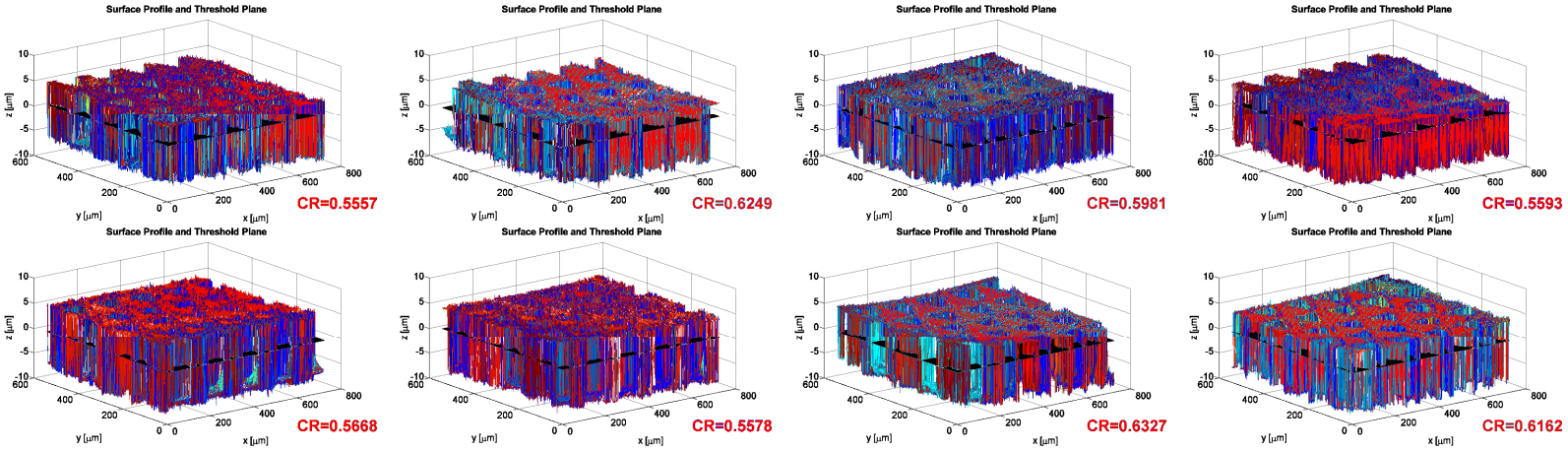

2nd DOE, Run#7:

Average CR = 0.5889 ± 0.033

Percent Error in CR = **23.46 ± 4.25%**

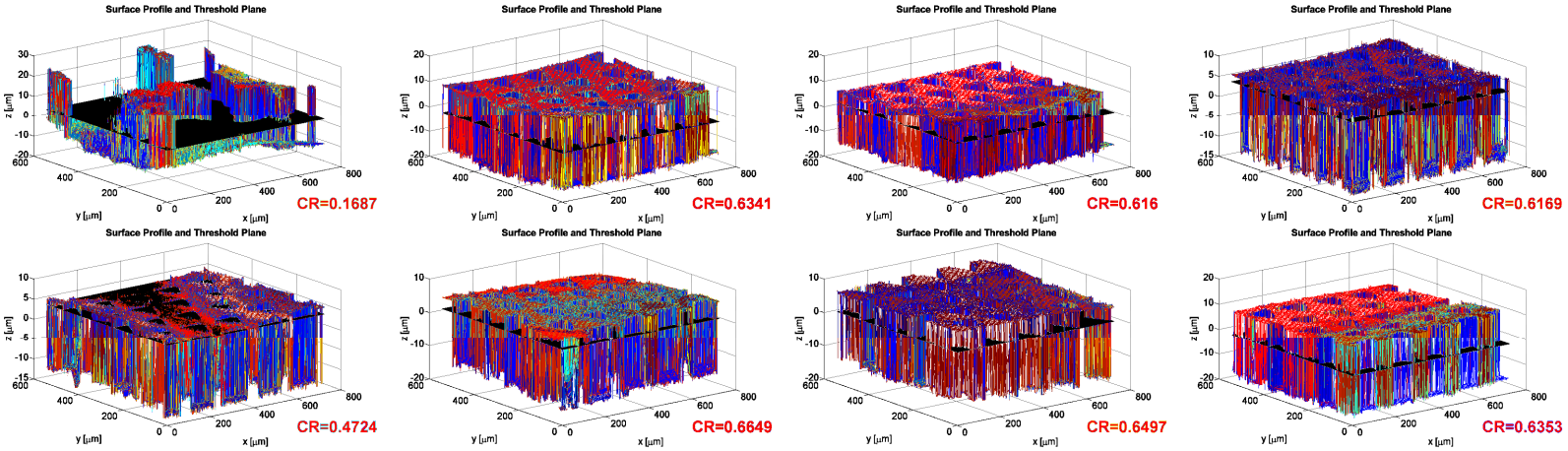

2nd DOE, Run#8:

Average CR = 0.5572 ± 0.168

Percent Error in CR = **27.58 ± 21.82%**

APPENDIX K – 2nd DOE RESULTS OF ANOVA

Treatment	Run	(A) Layers of Photoresist: 2	(A) Layers of Photoresist: 4	(B) Exposure Dosage (mJ/cm²): 300	(B) Exposure Dosage (mJ/cm²): 600	(B) Exposure Dosage (mJ/cm²): 900	(B) Exposure Dosage (mJ/cm²): 1200	Measurement - Percent Error in Coverage Ratio: y1	y2	y3	y4	y5	y6	y7	y8	y_bar
1	6	✓		✓				16.39	20.88	15.40	6.34	19.44	8.05	16.43	7.13	13.76
2	3		✓	✓				3.98	3.19	2.27	0.85	1.17	1.38	2.18	2.05	2.13
3	7	✓			✓			44.86	65.35	8.69	48.11	98.63	65.94	58.25	33.03	52.86
4	8		✓		✓			1.96	0.71	4.11	1.73	1.38	2.31	1.05	1.13	1.80
5	5	✓				✓		4.56	3.36	2.47	5.01	1.07	11.45	0.53	8.22	4.58
6	1		✓			✓		30.71	41.37	83.20	86.48	81.49	78.39	86.16	85.08	71.61
7	2	✓					✓	27.77	18.78	22.27	27.30	26.33	27.51	17.77	19.91	23.46
8	4		✓				✓	78.07	17.59	19.93	19.82	38.61	13.59	15.56	17.42	27.57

Source of Variation	SS	df	MS	F	F'	% Contribution
A (Layers of Photoresist)	71.592752	1	71.59275	0.329631	2.8	0.15%
B (Exposure Dosage)	7484.0084	3	2494.669	11.48608	2.14	15.38%
AB	28935.277	3	9645.092	44.4084	2.14	59.47%
Error	12162.679	56	217.1907			25.00%
Total	48653.558	63				

NOTE: $F_{critical}$ obtained from Table A.2 of Appendix of "Practical Guide to Experimental Design" by Frigon & Mathews; Value corresponds to α=0.10.

APPENDIX L – 3rd DOE RESULTS FOR COVERAGE RATIO

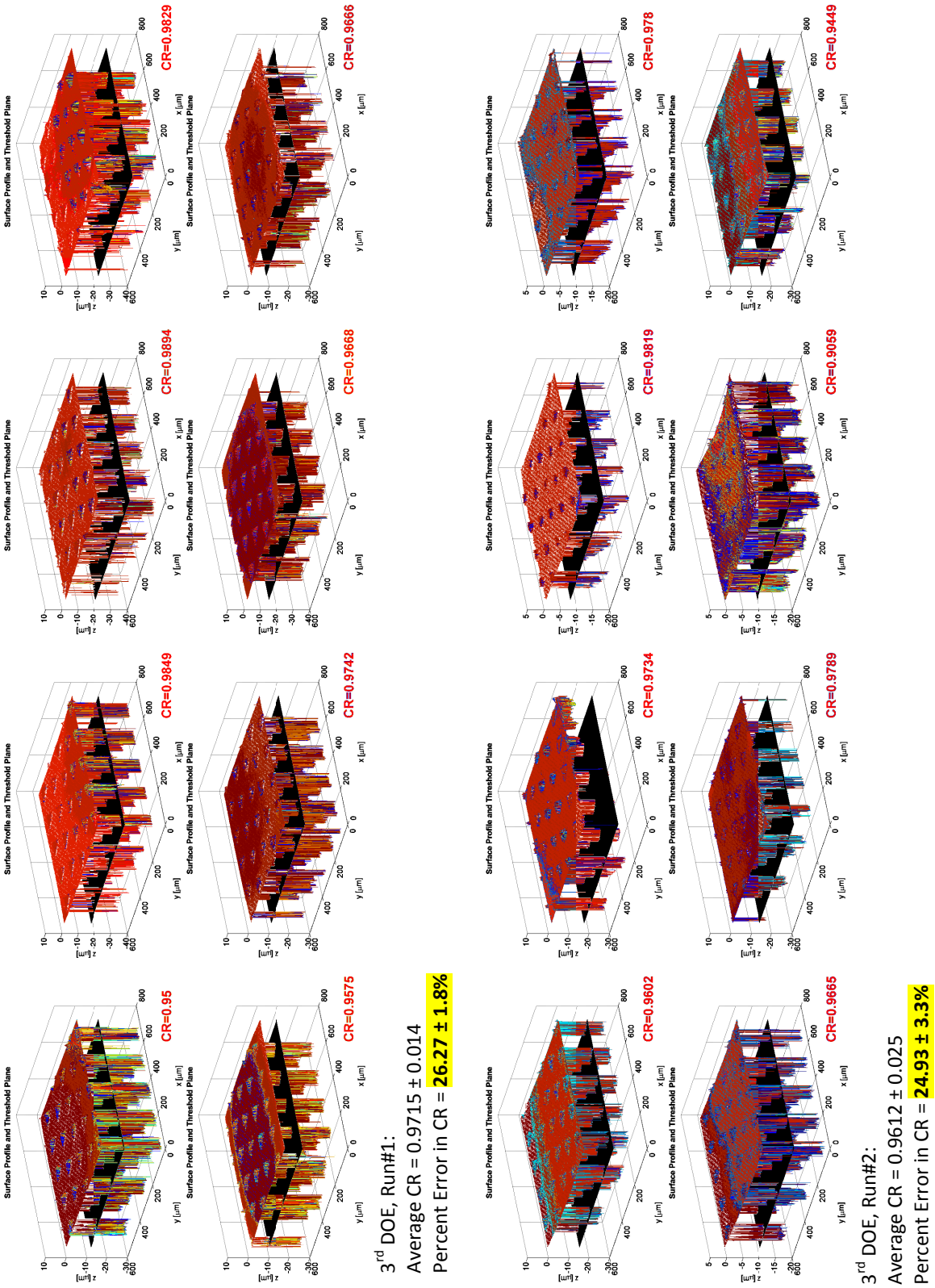

3rd DOE, Run#1:
Average CR = 0.9715 ± 0.014
Percent Error in CR = **26.27 ± 1.8%**

3rd DOE, Run#2:
Average CR = 0.9612 ± 0.025
Percent Error in CR = **24.93 ± 3.3%**

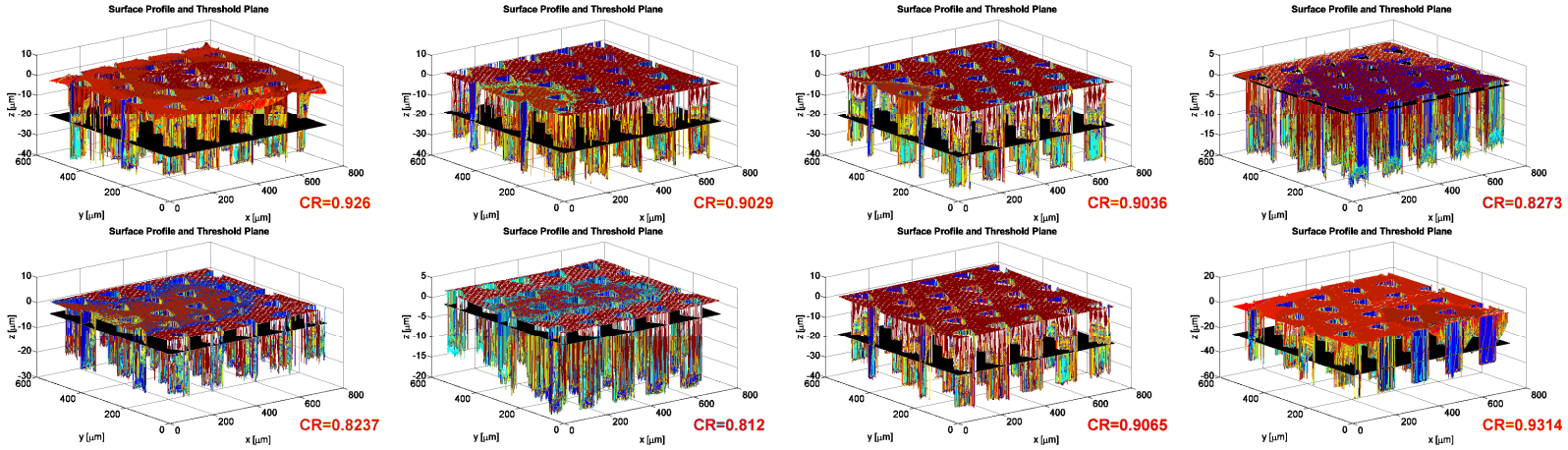

3rd DOE, Run#3:

Average CR = 0.8792 ± 0.049

Percent Error in CR = **14.27 ± 6.42%**

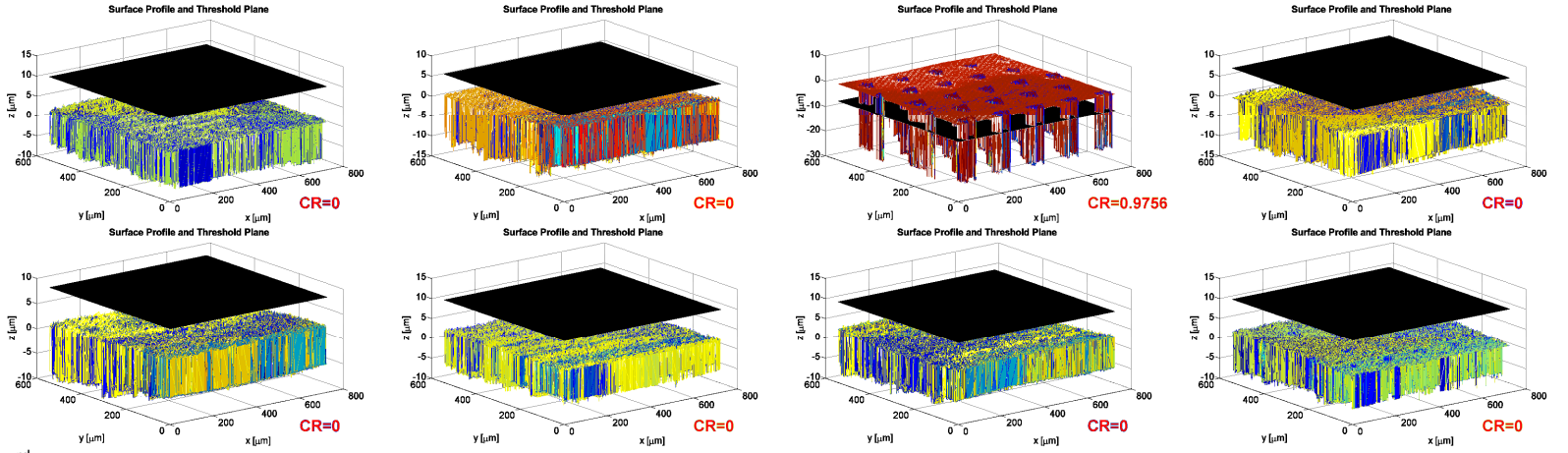

3rd DOE, Run#4:

Average CR = 0.1219 ± 0.345

Percent Error in CR = **90.85 ± 25.88%**

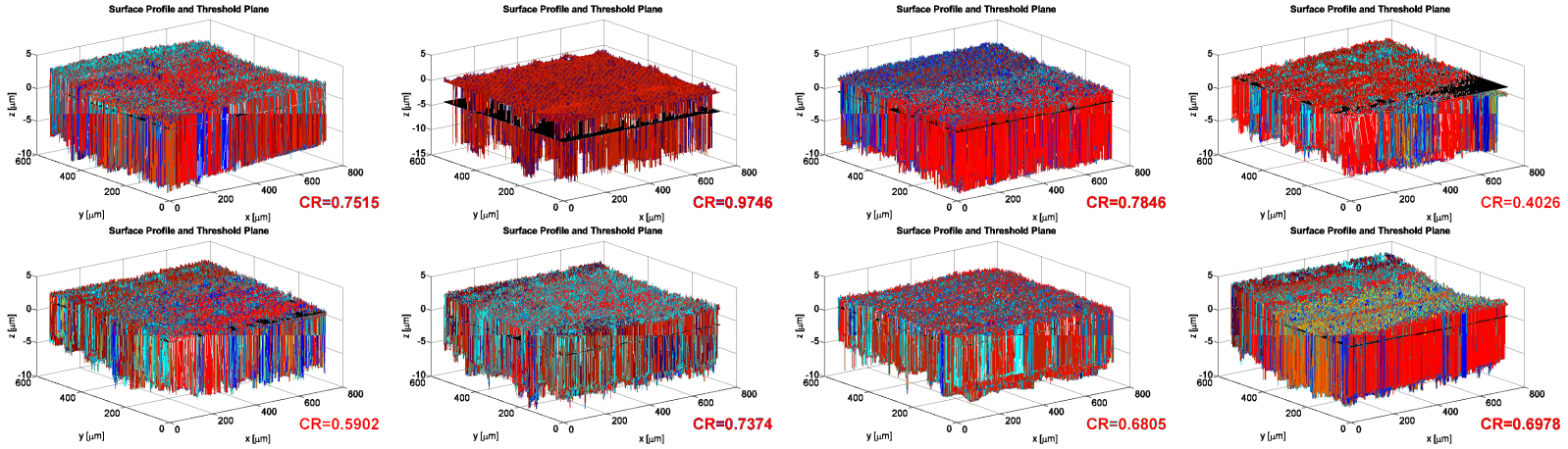

3rd DOE, Run#5:

Average CR = 0.7024 ± 0.164

Percent Error in CR = **15.87 ± 15.85%**

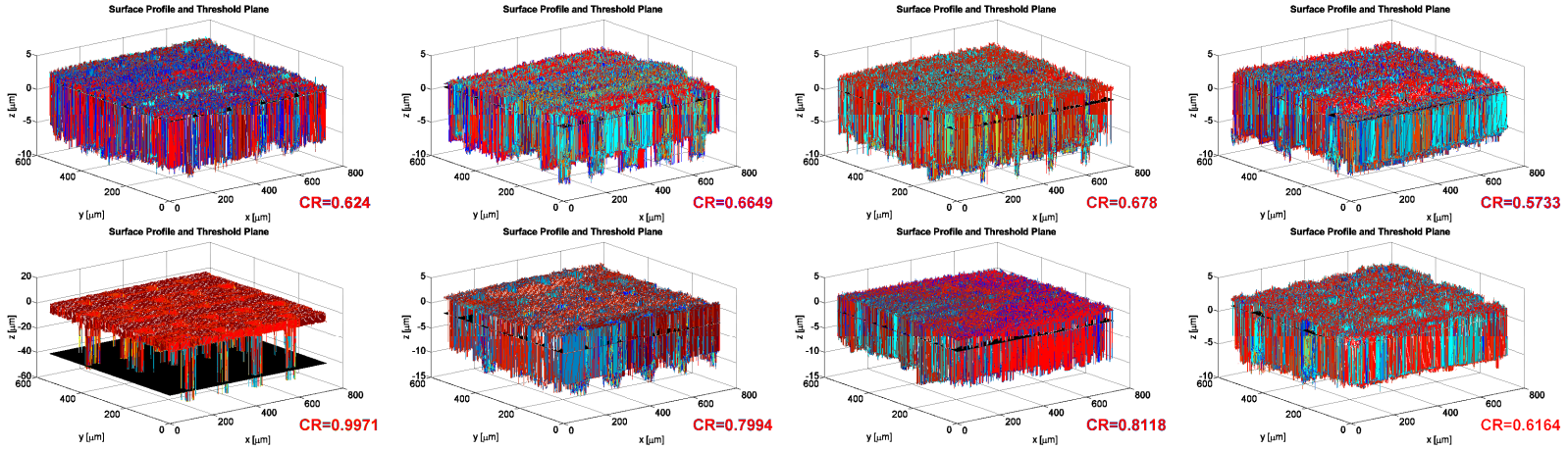

3rd DOE, Run#6:

Average CR = 0.7206 ± 0.14

Percent Error in CR = **16.09 ± 9.08%**

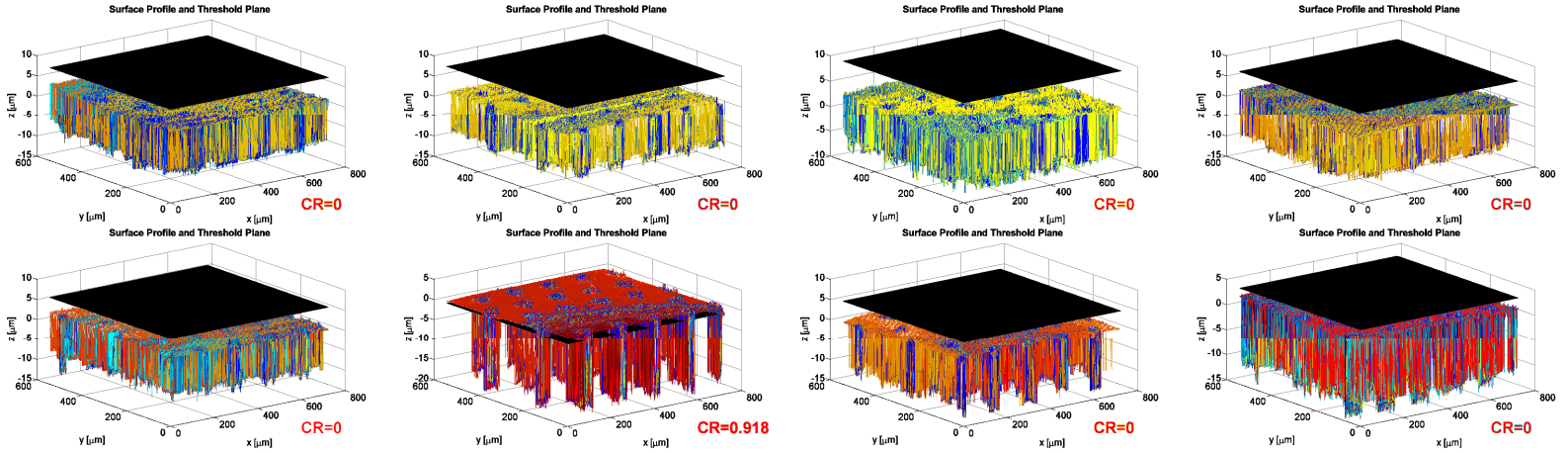

3rd DOE, Run#7:

Average CR = 0.1147 ± 0.325

Percent Error in CR = **89.91 ± 28.53%**

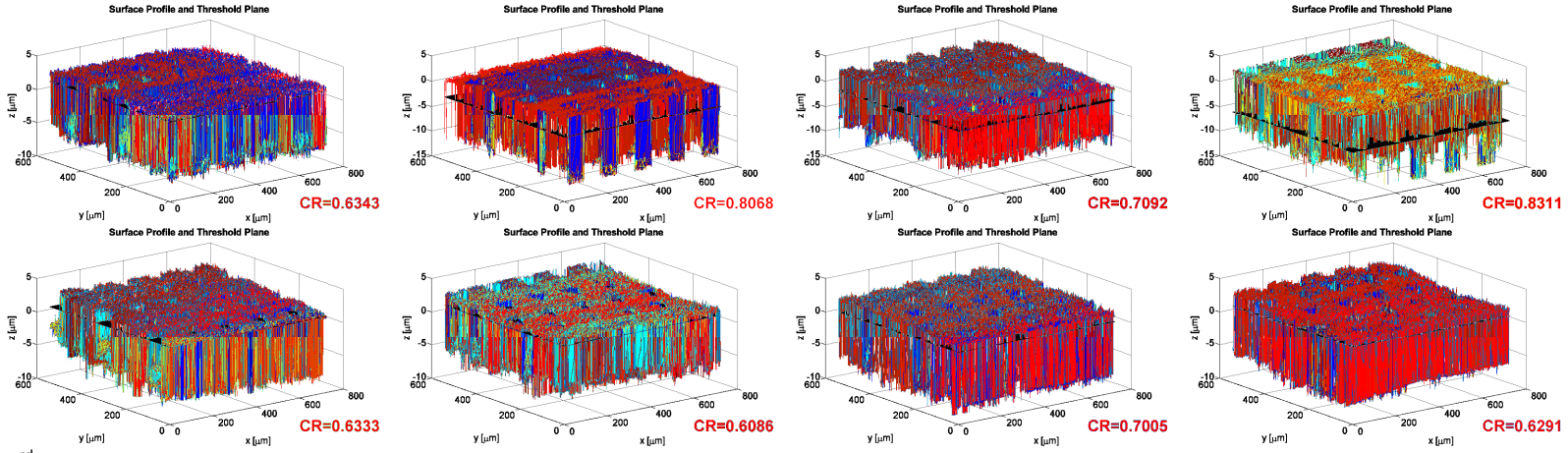

3rd DOE, Run#8:

Average CR = 0.6941 ± 0.085

Percent Error in CR = **13.01 ± 6.17%**

APPENDIX M – 3rd DOE RESULTS OF ANOVA

Treatment	Run	(A) Layers of Photoresist		(B) Exposure Dosage (mJ/cm^2)				Measurement - Percent Error in Coverage Ratio								
		2	4	300	600	900	1200	y1	y2	y3	y4	y5	y6	y7	y8	y_bar
1	8	✓		✓				24.52	29.10	29.69	28.84	25.50	27.70	26.73	26.70	27.35
2	3		✓	✓				25.86	27.59	28.71	28.2	26.69	28.32	18.75	23.86	90.04
3	6	✓			✓			21.37	18.36	18.44	8.45	7.97	6.44	18.82	22.09	15.24
4	7		✓		✓			100.00	100.00	27.88	100.00	100.00	100.00	100.00	100.00	90.99
5	5	✓				✓		1.49	27.75	2.85	47.23	22.63	3.34	10.79	8.53	15.58
6	1		✓			✓		18.20	12.85	11.13	24.85	30.70	4.78	6.41	19.21	16.02
7	2	✓					✓	100.00	100.00	100.00	100.00	100.00	20.33	100.00	100.00	90.04
8	4		✓				✓	16.85	5.75	7.04	8.94	16.99	20.23	8.19	17.54	12.69

Source of Variation	SS	df	MS	F	F'	% Contribution
A (Layers of Photoresist)	6.3378063	1	6.337806	0.00455	2.8	0.00%
B (Exposure Dosage)	16352.353	3	5450.784	3.913264	2.14	11.58%
AB	46881.522	3	15627.17	11.21917	2.14	33.19%
Error	78002.381	56	1392.9			55.23%
Total	141242.59	63				

REFERENCES

1. Christophe Marques, Yohannes Desta, James Rogers, Michael Murphy, and Kevin Kelly. "Fabrication of High-Aspect-Ratio Microstructures on Planar and Nonplanar Surface Using a Modified LIGA Process." *Journal of Microelectromechanical Systems* (1997); 6(4):329-336.

2. K. Kim, S. Park, J.-B. Lee, H. Manohara, Y. Desta, M. Murphy, and C.H. Ahn. "Rapid Replication of Polymeric and Metallic High Aspect Ratio Microstructures using PDMS and LIGA Technology." *Microsystem Technologies* (2002); 9(1-2):5-10.

3. Manhee Lee, Woonseob Lee, Sung-Keun Lee, and Seung S. Lee. "3D Microfabrication with Inclined/Rotated UV Lithography". *Sensors and Actuators A: Physical* (2004); 111(1):14-20.

4. L. Frasson, T. Parittotokkaporn, A. Schneider, B.L. Davies, J.F.V. Vincent, S.E. Huq, P. Degenaar, and F.M. Rodriguez Baena. "Biologically Inspired Microtexturing: Investigation into the Surface Topography of Next-Generation Neurosurgical Probes." *Engineering in Medicine and Biology Society, Vancouver, BC* (2008); 5611-5614.

5. Christophe Marques. "Manufacture of LIGA Heat Exchanger on Tube." PhD Dissertation, Louisiana State University (May 2003).

6. Hiroshi Miyajima and Mehran Mehregany. "High-Aspect-Ratio Photolithography for MEMS Applications." *Journal of Microelectromechanical Systems* (1995); 4(4):220-229.

7. Ren Yang, Jing Jiang, Wanjun Wang, and W.J. Meng. "UV-LIGA Fabrication of Microscale Two-Level Mold Inserts for MEMS Applications." *Proceedings of SPIE* (2005); 5717:175-184.

8. Zhong-geng Ling, Kun Lian, and Linke Jian. "Improved Patterning Quality of SU-8 Microstructures by Optimizing the Exposure Parameters." *Proceedings of SPIE* (2000); 3999:2000.

9. M. Rahman, A.B.M.A. Ased, T. Masaki, T. Saleh, Y.S. Wong, and A. Senthil Kumar. "A Multiprocess Machine Tool for Compound Micromachining." *International Journal of Machine Tools and Manufacture* (2010); 50(4):344-356.

10. Sarang Narayan Kortikar. "Fabrication and Characterization of Deterministic Micro-Asperities on Thrust Surfaces." MS Thesis, University of Kentucky (November 2004).

11. G. Dumitru, V. Romano, H.P. Weber, H. Haefke, Y. Gerbig, and E. Pflüger. "Laser Microstructuring of Steel Surfaces for Tribological Applications." *Applied Physics A: Materials Science and Processing* (2000); 70(4):485-487.

12. Jenny Paige. "Paige ARO December 2003C." Powerpoint, Bearing and Seals Laboratory, University of Kentucky (2003).

13. Katherine H. Warren and Lyndon Scott Stephens. "Effect of Shaft Microcavity Patterns for Flow and Friction Control on Radial Lip Seal Performance—A Feasibility Study." *Tribology Transactions* (2009); 52:731-743.

14. Wen Dai, Kun Lian, and Wanjun Wang. "A Quantitative Study on the Adhesion Property of Cured SU-8 on Various Metallic Surfaces." *Microsystem Technologies* (2005); 11:526-534.

15. Michael Parodi, Tom Batchelder, Peter Haaland, and Jim McKibben. "Spin Coating and Alternative Techniques for Flat Panel Displays." *Semiconductor International* (January 1996); 101-105.

16. Datasheet, Microchem® XP Negative Microspray™ (discontinued).

17. E.W. Becker, W. Ehrfeld, P. Hagmann, A. Maner, and D. Münchmeyer. "Fabrication of Micro Structures with High Aspect Ratio and Great Structural Heights by Synchotron Radiation, Lithography, Galvanoforming, and Plastic Molding." *Microelectronic Engineering* (1986); 4:35-56.

18. Vikas Galhotra, Venkat Sangishetty, En Ma, and Kevin Kelly. "Electroplated Nickel Mold Insert for LIGA." *Proceedings of SPIE* (1995); 2639:158-163.

19. Vikas Galhotra, Christophe Marques, Yohannes Desta, Kevin Kelly, Mircea Despa, Ajit Pendse, and John Collier. "Fabrication of LIGA Mold Inserts using Modified Procedure." *Proceedings of SPIE* (1996); 2879:168-173.

20. Jian Zhang. "LIGA Mold Insert Fabrication Using SU-8 Photoresist." MS Thesis, Louisiana State University (December 2002).

21. National Synchotron Light Source, http://www.nsls.bnl.gov

22. Sriram Venkatesan. "Surface Textures for Enhanced Lubrication: Fabrication and Characterization Techniques." MS Thesis, University of Kentucky (June 2005).

23. Rodrigo Lima de Miranda, Christiane Zamponi, and Eckhard Quandt. "Rotational UV Lithography Device for Cylindrical Substrate." *Review of Scientific Instruments* (2009); 80(1):015103(1)-015103(5).

24. P.-F. Chauvy, P. Hoffmann, and D. Landalt. "Applications of Laser Lithography on Oxide Film to Titanium Micromachining." *Applied Surface Science* (2003); 208-209:165-170.

25. Vetrivel Kanakasabai. "Detailed Surface Analysis of Lip Seal Elastomers Ran Against Shafts Manufactured with Triangular Cavities." MS Thesis, University of Kentucky (August 2009).

26. M. Geiger, S. Roth, and W. Becker. "Influence of Laser Produced Microstructures on the Tribological Behaviour of Ceramics." *Surface and Coatings Technology* (1998); 100-101:17-22.

27. I. Etsion and E. Sher. "Improving Fuel Efficiency with Laser Surface Textured Piston Rings." *Tribology International* (2009); 42(4):542-547.

28. U. Pettersson and S. Jacobson. "Tribological Texturing of Steel Surfaces with a Novel Diamond Embossing Tool Technique." *Tribology International* (2006); 39:695-700.

29. W. Yu, S. Cargill, M. Leonard, and M.P.Y. Desmulliez. "Micro-fabrication on 3-D Surface by Electrostatic Induced Lithography." *Electronics System-Integration Technology Conference, Greenwich, UK* (2008); 111-116.

30. Wen Dai and Wanjun Wang. "Fabrication of Comb-Drive Micro-Actuators Based on UV Lithography and Electroless Plating Technique." *Microsystem Technologies* (2008); 14:1745-1750.

31. Ren Yang, Seok J. Jeong, and Wanjun Wang. "UV-LIGA Microfabricated of a Power Relay Based on Electrostatic Actuation." *Proceedings of SPIE* (2003); 4981:122-130.

32. Chris J. Morgan, R. Ryan Vallence, and Eric R. Marsh. "Micro Machining Glass with Polycrystalline Diamond Tools Shaped by Micro Electro Discharge Machining." *Journal of Micromechanics and Microengineering* (2004); 14:1687-1692.

33. Ryan Anthony Turner. "Tapered LIGA Mold Insert." MS Thesis, Louisiana State University (December 2002).

34. L.S. Stephens, R. Siripuram, M. Hayden, and B. McCartt. "Deterministic Micro Asperities on Bearings and Seals Using a Modified LIGA Process." *Journal of Engineering for Gas Turbines and Power* (2004); 126:147-154.

35. A. Blatter, M. Maillat, S.M. Pimenov, G.A. Shafeev, A.V. Simaken, and E.N. Loubnin. "Lubricated Sliding Performance of Laser-Patterned Sapphire." *Wear* (1999); 232(2):226-230.

36. D. Allegretti, G. Daurelio, and F. Guerrini. "Laser Surface Micro-Texturing on the Mechanical Seals Rings Enhancing the Tribological Properties." *Proceedings of SPIE* (2001); 4184:512-518.

37. Izhak Etsion. "Improving Tribological Performance of Mechanical Components by Laser Surface Texturing." *Tribology Letters* (2004); 17(4):733-737.

38. Aviram Ronen, Izhak Etsion, and Yuri Kligerman. "Friction-Reducing Surface-Texturing on Reciprocating Automotive Components." *Tribology Transactions* (2001); 44(3):359-366.

39. Philip C. Hadinata and Lyndon Scott Stephens. "Soft Elastohydrodynamic Analysis of Radial Lip Seals with Deterministic Microasperities on the Shaft." *Journal of Tribology* (2007); 129:851-859.

40. A. Shinkarenko, Y. Kligerman, and I. Etsion. "The Effect of Elastomer Surface Texturing in Soft Elasto-Hydrodynamic Lubrication." *Tribology Letters* (2009); 36(2):95-103.

41. Manabu Wakuda, Yukihiko Yamauchi, Shuzo Kanzaki, and Yoshiteru Yasuda. "Effect of Surface Texturing on Friction Reduction Between Ceramic and Steel Materials under Lubricated Sliding." *Wear* (2003); 254:356-363.

42. Ulrika Petterson and Staffan Jacobson. "Textured Surfaces for Improved Lubrication at High Pressures and Low Sliding Speeds of Roller/Piston in Hydraulic Motors." *Tribology International* (2007); 40:355-359.

43. I. Etsion and G. Halperin. "A Laser Surface Textured Hydrostatic Mechanical Seal." *Tribology Transactions* (2002); 45(3):430-434.

44. D.S.-W. Park, M.L. Hupert, M.A. Witek, B.H. You, P. Datta, J. Guy, J.B. Lee, S.A. Soper, D.E. Nikitapoulos, and M.C. Murphy. "A Titer Plate-Based Polymer Microfluidic Platform for High Throughput Nucleic Acid Purification." *Biomedical Microdevices* (2008); 10:21-33.

45. Christophe Marques. "Heat Transfer of a Microstructure-covered Cylinder in Crossflow." MS Thesis, Louisiana State University (August 1997).

46. Kevin Kelly, Chistophe Marques, James Rogers, Mircea Despa, and John Collier. "High-Aspect-Ratio Microstructure-covered Sheets: Fabrication and Function." *Proceedings of SPIE* (1998); 3328:403-408.

47. Christophe Marques and Kevin Kelly. "Fabrication and Performance of a Pin Fin Micro Heat Exchanger." *Journal of Heat Transfer* (2004); 126(3):434-444.

48. John A. Rogers, Rebecca J. Jackman, and George M. Whitesides. "Micro-contact Printing and Electroplating on Curved Substrates: Production of Free-Standing Three-Dimensional Metallic Microstructures." *Advanced Materials* (1997); 9(6):475-477.

49. John A. Rogers. "Techniques and Applications for Non-Planar Lithography." *Materials Research Society Symposium—Proceedings* (2002); 739:31-38.

50. Jenny Marie Paige. "Experimental and Theoretical Comparison of Radial Lip Seal Operation." MS Thesis, University of Kentucky (April 2005).

51. J.M. Amiss, Franklin D. Jones, Henry H. Ryffel. *Machinery's Handbook, 22nd Edition*. Industrial Press Inc., United States (1984); 22nd Edition:2104.

52. Zygo® NewView 5000 System Manual OMP-0471.

53. B. Smith, D.M. Brewis, G.W. Critchlow, and R.H. Dahm. "Cleaning Stainless Steel Surfaces to Improve the Adhesion of Photoresist Coatings." *Transactions of the Institute of Metal Finishing* (2000); 78:56-60.

54. D.M Brewis. "Adhesion to Polymers: How Important are Weak Boundary Layers?" *International Journal of Adhesion and Adhesives* (1993); 13(4):251-256.

55. Nga P. Pham, Joachim N. Burtghartz, and Pasqualina M. Sarro. "Spray Coating of Photoresist for Pattern Transfer on High Topography Surfaces." *Journal of Micromechanics and Microengineering* (2005); 15:691-697.

56. Datasheet, Microchem® XP SU-8 Microspray™.

57. Vijay K. Singh, Minoru Sasaki, Kazuhiro Haven, and Masayoshi Esashi. "Flow Condition in Resist Spray Coating and Patterning Performance for Three-Dimensional Photolithography over Deep Structures." *Japanese Journal of Applied Physics* (2004); 43(4B):2387-2391.

58. Y.-J. Chuang, F.-G. Tseng, and W.-K. Lin. "Reduction of Diffraction Effect of UV Exposure on SU-8 Negative Thick Photoresist by Air Gap Elimination." *Microsystem Technologies* (2002); 8:308-313.

59. Bo Li, Miao Liu, and Quanfang Chen. "Low-stress Ultra-thick SU-8 UV Photolithography Process for MEMS." *Journal of Microlithography, Microfabrication, and Microsystems* (2005); 4(4):043008(1)-043008(6).

60. Paul I. Hagouel, Ioannis Karafyllidis, and Andrew R. Neureuther. "Dependence of Developed Negative Resist Profiles on Exposure Energy Dose: Experiment, Modeling, and Simulation." *Microelectronic Engineering* (1998); 41-42:351-354.

61. GwangBeom Kim, Changdae Park, Dong Sun Seo, Sang Jeen Hong. "Delamination Analysis of Low-Temperature Processed SU-8 Photoresist for MEMS Device Fabrication." *Key Engineering Materials* (2007); 345-346:1397-1400.

62. John D. Williams and Wanjun Wang. "Study on the Post-Baking Process and the Effects on UV-Lithography of High Aspect Ratio SU-8 Micro-structures." *Journal of Microlithography, Microfabrication, and Microsystems* (2004); 3(4):563-568.

63. Paul I. Hagouel, Ioannis Karafyllidis, and Andrew Neureuther. "Developer Temperature Effect on Negative Deep Ultraviolet Resists: Characterization, Modeling, and Simulation." *Journal of Vacuum Science and Technology B* (1997); 15(6):2616-2620.

64. Pinner, Soderberg, and Baker. "Nickel Plating." *Modern Electroplating*. The Electrochemical Society, New York (1942).

65. Bianca McCartt. "Nickel Electroplating Procedure." Bearings and Seals Laboratory, University of Kentucky (2003).

66. Electroplating notes. Bearings and Seals Laboratory, University of Kentucky.

67. Norman Frigon and David Mathews. *Practical Guide to Experimental Design*. John Wiley & Sons Inc., New York (1997).

68. Email correspondence, Scott Lattime, The Timken® Company.

69. Victoria J. Hodge and Jim Austin. "A Survey of Outlier Detection Methodologies." *Artificial Intelligence Review* (2004); 22:85-126.

70. E. Ong, R.M. Baker, and L.P. Hale. "A Two-Layer Photoresist Process for patterning High-Reflectivity Substrates." *Journal of Vacuum Science and Technology B* (1983); 1(4):1247-1250.

71. Wu-Sheng Shih, Charles J. Neef, and Mark G. Daffron. "A Planarization Process for Multi-Layer Lithography Applications." *Proceedings of SPIE* (2004); 5376:664-672.

VITA

Justin P. Huber was born December 20, 1983 in Lexington, Kentucky. He earned a Bachelor in Science degree in Mechanical Engineering in 2006 from the University of Kentucky. As an undergraduate, Justin received the Presidential Scholarship, and participated in the Pi Tau Sigma Engineering Honor Fraternity. As a graduate, he received the Graduate School Academic Fellowship. His interests are focused toward engineering applications in the medical field.